Evapotranspiration Tagging for the Poyang Lake Region, Southeast China

Dissertation zur Erlangung des Doktorgrades an der
Fakultät für Angewandte Informatik der
Universität Augsburg

vorgelegt von

Jianhui Wei

2015

Erstes Gutachten:	Prof. Dr.	Harald Kunstmann
Zweites Gutachten:	PD. Dr.	Andreas Philipp

Tag der mündlichen Prüfung: 28.04.2016

Acknowledgements

Completion of this work was with the support of various people.

First of all, I would like to express my sincere gratitude to my supervisor, Prof. Harald Kunstmann, for accepting me as his PhD student, for offering me the opportunity to work on the ET-Tagging topic, and for his excellent supervision and constant support.

My sincere gratitude goes to PD Dr. Andreas Philipp (University of Augsburg) for his kind agreement to act as secondary referee.

My gratefulness goes to Dr. Hans Richard Knoche, who has been always available for discussions in the regional climate modeling field and in the complexities of the atmospheric branch of the hydrological cycle, and for answering questions.

My special thanks go to Dr. Benjamin Fersch and Dr. Sven Wagner for their helpful technological supports and valuable scientific discussions.

The atmosphere at the Institute of Meteorology and Climate Research (KIT/IMK-IFU), in the Regional Climate and Hydrology group, and in our offices has always been very positive and friendly: many thanks to all my colleges and friends in Garmisch-Partenkirchen.

This work is funded by China Scholarship Council (CSC) and by Karlsruhe Institute of Technology (KIT).

Furthermore, I would like to thank European Centre for Medium-Range Weather Forecasts for access to the ERA-Interim reanalysis data, APHRODITE's Water Resources for APHRODITE, Max Plank Institute for Biogeochemistry for FLUXNET MTE, Climatic Research Unit for CRUT, and NOAA/National Centers for Environmental Information for IGRA.

The help of Dr. Joël Arnault, Dr. Benjamin Fersch, Dr. Dominikus Heinzeller, Dr. Patrick Laux, Dipl.-Ing. Christof Lorenz, and Dr. Sven Wagner from KIT/IMK-IFU for proofreading the manuscript is gratefully acknowledged.

Last but not least, I thank my wife, Qi Song, for all her patience, understanding, and motivation and also our parents for their support.

Content

List of Figures

List of Tables

List of Abbreviations

AGCM	Atmospheric General Circulation Model
APHRODITE	Asian Precipitation–Highly-Resolved Observational Data Integration Towards Evaluation of the Water Resources
CCSR/NIES	Centre for Climate System Research/National Institude for Environmental Studies
CHRM	Climate High-Resolution Model
COSMO	Consortium for Small-scale Modeling
CRUT	CRUTEM3
CST	Chinese Standard Time
DTR	Diurnal Temperature Range
ECMWF	European Centre for Medium-Range Weather Forecasts, Reading, UK
ERA	ECMWF Reanalysis
FAO	Food and Agriculture Organization
FLEXPART	Flexible Particle Dispersion Model
FLUXNET-MTE	Global Network of Eddy Covariance Towers–Model Tree Ensemble
FVGCM	Finite Volume General Circulation Model
GCM	General Circulation Model
GEOS-3	Geodetic and Earth Orbiting Satellite 3
HYSPIT	Hybrid Single Particle Lagrangian Integrated Trajectory Model
IGRA	Integrated Global Radiosonde Archive

LSM	Land Surface Model
MERRA	Modern-ERA Retrospective Analysis for Research and Applications
MM5	The Fifth-Generation Pennsylvania State University/NCAR Mesoscale Model
MPI	Message Passing Interface
MRF	Revised Medium-Range Forecast Model
NASA/GISS	National Aeronautics and Space Administration/Goddard Institute for Space Studies, USA
NOAA	National Oceanic and Atmospheric Administration
Noah-MP	The Community Noah Land Surface Model With Multi-Parametrization Options
OpenMP	Open Multi-Processing
OSU	Oregon State University
PBL	Planetary Boundary Layer
PSU	Pennsylvania State University
QIBT	Quasi-Isentropic Backward Trajectories
RCM	Regional Climate Model
RMSE	Root Mean Square Error
RRTM	Rapid Radiative Transfer Model
SST	Sea Surface Temperature
USGS	United States Geological Survey
UTC	Universal Time Coordinated
WAM	Water Accounting Model

Abstract

Land-atmosphere interaction analysis still lacks adequate methods for explicitly answering one of the center hydrological question of "what is the fate of evapotranspired water", and likewise, "where, when, and to what extent evapotranspiring water of one region returns as precipitation in the same or another region", and "what are water residence times across the atmosphere".

In this thesis, a regional climate model (RCM) based evapotranspiration tagging (ET-Tagging) algorithm has been applied for the first time to the subtropical monsoon and mountainous region of Southeast China. 15 month simulations (October 2004 to December 2005) were performed to investigate where and to which extent the tagged evapotranspired water from a predefined source region around the Poyang Lake (the largest freshwater lake in China) returning to the land surface as precipitation. To assess the relative importance of the individual evapotranspiration components for the ET-driven precipitation, the model has been extended to partition the total evapotranspiration into direct evaporation (consisting of evaporation from inland water bodies, evaporation from the top soil layer, and evaporation of precipitation intercepted by the canopy) and transpiration and to track the two partitions separately. Using this extended ET-Tagging partitioning algorithm, the contributions of direct evaporation and transpiration to precipitation were estimated separately.

Since, the atmospheric water residence time is a fundamental descriptor that provides information on the timescales of evapotranspiration (direct evaporation and transpiration) and precipitation, the algorithm has been further extended with an age tracer approach. This newly developed age-weighted ET-Tagging partitioning algorithm allows to calculate the atmospheric residence times of evapotranspired water (of direct evaporated water and of transpired water, separately), and to assess the celerity of the atmospheric branch of the hydrological cycle.

The most important results are: In 2005 the contribution of moisture originating from the Poyang Lake region to the annual precipitation in Southeast China reaches a value of up to 1.2 %, with a maximum of 6 % near the Poyang Lake region in August. A budget analysis indicates that in 2005 the tagged precipitation falling in the source area,

in the Poyang Lake basin, and in Southeast China equate to 0.8 %, 2.7 %, and 10.7 % of the evapotranspired water in the Poyang Lake region, respectively. Regarding the ET-Tagging partitioning, in 2005 direct evaporated water accounts for 64 % and transpired water for 36 % of the total tagged moisture with a mean age of around 36 hours for both. The condensed tagged moisture consists of a large proportion (69.2 %) of the young (7 hours) direct evaporated water and of a small amount of the older (11 hours) transpired water. Similarly, 69 % of total tagged precipitation originates from direct evaporation of water with a mean atmospheric residence time of 6.6 hours, whereas 31 % comes from vegetation transpiration with a longer residence time of 10.7 hours.

To explore the source-target relations under consideration of the respective precipitation regime (wet or dry weather conditions), source-specific precipitation efficiencies are introduced. For the period under investigation, the source-specific precipitation efficiency for direct evaporation generally dominates. Only during the comparatively dry August (with short residence times) and in the winter months (with small absolute transpiration values), the source-specific precipitation efficiency for transpiration is larger.

This thesis shows large spatial and temporal variations of the magnitude of tagged precipitation. There is a pronounced difference where and how long direct evaporation and transpiration are able to contribute to precipitation. Impacted by the East Asian monsoon, the patterns of the atmospheric water residence times change over the months. The results depict the the seasonal variations of the prevailing meteorological conditions and the varying interactions between land surface and atmosphere. The interactions control the annual cycle of the individual contributions to precipitation and the corresponding atmospheric water residence times, emphasizing the important impacts of vegetation cover and land use on the regional hydrological cycle.

In conclusion, with the age-weighted ET-Tagging partitioning algorithm developed in this work, the different fate of transpired and direct evaporated water in the atmospheric branch of the hydrological cycle is depicted. This algorithm has the potential to be used for addressing how the hydrological cycle changes and potentially accelerates with climate change.

Zusammenfassung

Für die Analyse von Land-Atmosphäre-Wechselwirkungen werden immer noch adäquate Methoden zur Beantwortung von zentralen hydrologischen Fragen gesucht, wie z. B. zu dem Fragen „Was wird aus dem in einer Region evapotranspiriertem Wasser?“ oder „Wo, wann und in welchem Umfang kehrt in einer bestimmten Region evapotranspiriertes Wasser wieder als Niederschlag in derselben oder in einer anderen Region zurück?“ und „Wie groß sind die Aufenthaltszeiten in der Atmosphäre?“

In dieser Arbeit wird zum ersten Mal ein auf einem regionalen Klimamodell (RCM) basierender Tagging-Mechanismus zur Evapotranspiration (*ET-Tagging*) auf eine monsunal beeinflusste subtropische Gebirgsregion in Südostchina angewendet. Simulationen über 15 Monate (Oktober 2004 bis Dezember 2005) wurden durchgeführt, um zu untersuchen, wo und in welchem Umfang das „getaggte“ aus einer zuvor definierten Quellregion um den Poyang Lake (größter Frischwassersee in China) evapotranspirierte Wasser wieder als Niederschlag zur Landoberfläche zurückkehrt. Um die Bedeutung der individuellen Beiträge der Evapotranspiration zum Niederschlag einschätzen zu können, wurde das verwendete Model erweitert. Die totale Evapotranspiration wurde in direkte Evaporation (bestehend aus der Evaporation von inländischen Wasserkörpern, Evaporation von der obersten Bodenschicht und Evaporation von durch die Vegetation aufgefangenen Niederschlag) und in Transpiration aufgeteilt. Beide Anteile wurden getrennt behandelt und ihre Beiträge zum Niederschlag abgeschätzt (*ET-Tagging Partitioning* Algorithmus).

Da die Verweilzeit von Wasser in der Atmosphäre ein fundamentaler Parameter ist und Informationen zu den Zeitskalen von Evapotranspiration (direkte Evaporation und Transpiration) und Niederschlag liefert, wurde das Modell um einen sogennanten „Age Tracer“-Ansatz erweitert. Dieser neu entwickelte, mit dem „Tracer-Alter“ gewichteter ET-Tagging Partitioning Algorithmus erlaubt es, die atmosphärischen Aufenthaltszeiten von evapotranspiriertem Wasser zu berechnen (separat für direkt evaporiertes Wasser und transpiriertes Wasser) und die Geschwindigkeit der Prozesse im atmosphärischen Zweig des Hydrologischen Kreislaufs einzuschätzen.

Die wichtigsten Ergebnisse sind: Die aus der Poyang See Region stammende Feuchte

trägt in 2005 mit bis zu 1.2 % zu dem jährlichen Niederschlag in Südostchina bei, mit einem Maximum von 6 % in der Nähe der Poyang See Region im Monat August. Eine Budget-Analyse zeigt weiter, dass in 2005 der getaggte Niederschlag in der Quellregion 0.8 %, im Poyang Lake Basin 2.7 % und in Südostchina 10.7 % des in der Quellregion evapotranspirierten Wassers ausmacht. Hinsichtlich der ET-Tagging-Aufteilung ergibt sich, dass direkte Evaporation 64 % und Transpiration 36 % der gesamten „getaggten" Feuchte in 2005 liefert, wobei die mittlere Verweilzeit für beide Anteile rund 36 Stunden beträgt. Die „getaggte" kondensierte Feuchte besteht zu einem großen Teil (69.2 %) aus jüngerem direkt evaporiertem Wasser (mit 7 Stunden Verweilzeit) und zu einem kleineren Teil aus älterem transpiriertem Wasser (mit 11 Stunden Verweilzeit). Ähnliches gilt für den Niederschlag: 69 % des gesamten „getaggten" Niederschlags stammt aus direkter Evaporation mit einer mittleren atmosphärischen Aufenthaltsdauer von 6.6 Stunden, 31 % aus Transpiration von der Vegetation mit einer längere Aufenthaltsdauer von 10.7 Stunden.

Für die Untersuchung von Quelle-Ziel-Beziehungen bei verschiedenen Niederschlagsregimen (feuchte oder trockene Wetterbedingungen) wurde eine quellenspezifische Niederschlagseffizienz eingeführt. In der Untersuchungsperiode überwiegt generell die Niederschlagseffizienz für direkte Evaporation, nur im vergleichbar trockenen August (mit kurzen Verweilzeiten) und in den Wintermonaten (mit kleinen absoluten Transpirationsraten) ist die quellen-spezifische Niederschlagseffizienz für Transpiration größer.

In dieser Arbeit ergeben sich große räumliche und zeitliche Variationen für die „getaggte" Niederschlagsmenge. Es bestehen deutliche Unterschiede darin, wo und wie lange direkte Evaporation und Transpiration zum Niederschlag beitragen. Durch den Einflusses des ostasiatischen Monsoons ändern sich die Muster der atmosphärischen Verweilzeiten des Wassers während des Jahres. Die Ergebnisse zeigen die saisonalen Änderungen in den meteorologischen Bedingungen und die variierenden Interaktionen zwischen Landoberfläche und Atmosphäre. Diese Interaktionen kontrollieren den Jahresgang der einzelnen Beiträge zum Niederschlag und die zugehörigen Feuchteaufenthaltszeiten in der Atmosphäre, was den großen Einfluß von Vegetation und Landnutzung auf den regionalen hydrologischen Zyklus unterstreicht.

Mit dem in dieser Arbeit entwickelten Aufenthaltszeit-gewichteten ET-Tagging Partitioning Algorithmus wurde der unterschiedliche Verbleib von transpiriertem und direkt evaporierten Wasser innerhalb des atmosphärischen Zweigs des hydrologischen Zyklus aufgezeigt. Dieser Algorithmus hat das Potential, auch für Fragestellungen herangezogen zu werden, die sich mit Änderungen (z. B. Beschleunigungen) des hydrologischen Zyklus aufgrund der Klimaänderung befassen.

Chapter 1

Introduction

Water is the medium through which
the atmosphere has most influence on human wellbeing
and terrestrial surfaces have significant influence on the atmosphere.
– – **W. James Shuttleworth (2012)**
"Terrestrial Hydrometeorology"

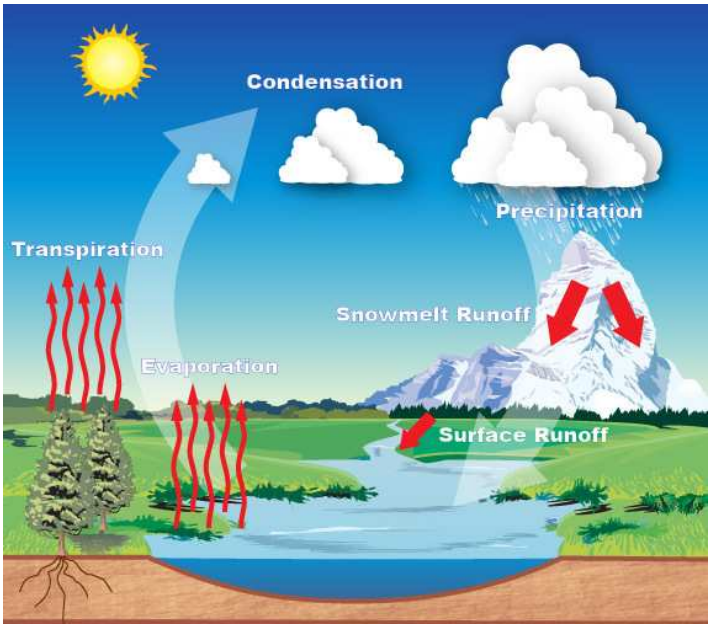

Figure 1.1: Illustration of the atmospheric hydrological cycle (http://www.srh.noaa.gov/jetstream/atmos/hydro.htm).

The hydrological cycle is one main driver for spatially and temporally distributing the water resources on the earth (Oki and Kanae, 2006; Trenberth et al., 2007). Evapotranspiration (ET) and precipitation (P) are the two essential components of the hydrological cycle, which link the terrestrial and atmospheric hydrological processes (see Figure 1.1). Their relationship is crucial for land-atmosphere interaction studies. Moreover, understanding the processes in the hydrological cycle is the foundation to assess these interactions. By now, it is well known that changes to the land surface can significantly alter the atmospheric branch of the hydrological cycle (Huntington, 2006) and can further amplify the climate and climate variability (Karl and Trenberth, 2003; Seneviratne et al., 2006). The relationship between ET and P is highly uncertain and shows a high spatial and temporal variation depending on the regional climate regime (Seneviratne et al., 2010).

1.1 Water Cycle and Moisture Tracking

Studying the fate of the evapotranspired water provides more insights into the interactions between land and atmosphere. The well-established concept of moisture recycling (Budyko, 1974; Savenije, 1995; Eltahir and Bras, 1996) describes the role of local evapotranspiration in the regional atmospheric hydrological cycle, and can be used to distinguish the fate of the evapotranspired water, after staying for a certain time in the local atmosphere, as (i) precipitating water arriving at the local land surface, or (ii) moisture transported to remote regions (Brubaker et al., 1993).

The recycling ratio, defined as the contribution of locally evapotranspired water to total precipitating water, is widely used as an indicator in studies of moisture recycling (Brubaker et al., 1993; Eltahir and Bras, 1994; Trenberth, 1999b; van der Ent et al., 2010; Dominguez et al., 2006; Knoche and Kunstmann, 2013; Alexandre and Gonzalo, 2013). A larger value of the recycling ratio suggests that the regional water balance and subsequently the climate are more sensitive to local land surface processes. Eltahir and Bras (1996), Burde and Zangvil (2001), and Gimeno et al. (2012) give comprehensive reviews that summarize the concepts, describe the governing equations, and reveal the source-sink relationships, respectively.

There are three principal approaches to estimate moisture recycling: (i) physical models (stable water isotopes), (ii) analytical models, and (iii) numerical models (passive water tracers) (Gimeno et al., 2012). These methods may also be combined together to gain improved information on land-atmosphere interaction.

In physical models, environmental tracers (stable water isotopes measured in precipitation such as δ^2H and δ^{18}O) have been employed as a proxy for identifying the

sources of precipitation by examining isotopic fractionation (Kurita et al., 2003; Gimeno et al., 2012). However, intensive collection of isotope data is hard to accomplish, and additional methods such as an analytical model (Kurita et al., 2003) or a numerical model (Joussaume et al., 1984) are often used to gain more detailed information.

Most of the analytical models (also called bulk models) are originated from *Budyko's Model* that was developed by Budyko (1974). This comparatively simple (one-dimensional) model, based on several restrictive assumptions, estimates moisture recycling considering an uniform atmospheric flow structure over the region (Burde et al., 1996). Further developments based on this concept have been made such as the application in a stochastic framework (Entekhabi et al., 1992), extensions from one dimension to two dimensions (Brubaker et al., 1993; Trenberth, 1998, 1999b), and relaxation of certain assumptions (Burde et al., 1996; Schär et al., 1999; Burde and Zangvil, 2001; Mohamed et al., 2005; Dominguez et al., 2006). A detailed description of the most common analytical models used currently are given in the studies of Brubaker et al. (1993), Eltahir and Bras (1994), and Dominguez et al. (2006).

However, the shortcomings as a consequence of simplifying assumptions have significant effects on the estimation of the moisture recycling. For example, Trenberth (1999b) and Bosilovich and Schubert (2001) indicate that simple averaging of estimates for different length scales and timescales may overlook the heterogeneity of the land surface and the temporal variability. Stidd (1967) and Brubaker et al. (1993) also discuss that the assumption "evapotranspired moisture and precipitating moisture is fully mixed in the entire atmospheric column" is not valid in the case of convective events. Consequently, underestimation of moisture recycling has been revealed and discussed in many studies (Eltahir and Bras, 1996; Trenberth, 1999b; Burde and Zangvil, 2001; Bosilovich and Schubert, 2001; Gimeno et al., 2012).

In numerical models, atmospheric moisture tracking with stable water isotopes (Jouzel et al., 1987, 1997; Pfahl et al., 2012) or with water tracers (Sodemann et al., 2009; Knoche and Kunstmann, 2013; Winschall et al., 2014) is an option to couple the evapotranspiration and precipitation processes, in order to characterize the regional precipitation response to local evapotranspiration. The main idea is the consideration of a secondary atmospheric hydrological cycle of those tracers (Sodemann et al., 2009). Numerical atmospheric moisture tracking models are based on explicitly resolved physical processes and on empirically derived parameterizations, and are flexibly operated with different degree of accuracy and detail. The fate of evapotranspired water or the origin of precipitating water can be spatially and temporally determined in an explicit way.

Tracking moisture can be performed either in offline or online mode. For conducting off-line tracking, the basic meteorological parameters (e.g., wind fields, specific

humidity, surface pressure, precipitation, and evapotranspiration) are required and are normally taken from atmospheric analyses or from external meteorological or climatological model outputs. For example, the quasi-isentropic backward trajectories model (*QIBT*) (Dirmeyer and Brubaker, 1999, 2007) tracks water parcels starting from precipitation events, examines the transport in the three dimensional atmosphere, and diagnose surface sources. (Wei et al., 2012a). Based on the same framework of *QIBT*, the application of forward tracking beginning with evapotranspiration has been shown by Tuinenburg et al. (2012). The diagnosis of moisture recycling using one of both models is still subject to the assumption of releasing evapotranspired water into (or drawing precipitating water from) the whole atmospheric column in a distribution according the specific humidity (Wei et al., 2012a). This assumption cannot be validated. Additional shortcomings, for instance, the neglecting of convergence and divergence flow processes for water parcels (Stohl and James, 2004), are also worth to be noted. Another type of two dimensional off-line models, such as the colored moisture analysis algorithm (Yoshimura et al., 2004b) or the water accounting model (*WAM*) (van der Ent et al., 2010), are based on the assumption of the atmospheric water balance and has been used for flexibly estimating the moisture recycling on various scales with a highly computational efficiency. However, due to the limitation of the two dimensional nature, both Goessling and Reick (2013) and van der Ent et al. (2013) show that the presence of directional shear and the frequency of strong moist convection have significant impacts on the estimation. Two off-line Lagrangian particle dispersion models *HYSPLIT*(Draxler, 2003) and *FLEXPART*(Stohl et al., 2005), widely employed in the research field of air quality, have been applied for the studies of moisture recycling as well (Gustafsson et al., 2010; Stohl and James, 2004, 2005). But these two models, diagnosing the net rate of change E - P instand of E or P individually, cannot clearly account for a separation between evapotranspiration and precipitation.

For direct moisture tracking under consideration of dynamical and hydrological processes, atmospheric Eulerian models with a build-in tagging algorithm have been used (Knoche and Kunstmann, 2013; Goessling and Reick, 2013). These extended models allow to tag the moisture evapotranspired from a defined region into the atmosphere and to track it until it returns to the land surface as precipitation. Joussaume et al. (1986) and Koster et al. (1986) introduced the concept of tagging and implemented the tagging algorithm in a global circulation model (*NASA/GISS*) for investigating global sources of local precipitation. This model was applied by Druyan and Koster (1989) in order to identify sources of the Sahel precipitation during dry and wet seasons. Later, Numaguti (1999) used the *CCSR/NIES* AGCM in conjunction with water vapor tracers to examine the origin of precipitation water over the Eurasian continent and to investigate timescale and frequency of recycling processes. Following the same idea, Bosilovich and Schubert (2002) summarized this concept and extended *GEOS-3* GCM. The extended *FVGCM* (Bosilovich et al., 2003) was used for studies on regional

(Bosilovich and Chern, 2006) and global scales (Bosilovich et al., 2005).

Recently, high resolution regional models receive increasing attention due to the fast development in high performance computation. This allows researchers to focus on the identification of precipitation sources on different temporal scales. Event-based rainfall was investigated by using mesoscale models, for example, the High-Resolution Model *CHRM* (Sodemann et al., 2009) and the *COSMO* model (Winschall et al., 2014). In addition, Knoche and Kunstmann (2013) conducted simulations using the Fifth-Generation Mesoscale Model *MM5* with a tagging extension to show the evolution of the tagged moisture field and to reveal details of the transport on a monthly scale.

1.2 Motivation of the Thesis

In this thesis, the evapotranspiration study focus on the Poyang Lake area (N29 °, E116 °) in Southeast China (see Figure 1.2). This lake is the largest freshwater lake in China covering on average a surface area of about 3,500 km^2 and containing a water volume of about 25.2 km^3. It is mainly fed by the inflow from five tributaries in the Poyang Lake basin. The lake and its surrounding wetlands (referred to as the Poyang Lake region) perform crucial hydrologic and ecologic functions for flood control (Shankman et al., 2012) and for maintenance of biodiversity (Jiao, 2009).

Recently, changes in the Poyang Lake level and the associated impacts on water supplies and ecosystems have been investigated extensively on the aspects of both regional climate change and human activities (Zhang et al., 2014a). Liu et al. (2013) detected a decreasing trend of the lake size, based on the analysis of satellite images and hydrological data. In 2006, an abrupt change of the Poyang Lake was identified and directly related to the start of regular operation of the Three Gorge Dams in the same year (Zhang et al., 2012; Liu et al., 2013; Gao et al., 2013). The dam operation induces a decreasing discharge in the downstream Yangtze River at the Poyang Lake outlet, which enhances the outflow of the Poyang Lake to the Yangtze River, particularly during the dry season. Solving the problem of "water loss" or at least minimizing these impacts on the Poyang Lake and its surrounding wetlands is of great concern for local governments (Jiao, 2009; Zhang et al., 2012). Many studies have addressed this issue by investigating the land hydrological and hydraulic processes of the Poyang Lake area (Zhang et al., 2012; Ye et al., 2013; Lai et al., 2014; Zhang et al., 2014a). However, only very few studies attempt to shed light on the "water loss" issue in terms of the atmospheric branch of the hydrological cycle, especially, the fate of water evapotranspired from the Poyang Lake and its surrounding wetlands in the atmosphere.

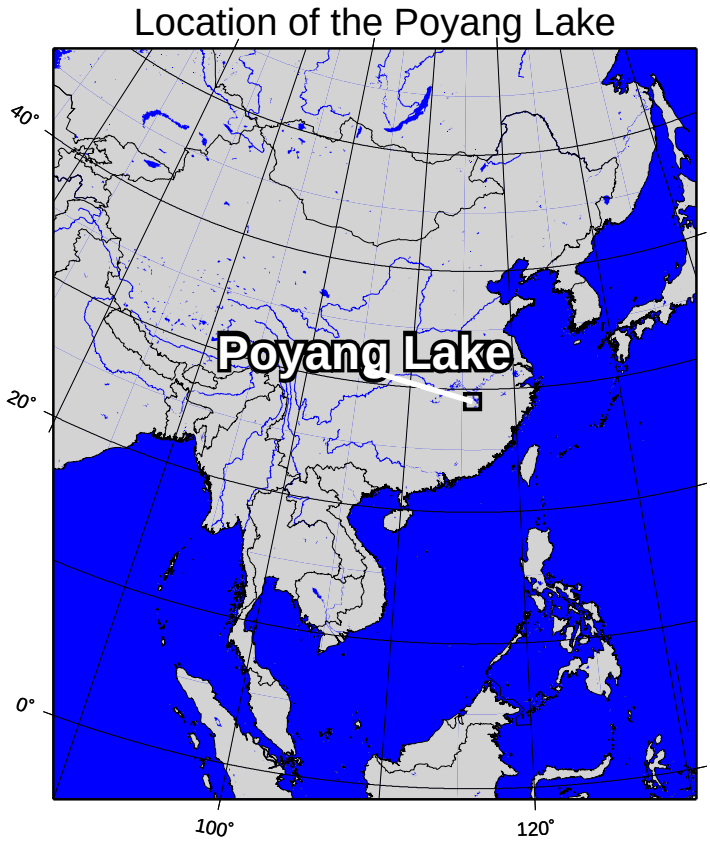

Figure 1.2: Location of the Poyang Lake. Rivers, lakes and the ocean are shown in blue.

Precipitation in China generally shows a large variability in its spatial and temporal distribution, and changes in the frequency and intensity of extremes due to climate change (Liu et al., 2005). In the Poyang Lake basin, the frequency of extreme events such as heavy precipitation, floods and droughts is shown to be increased due to changes in the large-scale circulation (Zhang et al., 2008, 2011a; Shankman et al., 2006) and due to intensive human activities (Ye et al., 2013), resulting in serious hydrological, ecological and economic consequences (Zhang et al., 2014a,b; Xie et al., 2013; Deng et al., 2011). In the study area, the climate is mainly controlled by the subtropical monsoon system (Ding and Chan, 2005). A more detailed description of the climate and the observed climate change in Southeast China is given in Chapter 2.

Land-atmosphere interactions in the Poyang Lake region and their possible influence over Southeast China can be inferred from past research using analytical methods on global scales (Trenberth and Guillemot, 1995; Trenberth, 1998, 1999b) and for the whole of China (Simmonds et al., 1999; Zhou and Yu, 2005).

However, under the conditions of the complex mountainous terrain and the monsoon system in Southeast China, both land surface characteristics and atmospheric features

must be taken into account in the studies of moisture tracking. It has been shown that evapotranspiration (transpiration and evaporation) is considerably affected by land surface characteristics like water bodies, soil, and vegetation (Lawrence et al., 2007; Wang and Dickinson, 2012; Wang-Erlandsson et al., 2014). Two key atmospheric features, which are the presence of the directional wind shear and the fact that situations with strong moisture convection are prevailing (Goessling and Reick, 2013; van der Ent et al., 2013), should be considered in the studies of moisture tracking as well. Consequently, a detailed three dimensional large convection resolving atmospheric model including a sophisticated land surface model for moisture tracking should be employed to gain more insight into the dynamical and hydrological processes. Moreover, atmospheric moisture tracking with moisture tracers in a numerical model is also a straightforward way to characterize the regional response to local evapotranspiration.

Following this idea, a regional climate model (RCM) with an implemented evapotranspiration tagging (ET-Tagging) algorithm is applied in this study. This model allows to tag the moisture evapotranspired from a certain region into the atmosphere and to track it until returning to the land surface as precipitation or leaves the model domain. The ET-Tagging algorithm has been originally implemented by Knoche and Kunstmann (2013) into the Fifth-Generation Mesoscale Model (MM5), and is extended further in this thesis.

1.3 Research Questions

Generally stated, this thesis tries to answer a central hydrological research question:

What is the fate of evapotranspired water from the Poyang Lake region?

With regard to this main research question, three specific sub-questions in this dissertation are addressed:

- Where does the evapotranspired water from the Poyang Lake region go?
- How important are the individual contributions of the two components of evapotranspiration fluxes, i.e., the transpiration flux and the direct evaporation flux, for the subsequently ET-driven precipitation?
- How long is the lifetime (i.e., atmospheric residence times) between the original evapotranspiration (transpiration and direct evaporation) and the returning of water masses to the land surface as precipitation?

1.4 Innovation

Innovative work in this dissertation consists of:

- Parallelization of the evapotranspiration tagging code that allows to conduct long-term simulations to investigate the intra-annual/seasonal variability
- Development of an evapotranspiration tagging partitioning algorithm that allows to separately track the moisture components of transpiration and direct evaporation
- Development of an age-weighted evapotranspiration tagging partitioning algorithm that allows to calculate the atmospheric water residence times of transpired water, of direct evaporated water, and of total evapotranspired water
- Application of the methods to the mountainous Poyang Lake region in subtropical Southeast China
- Analysis of the source-target relations by introducing a source-specific precipitation efficiency.

Chapter 2

Study Area

2.1 Climatology of Southeast China

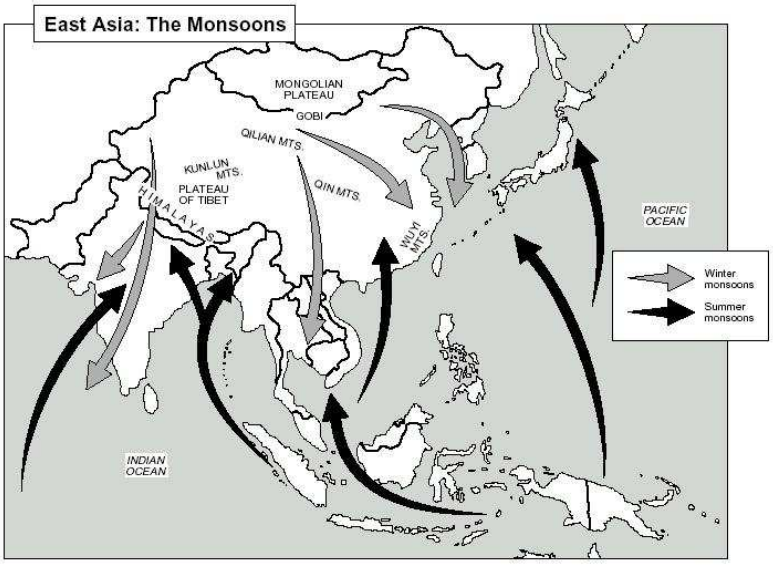

Figure 2.1: Schematic overview of the main atmospheric moisture transporting streams in winter (gray arrows) and summer (black arrows) (`http://climatic-changes.blogspot.de/2012_02_01_archive.html`).

Large Scale Dynamics The East Asian monsoon system determines the regional climate of China (Trenberth et al., 2000; Zhu and Chen, 2002). In winter, the monsoon system is closely connected to the Siberian high in the North and cool, dry moisture is transported by the prevailing northeasterly winds (Wu et al., 2006) (Figure 2.1). In summer, the main low-level streams transport moisture towards China (Chow

et al., 2008), the origin is temporally varying between the Indian Ocean and the Bay of Bengal, the South China Sea, and the western North Pacific Ocean (Figure 2.1). The consequences of the monsoons' effects on the climatic characteristics of Southeast China and the Poyang Lake region are described in the following paragraphs.

Temperature The mean annual temperature over Southeast China ranges from 15 ℃ in the North to higher than 20 ℃ in the Southeast close to the South Asian Sea (You et al., 2011). Figure 2.2 shows the spatial distribution and the annual cycle of temperature. The mean annual temperature generally decreases from the southeastern coast line to the northwestern mountainous region due to the topography and the latitude (Figure 2.2a). Averaged over Southeast China, the lowest monthly mean temperature is found in January (∼ 6 ℃), while the highest temperature occurs in July (∼ 28 ℃) (Figure 2.2b).

With respect to global warming, the mean surface air temperature in China increased from 1955 to 2000 with an accelerating trend after 1990 (Liu et al., 2004b). The warming rate of the annual mean temperature is 0.27 ℃/decade during 1961-2003 (You et al., 2011). In general, the change of the temperature extremes often follows the trend of the mean surface air temperature. However, in Southeast China, the significant increase in daily minimum temperature and the slight decrease in daily maximum result in the narrowing diurnal temperature range (DTR), especially in the boreal winter season (Dai et al., 1997; Easterling et al., 1997; Shen and Varis, 2001; Liu et al., 2004b).

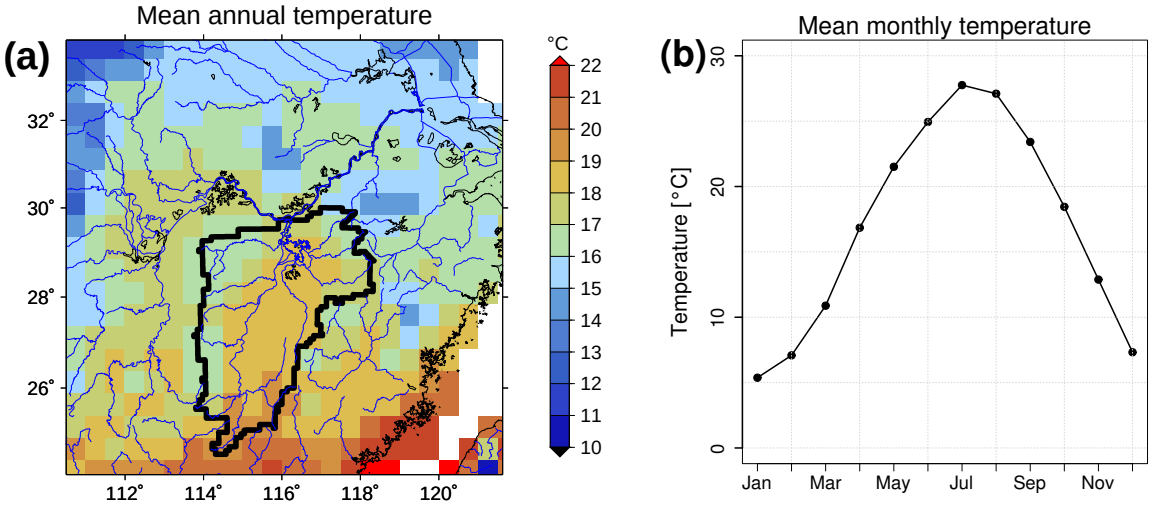

Figure 2.2: (a) Distribution of the mean annual temperature [℃] over Southeast China and (b) annual cycle of the mean monthly temperature [℃] averaged over Southeast China, for 1980-2007 (Data source: CRU at 0.5 ° × 0.5 ° resolution). The Poyang Lake basin is also indicated by the black frame in (a).

Precipitation Figure 2.3a illustrates the spatial distribution of the long-term mean annual precipitation in Southeast China. The southeast-northwest precipitation gradient is pronounced. The total amount of mean annual precipitation are ranging from less than 600 mm in the northwest of Southeast China to more than 2000 mm in the area close to the Poyang Lake basin. The annual cycle of precipitation (see Figure 2.3b) is dominated by the strength of the East Asian summer monsoon (Ding and Chan, 2005). The rainy period (here, from April to June) mainly comes into being during prevalence of the summer monsoon.

In the last 40 years, the observed trend of precipitation amount in China varies largely by season and region, and an increase of frequency and intensity of extreme precipitation events are detected as well (Liu et al., 2005). Gemmer et al. (2004) found that, in the last decades, precipitation in China increases in winter and summer and decreases in spring and autumn. Especially, significant increasing of summer precipitation is found in Southeast China (Ye, 2013). The possible reason for increasing precipitation variability at monthly scales is the weakening trend of East Asian summer monsoon (Xu et al., 2006b), which results from the increasing geopotential height over Mongolia, North China, and west Pacific regions (Wang and Zhou, 2005; Zhang et al., 2009; You et al., 2011).

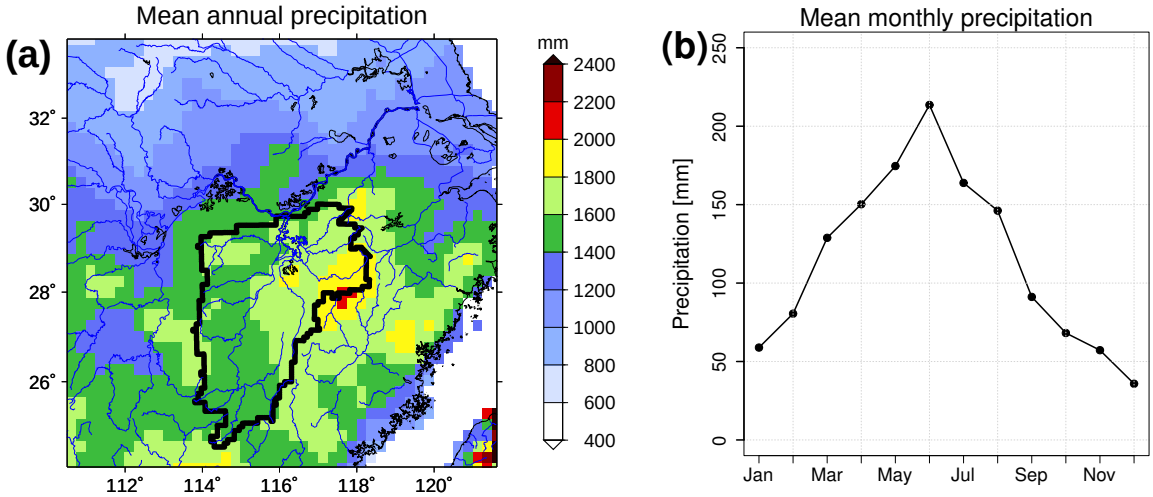

Figure 2.3: (a) Distribution of the mean annual precipitation [mm] over Southeast China and (b) annual cycle of the mean monthly precipitation [mm] averaged over Southeast China, for 1980-2007 (Data source: APHRODITE at 0.25 ° × 0.25 ° resolution). The Poyang Lake basin is also indicated by the black frame in (a).

Evapotranspiration The mean annual evapotranspiration rate varies between around 600 mm in the North, and more than 900 mm in the South and along the coast line (Figure 2.4a). The evapotranspiration rate is closely connected to the seasonal

variation of the overall meteorological conditions. In general, higher temperature, more available soil moisture, and higher wind speeds during the summer monsoon season (i.e., from May to August) enhance the local evapotranspiration (Figure 2.4b).

Since there is a complementary relationship between terrestrial evapotranspiration (directly related to the latent heat flux) and pan evaporation (mainly related to sensible heat flux) (Brutsaert and Parlange, 1998; Ohmura and Wild, 2002), normally the trends of terrestrial evapotranspiration and pan evaporation should also oppositely change. In Southeast China, the trend of pan evaporation from measurements statistically decreases from 1960 to 2000 (Liu et al., 2004a; Xu et al., 2006a). However, the same decreasing trend of terrestrial evapotranspiration, estimated by the Penmann-Monteith method, is shown in Gao et al. (2007). This phenomena, so called "pan evaporation paradox" (Peterson et al., 1995; Roderick and Farquhar, 2002), is extensively investigated over many study areas in China (Liu et al., 2004a; Xu et al., 2006a; Gao et al., 2007). It is mainly caused by a significant decrease in the net radiation due to air polluting (Menon et al., 2002; Tie and Cao, 2009) and, to a lesser extent, due to a significant decrease in the wind speed in summer and winter (Xu et al., 2006b).

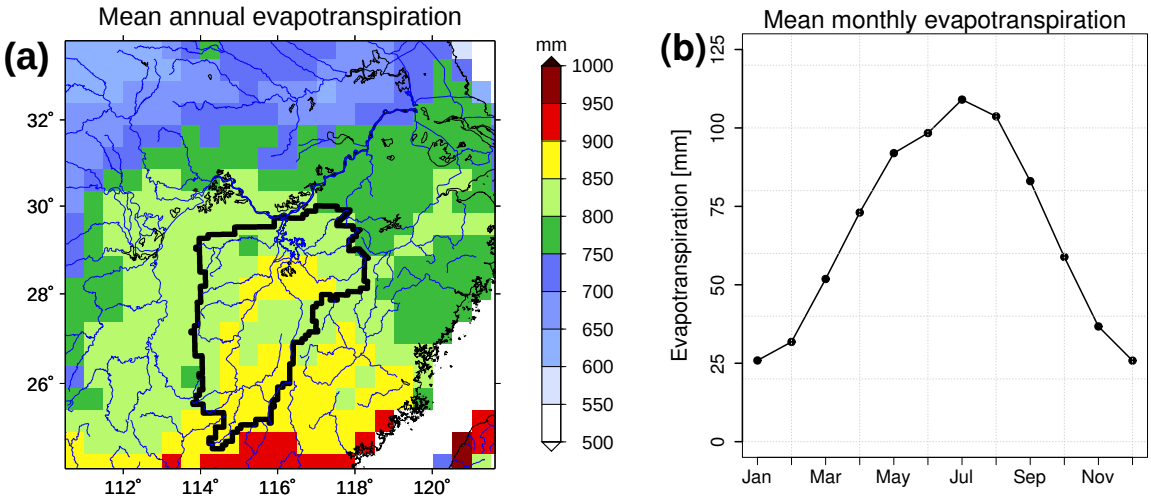

Figure 2.4: (a) Distribution of the mean annual evapotranspiration [mm] over Southeast China and (b) annual cycle of the mean monthly evapotranspiration [mm] averaged over Southeast China, for 1982-2007 (Data source: FLUXNET-MTE at 0.5° × 0.5° resolution). The Poyang Lake basin is also indicated by the black frame in (a).

2.2 Hydrology of the Poyang Lake Basin

River Basin The Poyang Lake basin is located in the center of Southeast China and covers in total an area of $1.6 \times 10^5\,\mathrm{km}^2$ (Sun et al., 2012). The topography varies

from higher than 2000 m a.s.l. in the South to lower than 50 m a.s.l. around the lake. The Poyang Lake basin encompasses five sub-basins of the Xiushui River, Ganjiang River, Fuhe River, Xinjiang River, and Raohe River (Figure 2.5).

The Poyang Lake (29 °N, 116 °E) is the largest freshwater lake in China covering on average an area of 3500 km^2 in a hydrological normal year, but varies dramatically from 907.7 to 3,752.7 km^2 in history (Liu et al., 2013). The fluctuation of the lake area are controlled by the discharges from the five tributaries in this catchment and the outflow into the Yangtze River (Ye et al., 2011). From a hydrological perspective, this lake is an important flood storage and detention area along the Yangtze River (Shankman et al., 2012). To protect its abundant biodiversity, Poyang Lake National Nature Reserve adjacent to the Yangtze River provides habitats for migratory birds and endangered white cranes (Jiao, 2009).

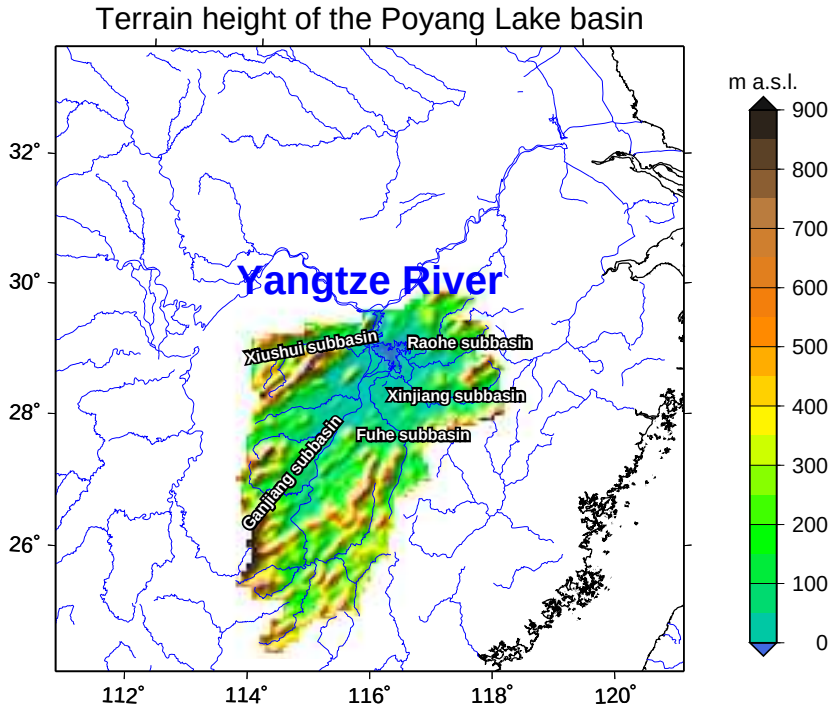

Figure 2.5: Topography (m a.s.l.) of the Poyang Lake basin and locations of the five sub-basins. The Poyang Lake and rivers are shown in blue.

Due to changes in the large-scale circulation observed during the period from 1960 to 2005 (Shankman et al., 2006; Zhang et al., 2008, 2011a) and due to intensive human activities (Ye, 2013), the frequency of extreme events such as heavy precipitation, floods and droughts increases in the Poyang Lake basin, and further result in serious hydrological, ecological and economic consequences (Zhang et al., 2014a,b; Xie et al., 2013; Deng et al., 2011).

Discharge The high inter-annual variability of discharge in the Poyang Lake basin strongly depends on changes in precipitation (Zhang et al., 2011a). As a response to the positive trend of precipitation in summer and winter, the corresponding discharge increases as well during the investigation period from 1995 to 2005 (Zhang et al., 2011a), and possibly becomes more extreme in the future (Ye et al., 2011).

Floods and Droughts On a global scale, continuously increasing risk of extreme floods due to climate change has been observed in the past and is expected to continue in the future (Milly et al., 2002; Hirabayashi et al., 2013). As reported in China's National Assessment Report on Climate Change (Lin et al., 2007), flooding becomes also more severe in Southeast China. In the Poyang Lake basin, the frequency of severe floods has significantly increased (Shankman et al., 2006).

Regarding droughts, there is no obvious trend in the size of drought areas over Southeast China (Zou et al., 2005). However, the frequency and the severity of droughts in this region show a positive trend in the past and is predicted to last in the near future (Sheffield et al., 2012; Zou et al., 2005; Zhai et al., 2010). For example, severe droughts in 2006, 2011, and 2012 in the Poyang Lake basin have drawn extensive attentions nationally and worldwide (Feng et al., 2012).

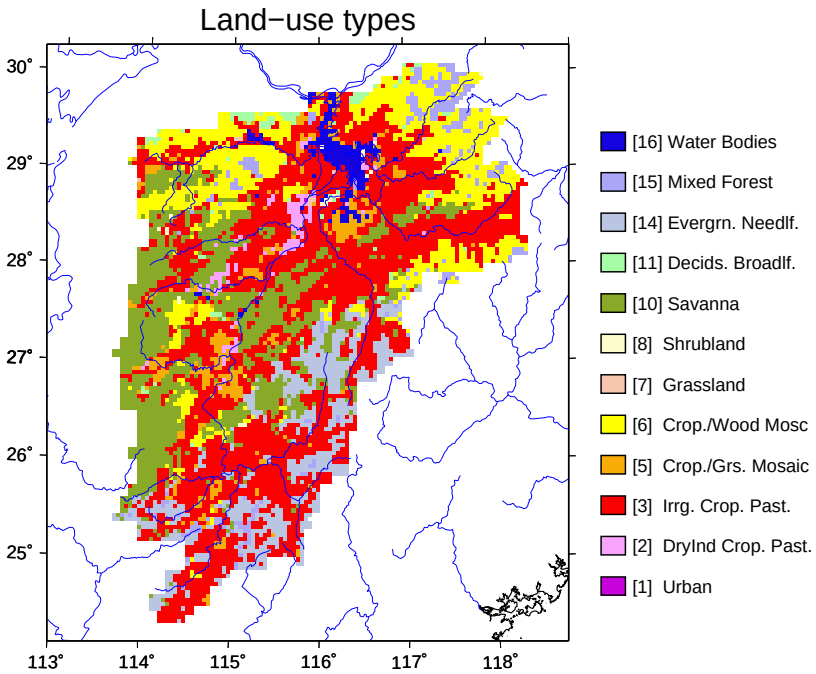

Figure 2.6: Spatial distribution of the land-use types for the Poyang Lake basin with a horizontal resolution of 4.5 km based on the global 25-category data from the U.S. Geological Survey (USGS). The Poyang Lake and rivers are shown in blue.

Land Use Land use in the Poyang Lake basin consists of forest (46 %), shrub land (25 %), crop land (25 %) and small areas of pasture, urban centers and open water (4 %) (Ye et al., 2011; Zhang et al., 2014a) (Figure 2.6). For forest, the originally (i.e., before 1980) observed negative trend changes to a currently (i.e., 1980-2005) positive trend influenced by the Chinese forest policy (Liu and Tian, 2010). Meanwhile, the trend change of cropland follows the opposite direction (i.e., from expanding to shrinking). Since irrigated crop (i.e., paddy rice) around the lake is the prime vegetation type, the increasing quantity of agricultural water with considerably less water use efficiency changes the available water resources (Wu et al., 2010; Zhu et al., 2013). Based on the analysis of satellite images and hydrological data, recently, Liu et al. (2013) revealed a decreasing trend of the lake size.

Chapter 3

RCM-Based ET-Tagging Algorithm

In this chapter, a MM5-based Eulerian model with a build-in evapotranspiration tagging algorithm is described. The tagging algorithm allows to tag the moisture evapotranspired from a given region and to follow the pathways across the atmosphere until the tagged moisture returns to the land surface as precipitation or leaves the model domain. The algorithm accounts for all water transport processes and phase transitions. It can be used to explicitly quantify the contribution of regional evapotranspiration to precipitation with properly handling the problems of the presence of vertical wind and vertical wind shear. Additionally, further extensions of the model concerning the partitioning of evapotranspiration into transpiration and direct evaporation and the age-weighting of the tagged atmospheric moisture are described. It enables the assessment of the contribution of the individual evapotranspiration components on precipitation and the atmospheric moisture residence times. With these extensions, the RCM allows to characterize and quantify the regional atmospheric cycle in terms of magnitude, location, and timescale.

Firstly, a brief overview of the basic 3-D regional climate model (MM5) and some discussions of the basic features are given. Then the implementation of the ET-Tagging algorithm in MM5 is described. The additional extensions (ET-Tagging partitioning and age-weighting) are subsequently presented.

3.1 The Basic RCM MM5

In this thesis, the Fifth-Generation Mesoscale Model *MM5* (Dudhia, 1993; Grell et al., 1994) version 3.5 is used as the basic model for the implementation of an ET-Tagging algorithm. The MM5 modeling system, developed at the Pennsylvania State Uni-

versity and National Center for Atmospheric Research, addresses the simulation of dynamics of land surface (e.g., soil, snow cover, and vegetation) and atmosphere. This process-based, non-hydrostatic limited-area model has been applied extensively for short-period weather prediction and long-term climatological assessment at synoptic and sub-synoptic scales. Applied as a dynamical downscaling tool (Wilby and Wigley, 1997), the model can bridge the gap between large-scale information (i.e., the input data of MM5) and local information (i.e., the output data of MM5).

MM5 uses a horizontal grid with an Arakawa-Lamb B-grid staggering, based on a Lambert Conformal, Polar Stereographic, or Mercator map projection. In the vertical direction, a terrain-following coordinate σ is used, defined as

$$\sigma = (p_0 - p_t)/(p_{s0} - p_t) \tag{3.1}$$

where p_0 is a hydrostatic reference-state pressure, p_t is a specified constant model top pressure, and p_{s0} is the reference-state surface pressure.

Beside the simulation program MM5, the whole modeling system contains three further important programs: as the beginning program, TERRAIN horizontally interpolates the regular latitude-longitude terrain height and land surface information (e.g., land use, land-water mask, soil types, vegetation fraction, and time-constant deep-soil reference temperature) onto the chosen model grid. REGRID collects archived gridded meteorological data needed for initial conditions and lateral atmospheric and sea surface boundary conditions (i.e., SST). The deep-soil reference temperature field generated by TERRAIN is used as lower soil boundary condition for MM5.

The meteorological data are provided by either external simulations (e.g., simulations of general circulation model) or reanalysis (e.g., ERA-Interim). They are horizontally interpolated from the original grid to the model grid by REGRID, too. Then, INTERPF deals with the vertical interpolation from pressure levels to model σ levels.

Model Physics MM5 accounts for, among other physical processes, atmospheric diffusive and turbulent processes, short- and long-wave radiation, phase transitions of water substance, and the formation of precipitation. For each physical mechanism a variety of different parametrizations and options are available. In the following, a short introduction to the physical treatments is given and the configurations employed for this study are described.

Planetary Boundary Layer (PBL) physics handle subgrid-scale vertical transports by various-sized eddies and turbulence (Dudhia, 2014), and are critical to prediction of meteorological variables (Han et al., 2008). For PBL modeling and turbulence parameterization, the revised Medium-Range Forecast model (MRF-PBL) (Hong and Pan,

1996) is chosen for this study. A computationally efficient nonlocal vertical diffusion scheme, implemented into MRF, allows to simulate the processes of vertical diffusion of temperature, moisture and momentum and to calculate the height of the PBL. It works in coordination with a land-surface model (LSM) by exchanging heat and moisture fluxes at the interface between atmosphere and soil.

Incoming solar radiation is the main driver of the climate system (Trenberth and Stepaniak, 2004). Radiation processes interact with the atmosphere, with cloud and precipitation fields, and with the land surface (Dudhia, 1989). For the calculations of the atmospheric short- and long-wave radiation the cloud-radiation short-wave scheme (Dudhia, 1989) and the Rapid Radiative Transfer Model (RRTM) long-wave scheme (Mlawer et al., 1997) are selected. The Dudhia scheme explicitly calculates the clear-air and clouds downward shortwave fluxes, considering the effects of solar zenith angle, and is sophisticated enough so that little memory is required. RRTM utilizes the correlated-k method to efficiently obtain the accurate representations of long-wave processes, which is suitable for climate studies.

The explicit microphysical parametrization is used for calculation of grid-scale cloud and precipitation processes including conversion between gaseous, liquid, and solid phases of water and associated energy changes. In MM5 the Reisner-1 Mixed-Phase scheme (Reisner et al., 1998), that treats the model atmosphere as composed of five hydrometer species: water vapor, cloud water, cloud ice, rain water, and snow, is selected. For their evolution, time- and spatial-dependent three-dimensional mixing ratios (kg kg^{-1}) are used as prognostic variables shown in Table 3.1.

Table 3.1: Atmospheric moisture components (kg kg^{-1}) used in the chosen Reisner-1 Mixed-Phase scheme.

Notation	Description
q_v	mixing ratio of water vapor (gas phase)
q_c	mixing ratio of non-precipitating liquid water substance (cloud droplets)
q_i	mixing ratio of non-precipitating solid water substance (could ice particles)
q_r	mixing ratio of precipitating liquid water substance (rain droplets)
q_s	mixing ratio of precipitating solid water substance (snow flakes and other solid form)

The land-surface model is capable of simulating surface/subsurface energy and water fluxes and the corresponding budget changes in response to near-surface atmospheric forcing (Ek et al., 2003). It describes processes of soil thermodynamics, soil hydrology, and snow-ice hydrology, that relate to vegetation and snow cover (Chen and Dudhia, 2001; Dudhia, 2014). For this study, the Oregon State University Land Surface Model (OSU-LSM) (Chen et al., 1996; Chen and Dudhia, 2001) is used. The

advanced model, originally developed by Pan and Mahrt (1987), was extended further by Chen et al. (1996), and recently becomes a community land surface model Noah-MP with multiparameterization options (Niu et al., 2011; Yang et al., 2011). This fully developed one-dimensional soil-vegetation-atmosphere transfer model accounts for energy and water transferred among four soil layers (with a thickness of 10, 30, 60, and 100 cm), simultaneously, interacting with processes in lower atmosphere. For vegetated surface, evapotranspiration and interception and reevaporation is taken into account.

Basic Governing Equations for Humidity The non-hydrostatic MM5 model is based on a set of three-dimensional equations, including the prognostic equations for momentum, temperature, and various water components. The prognostic model equation governing the evolution of the water components is

$$\frac{\partial}{\partial t}(p^* q_k) = \underbrace{-\left\{ m^2 \left[\frac{\partial (p^* q_k m^{-1} u)}{\partial x} + \frac{\partial (p^* q_k m^{-1} v)}{\partial y} \right] + \frac{\partial (p^* q_k \dot{\sigma})}{\partial \sigma} \right\}}_{\textbf{Grid-scale transport (Pseudo flux)}}$$

$$\underbrace{+ q_k \cdot \left\{ m^2 \left[\frac{\partial (p^* m^{-1} u)}{\partial x} + \frac{\partial (p^* m^{-1} v)}{\partial y} \right] + \frac{\partial (p^* \dot{\sigma})}{\partial \sigma} \right\}}_{\textbf{Grid-scale transport (Divergence)}}$$

$$+ \underbrace{SUB(q_k)}_{\textbf{Subgrid-scale transport}} + \underbrace{p^* C_k}_{\textbf{Phase transitions}} + \underbrace{PRC(q_k)}_{\textbf{Precipitation effect}} \tag{3.2}$$

where q_k denotes the various mixing ratios (summarized in Table 3.1) coupled with $p^* = p_{s0} - p_t$. P^* (Pa) is the time invariant difference between the reference pressure p_{s0} at the surface and the pressure p_t at the model top. x (m) and y (m) are the two horizontal coordinates and the dimensionless variable σ is a generalized vertical coordinate with $\dot{\sigma}$ (s^{-1}) as its time derivative. u (m s^{-1}) and v (m s^{-1}) are the two horizontal wind velocities. m is the map projection factor.

SUB (Pa kg kg^{-1} s^{-1}), $p^* C_k$ (Pa kg kg^{-1} s^{-1}), and PRC (Pa kg kg^{-1} s^{-1}) represent the subgrid-scale transport, the phase transitions, and the downward transport of precipitating water substances, respectively. The advection in equation (3.2) is formulated in a pseudo flux form (first term on the right side) together with an associated compensating divergence term (second term). The phase transition rates C_k of the five water components represent 16 different processes used in the explicit moisture scheme (Table 3.2). A concentration-weighted falling speed of precipitating process is calculated iteratively in each model time step.

The numerical solution of equation (3.2) is computed on a rectangular-structured staggered grid by finite difference schemes. The spatial differencing employs a second-order centered scheme, and the temporal differencing consists of leapfrog steps with an Asselin filter scheme used to avoid a splitting of the solution (Dudhia, 1993).

3.2 ET-Tagging Algorithm

The concept of the ET-Tagging algorithm is to add a second numerical formulation of the atmospheric hydrological cycle to a RCM (Sodemann et al., 2009; Winschall et al., 2012; Sodemann and Stohl, 2013; Winschall et al., 2014), i.e., a cycle for the tagged moisture. Evapotranspiring water from a selected region is "tagged" when entering the atmosphere. Then, the tagged moisture undergoes the same atmospheric processes as the total moisture.

For the description of the MM5-based ET-Tagging algorithm I closely follow the study of Knoche and Kunstmann (2013). For brevity it is briefly summarized.

In this MM5 ET-Tagging environment, as realized in Knoche and Kunstmann (2013), a mask is defined over the whole model domain for separating a selected source area from its surroundings:

$$MASK_{tag} = \begin{cases} 1 & \text{for tagging source area} \\ 0 & \text{otherwise} \end{cases} \tag{3.3}$$

Upward ET fluxes ($ET > 0$) entering the lowest atmospheric model layer from the source area contribute to the tagged water vapor. Downward fluxes of tagged water vapor, i.e., tagged dew formation, are also considered. The tagged downward fluxes ET_{tag} (i.e., tagged dew formation) are proportional to the total downward fluxes ET ($ET < 0$) and the fraction of tagged water vapor $q_{v,tag}^{lowest}$ to total water vapor q_v^{lowest} in the lowest model layer:

$$ET_{tag} = \begin{cases} ET \cdot MASK_{tag} & \text{if } ET \geq 0 \\ ET \cdot q_{v,tag}^{lowest} / q_v^{lowest} & \text{if } ET < 0 \end{cases} \tag{3.4}$$

For tracking the tagged water pathways through the atmosphere, new model variables representing the tagged water substances are defined. Corresponding to the five mixing ratios q_v, q_c, q_i, q_r, and q_s of the original moisture components (see Table 3.1), new mixing ratios $q_{v,tag}$, $q_{c,tag}$, $q_{i,tag}$, $q_{r,tag}$, and $q_{s,tag}$ of the tagged moisture components are added. The original moisture variables keep unchanged and represent the total moisture including tagged and untagged moisture quantities.

Accordingly, the original MM5 moisture equations describing grid-scale transport, subgrid-scale transport due to turbulence and diffusion, phase transitions, and the downward transport of precipitating water components are duplicated in the code. The original equation set (equation 3.2) accounts for the total moisture components, while the new second equation set (equation 3.5) is for the tagged moisture components.

$$\begin{aligned}\frac{\partial}{\partial t}(p^* q_{k,tag}) = &-\left\{ m^2 \left[\frac{\partial (p^* q_{k,tag} m^{-1} u)}{\partial x} + \frac{\partial (p^* q_{k,tag} m^{-1} v)}{\partial y} \right] + \frac{\partial (p^* q_{k,tag} \dot{\sigma})}{\partial \sigma} \right\} \\ &+ q_{k,tag} \left\{ m^2 \left[\frac{\partial (p^* m^{-1} u)}{\partial x} + \frac{\partial (p^* m^{-1} v)}{\partial y} \right] + \frac{\partial (p^* \dot{\sigma})}{\partial \sigma} \right\} \\ &+ SUB(q_{k,tag}) + p^* C_{k,tag} + PRC(q_{k,tag}) \end{aligned} \tag{3.5}$$

In both equation sets, identical advection velocities and turbulence intensities are applied for the transport schemes. Analogously to the phase transition rates C_k between the total moisture components, the phase transition rates $C_{k,tag}$ between the tagged moisture components are combinations of single rates $C_{\alpha\to\beta,tag}$ for the various transition processes:

$$C_{k,tag} = \underbrace{\sum_{\substack{\alpha \\ \beta=k}} C_{\alpha\to\beta,tag}}_{gain} - \underbrace{\sum_{\substack{\beta \\ \alpha=k}} C_{\alpha\to\beta,tag}}_{loss} \tag{3.6}$$

Each single rate $C_{\alpha\to\beta,tag}$ is proportional to the original transition rate $C_{\alpha\to\beta}$ and the fraction $q_{\alpha,tag}/q_\alpha$ of the tagged part $q_{\alpha,tag}$ and the corresponding total part q_α:

$$C_{\alpha\to\beta,tag} = C_{\alpha\to\beta} \cdot q_{\alpha,tag}/q_\alpha \tag{3.7}$$

Table 3.2 summarizes the 16 different processes considered by the explicit moisture scheme *Reisner 1*. The corresponding ratios are calculated in the way shown in the third column. Also, the concentration-weighted fall velocity is the same for tagged and total precipitating particles, only determined by the total content of rain and snow substances, respectively.

The tagged ET fluxes ET_{tag} at the land surface appear implicitly as boundary values for the atmospheric subgrid-scale fluxes $SUB(q_{k,tag})$. A tagged water substance can partly fall out as precipitation $PRC(q_{k,tag})$, or can leave the atmosphere through outflow at the lateral model domain boundaries. Returning originally tagged water from outside of the model domain is not taken into account in this algorithm. Also, processes of subsurface tagged moisture are ignored.

The same numerical scheme for the advection of the tagged moisture as for the advection of the total moisture field is used to achieve numerical consistency. Since

numerical problems on tagged moisture components (e.g., negative values for the condensed tagged moisture variables) can raise due to the non-mass conservation advection scheme, positive definiteness and additional criteria for the ratios of tagged to total moisture quantities are carefully handled.

Table 3.2: Phase transition processes in the explicit moisture scheme *Reisner 1* (Reisner et al., 1998; Knoche and Kunstmann, 2013).

Phase transition processes		Description	
Water vapor q_v	→ Cloud water q_c	Cloud condensation	
	→ Cloud ice q_i	Initiation to cloud ice	
	→ Cloud ice q_i	Deposition to cloud ice	$q_{v,tag}/q_v$
	→ Rain water q_r	Condensation to rain	
	→ Snow q_s	Deposition to snow	
Cloud water q_c	→ Water vapor q_v	Evaporation of cloud water	
	→ Rain water q_c	Autoconversion to rain	$q_{c,tag}/q_c$
	→ Rain water q_c	Collection of cloud water by rain	
	→ Snow q_s	Collection of cloud water by snow	
Cloud ice q_i	→ Water vapor q_v	Sublimation of cloud ice	
	→ Rain water q_c	Autoconversion to snow	$q_{i,tag}/q_i$
	→ Rain water q_c	Accretion of snow by cloud ice	
Rain water q_r	→ Water vapor q_v	Evaporation of rain	$q_{r,tag}/q_r$
Snow q_s	→ Water vapor q_v	Sublimation of snow	
	→ Rain water q_c	Evaporation of melting snow	$q_{s,tag}/q_s$
	→ Rain water q_c	Melting of snow	

Additionally, the source codes of the ET-Tagging extensions is parallelized, on the basis of OpenMP, in order to achieve the high performance for the following simulations (see the detailed description in Appendix A). More details about the implementation of the ET-Tagging algorithm into the MM5 model are given in Knoche and Kunstmann (2013).

It should be noted that there is an alternative way of parameterizing tracer evapotranspiration using the moisture gradient of the individual tracers (e.g., Sodemann et al. (2009)). Detailed comparisons and discussions of the two methods are given in Winschall et al. (2014) and Goessling and Reick (2013).

3.3 ET-Tagging Partitioning Algorithm

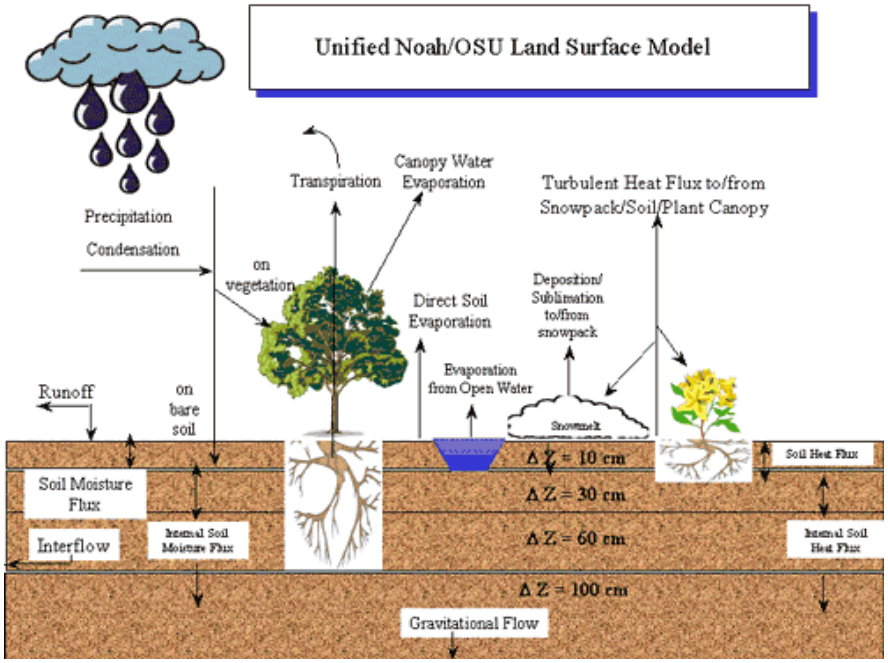

Figure 3.1: A schematic representation of the OSU-LSM in MM5 (http://www.ral.ucar.edu/research/land/technology/lsm.php).

For the assessment of the contribution of the individual ET components on precipitation, additional model extensions concerning the partitioning of ET are introduced. Principally, the ET in the model domain consists of evaporation from inland water bodies E_{water}, evaporation from the top shallow soil layer including one layer of snow E_{soil}, evaporation of precipitation intercepted by the canopy $E_{interception}$, and transpiration by vegetation E_t:

$$ET = E_{water} + E_{soil} + E_{interception} + E_t \tag{3.8}$$

Figure 3.1 illustrates all the processes of the soil thermodynamics and soil hydrology in the OSU-LSM (Chen et al., 1996; Chen and Dudhia, 2001), coupled with the MM5 model. E_{water} is governed by a Penman-based energy balance approach for potential evaporation. E_{soil} depends on soil moisture content and potential evaporation, and $E_{intercption}$ is determined by the intercepted canopy water content and potential evaporation. E_t is calculated mainly by considering green vegetation fraction, potential evaporation, and soil moisture in the root zone. A detailed description of the land-surface model is given in Chen and Dudhia (2001).

In this study, the model is extended to partition the evapotranspiration flux ET

into a direct evaporation flux E_d

$$E_d = E_{\text{water}} + E_{\text{soil}} + E_{\text{interception}} \tag{3.9}$$

and the transpiration flux E_t

$$ET = E_d + E_t. \tag{3.10}$$

These two fluxes are tracked separately in the framework of the ET-Tagging algorithm in order to explicitly quantify the contribution of direct evaporation and transpiration to precipitation.

Since only values of the total ET fluxes are contained in the output of MM5, new variables with respect to the two partitions E_d and E_t were defined for the ET partitioning option. More details about the implementation of the ET-Tagging partitioning within the framework of the ET-Tagging algorithm are given in Appendix B. It sheds light on (i) the organization and the order in which exact routines are called, and (ii) the routines where changes of source code are needed.

3.4 Age-Weighted ET-Tagging Algorithm

For the calculation of atmospheric water residence times (age of the moisture in the atmosphere), additional model extensions concerning the "age weighting" are introduced. Analogously to the implementation of the ET-Tagging algorithm into a RCM by adding a second atmospheric hydrological cycle for the tagged moisture, additional time information can be gained by adding a *third* atmospheric "hydrological" cycle information in the RCM code accounting for the age-weighted tagged moisture. New model variables representing the age-weighted tagged water components are defined and an additional equation set controlling the evolution of the age-weighted tagged water components is formulated.

The original MM5 moisture equations describing grid-scale transport, subgrid-scale transport due to turbulence and diffusion, phase transitions, and the downward movement of precipitating water components are duplicated again in the code. Besides the original equation set (see equation 3.2) for the total moisture components q_k and the second equation set (see equation 3.5) for the tagged moisture components $q_{k,tag}$ in the extended MM5 model, the new third equation set accounts for the age-weighted tagged

moisture components $q_{k,age}$ (kg kg^{-1} s) and is as follows:

$$\begin{aligned}\frac{\partial}{\partial t}(p^* q_{k,age}) = &-\left\{ m^2 \left[\frac{\partial (p^* q_{k,age} m^{-1} u)}{\partial x} + \frac{\partial (p^* q_{k,age} m^{-1} v)}{\partial y} \right] + \frac{\partial (p^* q_{k,age} \dot{\sigma})}{\partial \sigma} \right\} \\ &+ q_{k,age} \left\{ m^2 \left[\frac{\partial (p^* m^{-1} u)}{\partial x} + \frac{\partial (p^* m^{-1} v)}{\partial y} \right] + \frac{\partial (p^* \dot{\sigma})}{\partial \sigma} \right\} \\ &+ SUB(q_{k,age}) + p^* C_{k,age} + PRC(q_{k,age}) + S_{k,age} \end{aligned} \tag{3.11}$$

$S_{k,age}$ (s) denotes the source term due to advancing time for the age-weighted tagged moisture components. The transition rates $C_{k,age}$ (kg kg^{-1} s^{-1} s) are proportional to the original transition rates C_k and the ratio of age-weighted tagged moisture components $q_{k,age}$ to original total moisture components q_k

$$C_{k,age} = C_k \cdot q_{k,age} / q_k. \tag{3.12}$$

For the solution of the differential equation (3.11) a time splitting scheme is applied to increase efficiency of computation. Firstly, the equation without the term $S_{k,age}$ is integrated to obtain a preliminary age-weighted tagged moisture components $q^{n*}_{k,age}$ from previous time step n due to atmospheric transport and phase change processes. The spatial and temporal finite differencing schemes for equation (3.11) are the same as for equations (3.2) and (3.5). Then, regarding time-advancing for $q_{k,age}$, the remaining term $S_{k,age}$ of equation (3.11) is integrated. Since the age of the tagged moisture increases linearly with time, the numerical solution is given as

$$q^{n+1}_{k,age} = q^{n*}_{k,age} + q^{n+1}_{k,tag} \cdot \Delta T \tag{3.13}$$

where the time constant term p^* appearing in equation (3.11) is omitted in equation (3.13). ΔT (s) denotes the model time step length. The age-weighted tagged moisture components are initially set to zero.

The formation of tagged moisture begins with the evapotranspiration process at the land surface. Simultaneously, the formation of the atmospheric age-weighted tagged moisture is triggered and then tracked through all atmospheric processes until precipitating. The extended model then allows to calculate the atmospheric residence times τ_k of moisture by $q_{k,age}/q_{k,tag}$ and the atmospheric residence times T_P of precipitated water by P_{age}/P_{tag}. Additionally, the atmospheric residence times τ_k and T_P can also be calculated separately for transpired and direct evaporated tagged moisture and precipitated water.

Chapter 4

Experimental Design and Preparatory Simulations

In order to identify a suitable model setup for the following ET-Tagging study on the Poyang Lake region in Southeast China, preparatory simulations were performed. In this chapter, the design of the appropriate test simulations and the analysis strategy are presented. The validation allows to evaluate the performance of the basic MM5 model in simulating the general climatological variations. Firstly, spatial patterns of annual statistics and area-aggregated time series from the simulations are compared with those from gridded observations for the year of 2005. As a result, an suitable model setup for applying the extended model is chosen in order to study evapotranspiration- and precipitation-related processes like precipitation contribution ratios. Secondly, vertical profiles from the simulation with the chosen model setup are compared with those from station observations on a monthly scale for the same period under investigation. It allows to evaluate the chosen model setup in order to study celerity-related processes like atmospheric water residence times for this study region.

4.1 Basic Model Configurations

Firstly, the MM5 model (version 3.5) is applied with different domain sizes (i.e., large or small domain) and different grid spacings (i.e., 18 km, 09 km, 4.5 km) shown in Figures 4.1 and 4.2. Four model runs (see Table 4.1) are performed. For the vertical discretization, 33 model layers up to 50 hPa with refined layers in the lower part of the atmosphere are used.

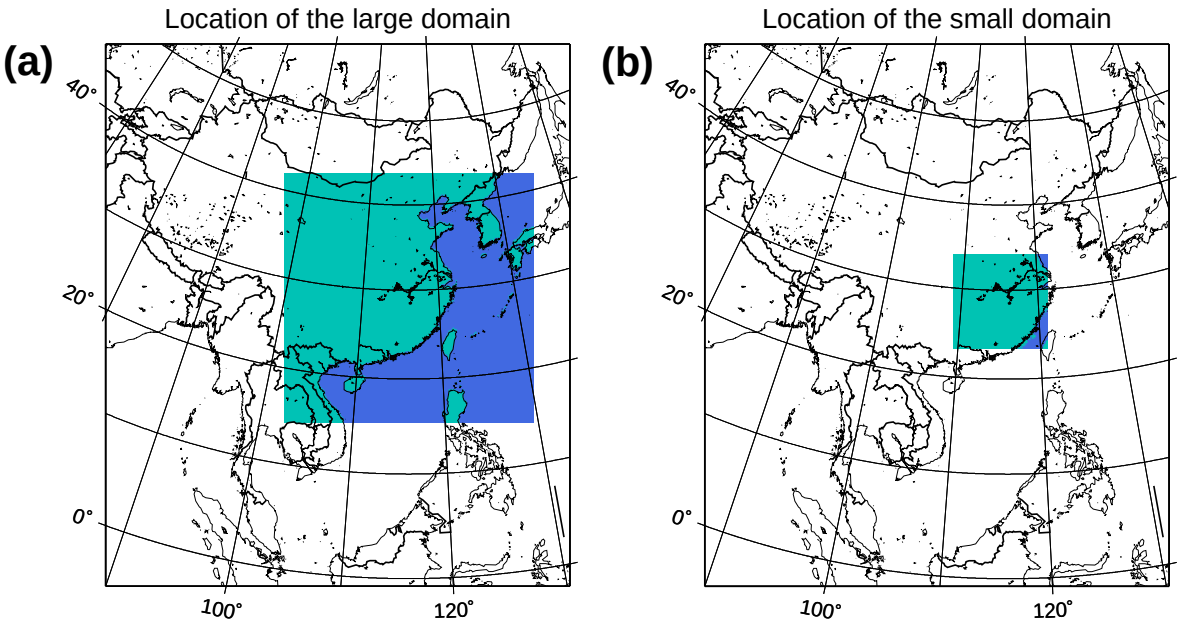

Figure 4.1: Location of the chosen model domains in this study (see also Table 4.1).

Table 4.1: Setup of the MM5 model for the preparatory simulations.

Different setup	*L*arge domain		*S*mall domain	
	L18	*L09*	*S09*	*S4.5*
Simulation domain	Northeast: 136.2°E 42.0°N		Northeast: 121.8°E 33.7°N	
	Southwest: 102.5°E 14.1°N		Southwest: 110.9°E 24.2°N	
Domain size (grid points)	180 × 180	360 × 360	120 × 120	240 × 240
Horizontal resolution (km)	*18*	*09*	*09*	*4.5*
Common setup				
Vertical discretization	33 levels			
σ levels	1.000, 0.996, 0.990, 0.983, 0.974, 0.963, 0.950, 0.934, 0.916, 0.896, 0.873, 0.848, 0.820, 0.789, 0.755, 0.718, 0.680, 0.640, 0.600, 0.560, 0.520, 0.480, 0.440, 0.400, 0.360, 0.320, 0.280, 0.240, 0.200, 0.160, 0.120, 0.080, 0.040, 0.000			
Boundary update	6 hours			
Output frequency	hourly			
Time period	3 months spin-up time (October-December 2004)			
	12 months evaluation time (January-December 2005)			

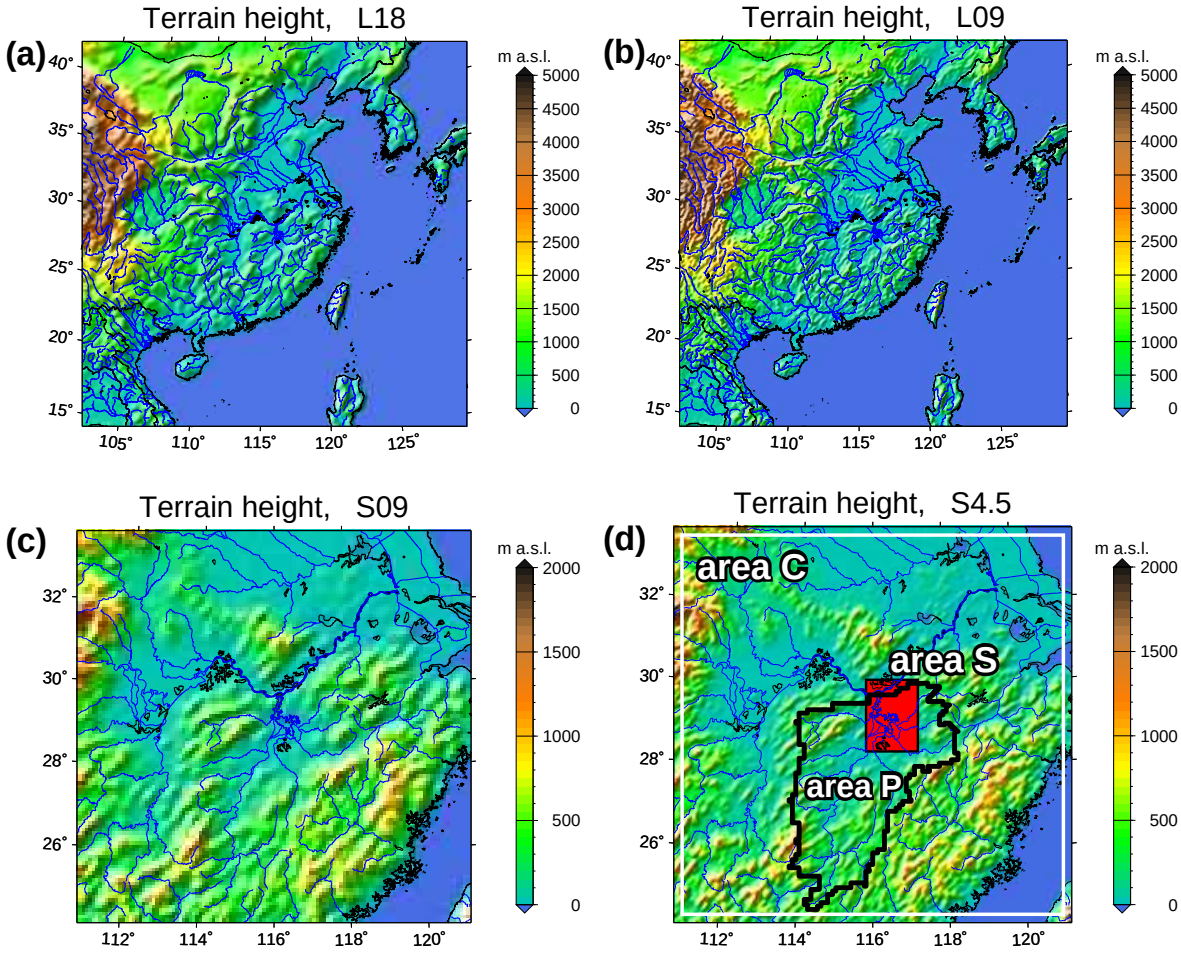

Figure 4.2: Terrain height (m a.s.l.) of the chosen model domains (see also Table 4.1). Rivers, lakes and the ocean are shown in blue. Additionally shown in (d) are three analysis areas where the simulated meteorological conditions are evaluated: The Poyang Lake region (area S, red shaded), the Poyang Lake basin (area P, black frame), and the model domain except a small boundary zone, nearly representing Southeast China (area C, large white rectangle).

Table 4.2: Physical schemes of the MM5 model as used in this study.

Compartment	Selected scheme	Reference
Shortwave radiation	Dudhia	Dudhia (1989)
Longwave radiation	RRTM	Mlawer et al. (1997)
Land surface	OSU-LSM	Chen and Dudhia (2001)
Planetary boundary layer	MRF-PBL	Hong and Pan (1996)
Microphysics	Mixed-Phase (Reisner 1)	Reisner et al. (1998)

The physical schemes selected for this study are summarized in Table 4.2. As mentioned by Knoche and Kunstmann (2013), it is difficult to achieve a process-based treatment for moisture tracking when cumulus parametrization schemes are employed.

Therefore, a comparatively high model resolution are chosen and it is assumed that the resolution is fine enough to resolve most of the relevant convective systems and do not apply an additional cumulus parametrization scheme. This choice is also taken in many other studies (Molinari and Dudek, 1992; Weisman et al., 1997; Done et al., 2004; Arakawa, 2004; Hong et al., 2008; Prein et al., 2013; Lee and Hong, 2015). The main reason is that at high resolution, the parametrizations are assumed to be obsolete because (deep) moist convection is (mostly) resolved at the grid scale.

The global reanalysis data ERA-Interim (with T255 spectral resolution $\approx 80\,\text{km}$, (Dee et al., 2011)) from the European Centre for Medium-Range Weather Forecasts (ECMWF) provides the initial and lateral boundary conditions (atmospheric meteorological fields and SSTs). Geographical data describing terrain height, vegetation/land-use (24 category U.S. Geological Survey (USGS) data), and soil characteristics (17 category FAO data) are taken from NCAR data sets. The hindcast simulation period covers 15 months from October 2004 to December 2005. The first three months are considered as model spin-up time, allowing the soil moisture and the atmospheric moisture components to sufficiently develop.

4.2 Evaluation Data and Strategy

Reference Data As reference data sets for precipitation, evapotranspiration, temperature, and wind fields, APHRODITE_V1003R1 (Asian Precipitation Highly Resolved Observational Data Integration Towards Evaluation of Water Resources, (Yatagai et al., 2009, 2012)), FLUXNET MTE (Model Tree Ensembles, (Jung et al., 2009, 2010, 2011)), CRUTEMP 3.0 (Climatic Research Unit, (Brohan et al., 2006)), and IGRA (the Integrated Global Radiosonde Archive, (Durre et al., 2006, 2008)) are used.

The APHRODITE product provides long-term daily gridded precipitation data over Asia at $0.25^\circ \times 0.25^\circ$ resolution. It merges 2.3 to 4.5 times more rain-gauge data compared to the data available through the Global Telecommunication System network (Yatagai et al., 2009) and is assumed to better represent precipitation in complex terrain (Yatagai et al., 2012).

The FLUXNET MTE product provides monthly gridded global evapotranspiration data at $0.5^\circ \times 0.5^\circ$ spatial resolution. It is derived by empirical upscaling of eddy covariance measurements from a global network of flux towers (FLUXNET) with a model tree ensemble (MTE) approach (Jung et al., 2009).

The CRUTEMP 3.0 product covers the whole globe, too, and has the same temporal (monthly) and spatial (at $0.5^\circ \times 0.5^\circ$) resolution as FLUXNET MTE. It is widely used

for validation of simulated near surface temperature (Fersch and Kunstmann, 2013) and for studying climate changes (Qian et al., 2011).

The IGRA database provides long-term daily radiosonde observations (e.g., wind speed and wind direction data) from more than 1500 stations globally (Durre et al., 2006). It is the largest and most comprehensive collection of quality-assured soundings and readily available (Durre et al., 2008).

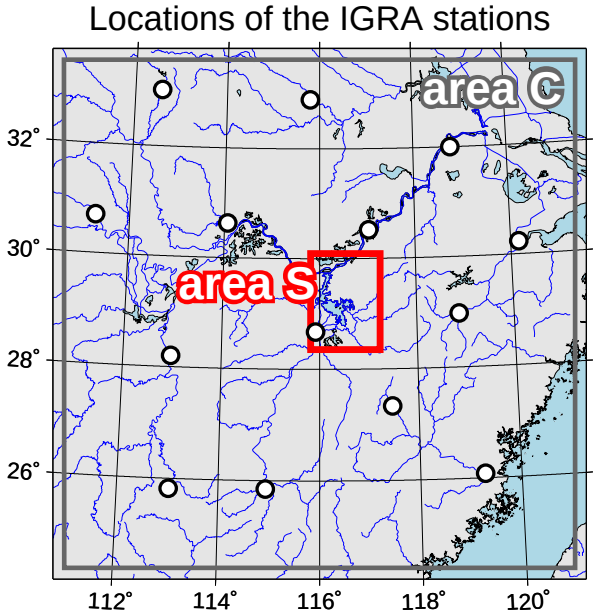

Figure 4.3: Locations of the IGRA stations in this study. Rivers, lakes, and the ocean are shown in blue. The continent is shown in gray. The tagging source area (area S) lies within the red rectangle. The large gray rectangle (area C) nearly represent Southeast China. The individual circles represent IGRA radiosonde stations used for wind validation of the simulation.

Model Evaluation For comparisons with gridded observations, the simulated precipitation, evapotranspiration, temperature were remapped to the respective reference data grids using a bilinear interpolation. For comparisons with station observations, the simulated wind components (zonal u and meridional v velocity) are averaged over nine grid points surrounding each IGRA station (shown in Figure 4.3) for each model layer. The investigations are concentrated on three analysis areas (see Figure 4.2d): the model domain except a small boundary zone (area C, covering nearly all of Southeast China), the Poyang Lake basin (area P), and the Poyang Lake region (area S).

4.3 Validation of Meteorological Modeling

To evaluate the performance of the basic MM5 model, spatial patterns of annual statistics and analysis-area aggregated time series from the four simulations, i.e., L18, L09, S09, and S4.5, (see Table 4.1) is compared with gridded observations for the year of 2005. As a consequence, a suitable model setup needed to be identified for the application of the extended model for studying precipitation contribution ratios. Furthermore, vertical profiles of wind components simulated by the MM5 with the chosen setup are compared with station observations, averaged for 14 radiosonde stations (see Figure 4.3) for each month in 2005. This comparison allows to evaluate the chosen model setup for studying atmospheric water residence times.

4.3.1 Model versus Gridded Observations

Precipitation Figures 4.4 and 4.5 depict the total annual precipitation for 2005 from APHRODITE and the MM5 model simulations (a, c, e, g), respectively. The relative differences between simulations and observation are shown in Figures 4.5 (b, d, f, h).

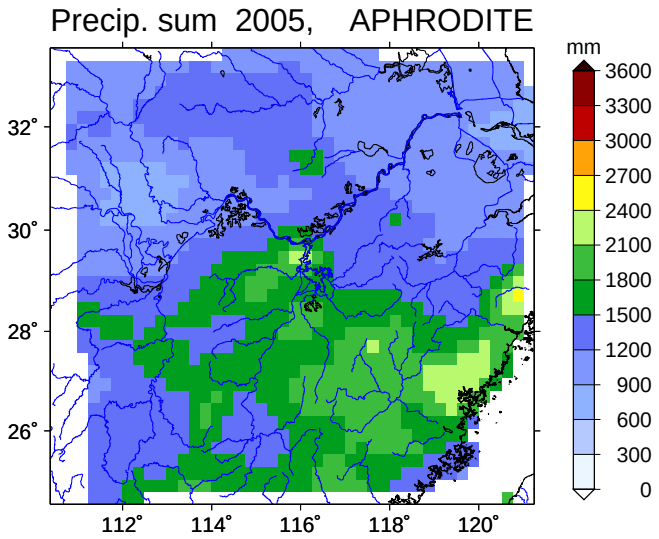

Figure 4.4: Annual total precipitation (mm) for Southeast China for 2005 from APHRODITE reference data.

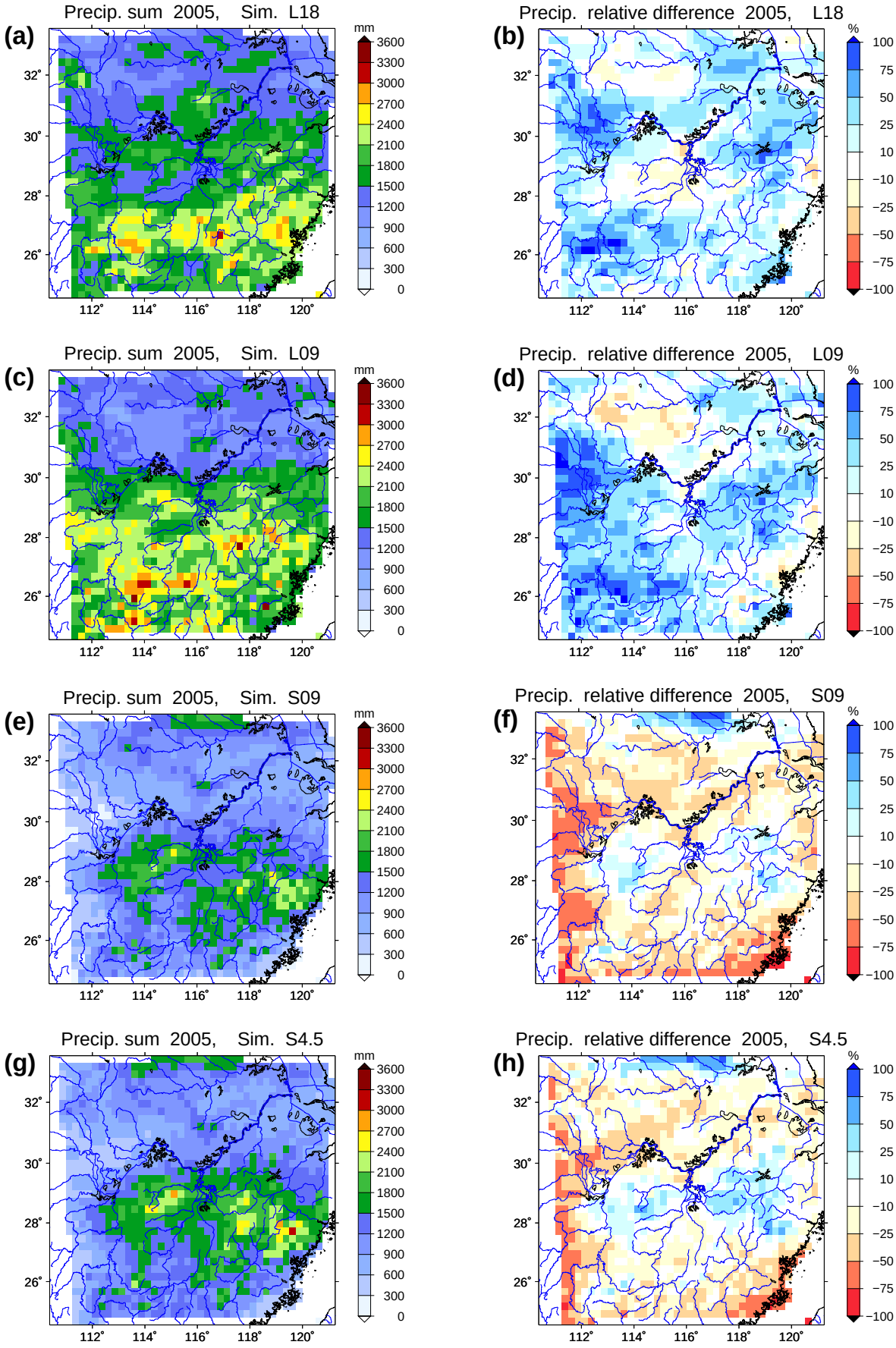

Figure 4.5: Annual total precipitation (mm) for Southeast China for 2005 from the four simulations (the left column). The relative differences (%) between simulation and reference data (see Figure 4.4) are shown in the right column.

Various smaller scale structures are found in the simulation data, presumably due to the finer horizontal resolution of the original model output data. Generally, the MM5 model can reasonably reproduce the overall pattern of the reference data: the amount of the annual precipitation decreases from the South to the North. However, the models with the setup of a large domain (i.e., L18 and L09) significantly overestimate the total precipitation amount (Table 4.3), especially for the southern part of the analysis area C. A pronounced wet bias ($\geq 50\,\%$) is found for the regions outside the Poyang Lake region (Figures 4.5b and 4.5d). This overestimation becomes larger with the change of the horizontal model resolution from 18 km to 9 km (Table 4.3 and Figure 4.5d). In contrast, the patterns of simulated precipitation by S09 and S4.5 are much closer to APHRODITE (Figures 4.5e and 4.5g). The simulations tend to underestimate the total amount of precipitation (Table 4.3), especially along the southeastern coast line and near the western boundary. It is partly ascribed to the excepted effect of degrading the resolution of lateral boundary conditions over the small domain (Denis et al., 2003). There is no enough time to allow the development and formation of the precipitation over such small domain. In comparison to the deviation map of S09 (Figure 4.5f), S4.5 appears less dryer near the boundary and slightly wetter in the center (shown in Figure 4.5h).

Figure 4.6 shows the annual cycle of precipitation aggregated over the three analysis areas (see Figure 4.2d) for the year 2005. The model results show comparatively good agreement with the reference data. The differences between simulated and observed precipitation during the rainy season (i.e., from April to June) show large variations. For the large domain setups, overestimation mainly occurs during the months before July in 2005, especially in May, while underestimation exists during the remaining months. The model with the small domain setups produces slightly too little rainfall, with the exception of May, where the simulated precipitation considerably exceeds the observations in areas P and S.

Evapotranspiration Figures 4.7 and 4.8 show the total annual evapotranspiration for the period under investigation from FLUXNET MTE and the simulations (a, c, e, g). The relative differences between simulations and observation are given in Figures 4.8 (b, d, f, h).

Generally, the relative differences of simulated evapotranspiration are smaller than that of simulated precipitation. In L18 and L09 (Figures 4.8b and 4.8d), small positive deviations are found for the northern part and northwest quadrant of area C, while small negative deviations are located in the South. In S09 and S4.5 (Figures 4.8f and 4.8h), the annual deviation patterns are different with larger deviations near the domain boundary than in the center. It is worth to note that the relative differences are small except in the regions in the northeast quadrant, where the land-use type is inland

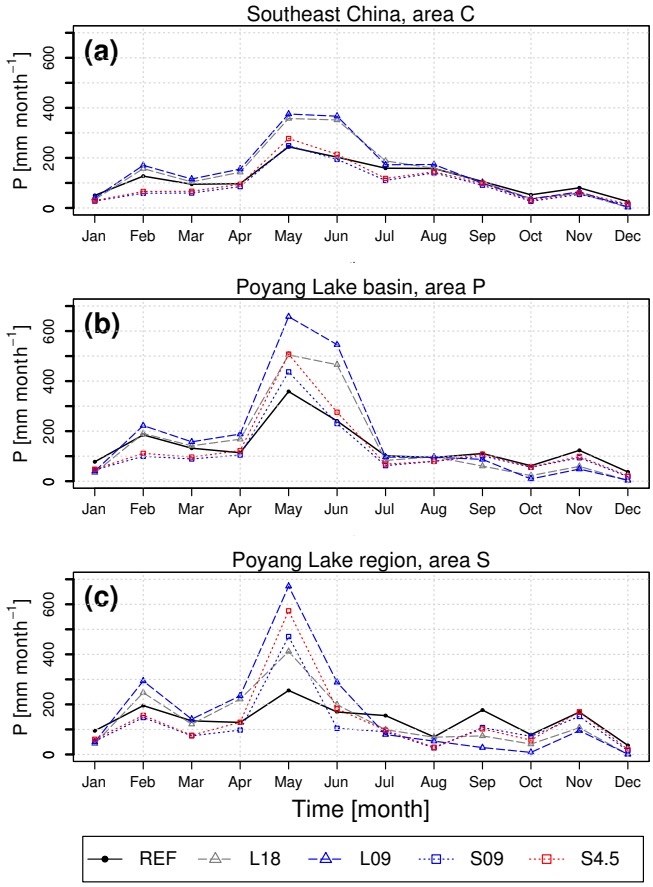

Figure 4.6: Comparison of simulation results of L18, L09, S09, and S4.5 (gray, blue, and red lines) and APHRODITE reference data REF (black line): Shown are area-averaged, monthly time series of precipitation (mm month^{-1}) for the three analysis areas C, P, and S (see Figure 4.2d).

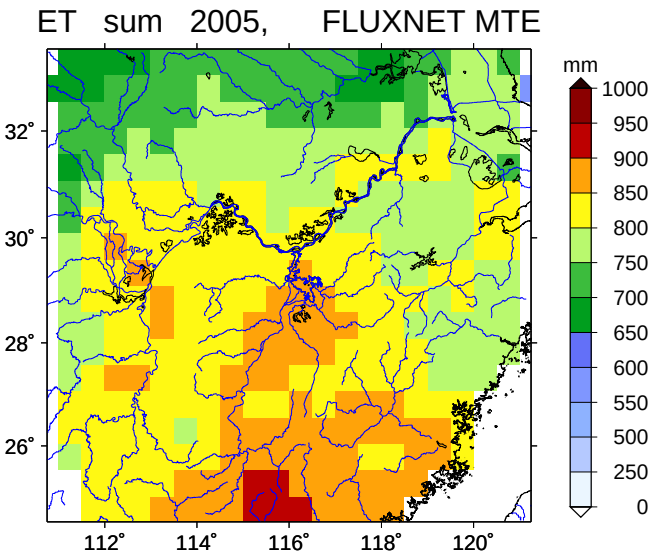

Figure 4.7: Annual total evapotranspiration (mm) for Southeast China for 2005 from FLUXNET MTE reference data.

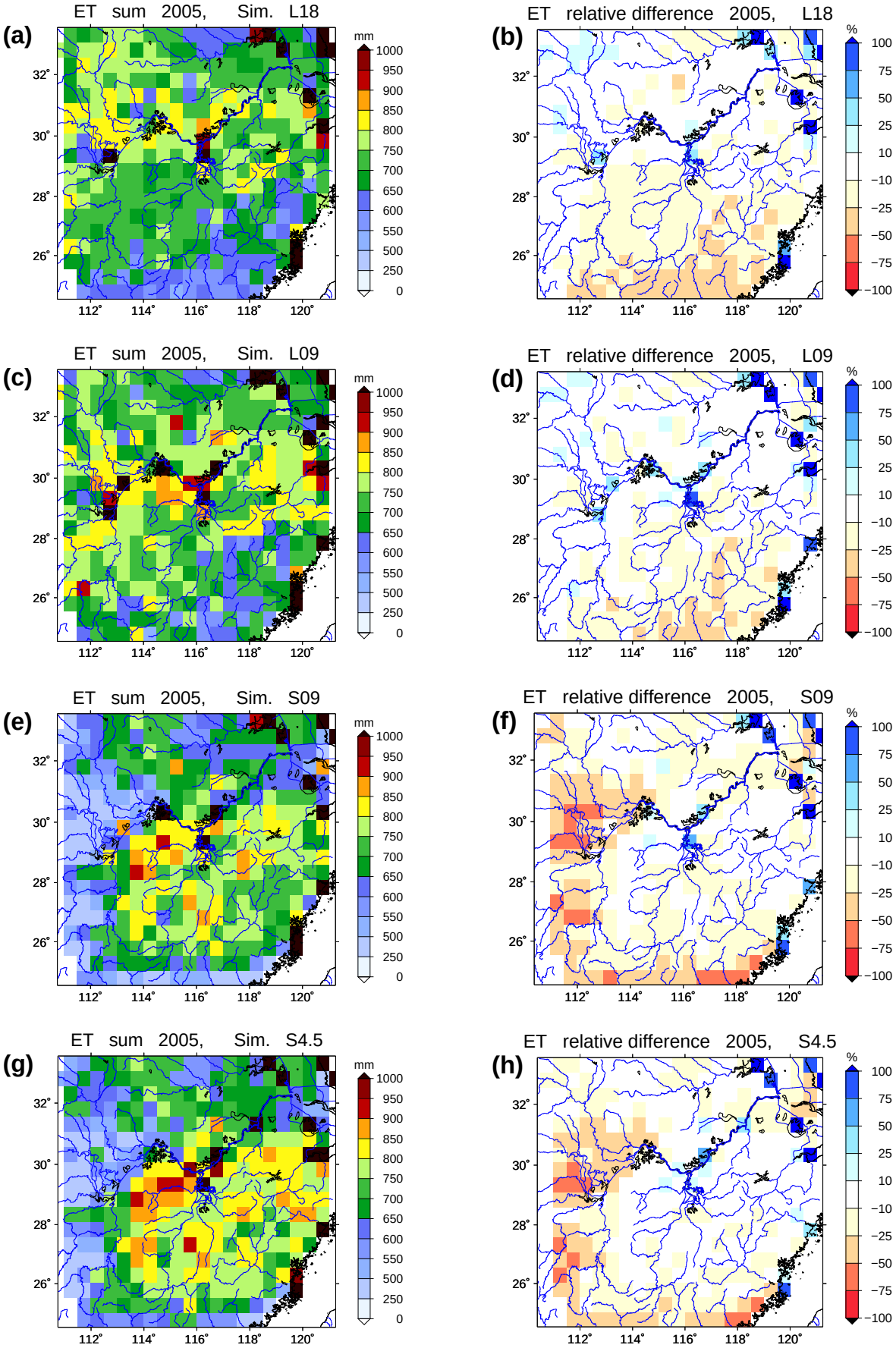

Figure 4.8: Annual total evapotranspiration (mm) for Southeast China for 2005 from the four simulations L18, L09, S09, and S4.5 (the left column). The relative differences (%) between simulation and reference data (see Figure 4.7) are shown in the right column.

water bodies. These deviations are partly attributed to the reference data: due to the weakness of the eddy covariance method used for FLUXNET MTE and the limited spatial representation (see Figure 2 in Jung et al. (2009)), the evapotranspiration near distinct landscape transitions such as lakes is not well captured (Baldocchi et al., 2001). However, FLUXNET MTE is still the only territorial-based evapotranspiration data set on a long-term and continuous base. On the other hand, the MM5 model used in this study does not account for the impact of human activities, like for the irrigation of paddy rice. But Wei et al. (2012b) found that irrigation-induced evapotranspiration caused only a small increase in precipitation, even in heavily irrigated central and northern China.

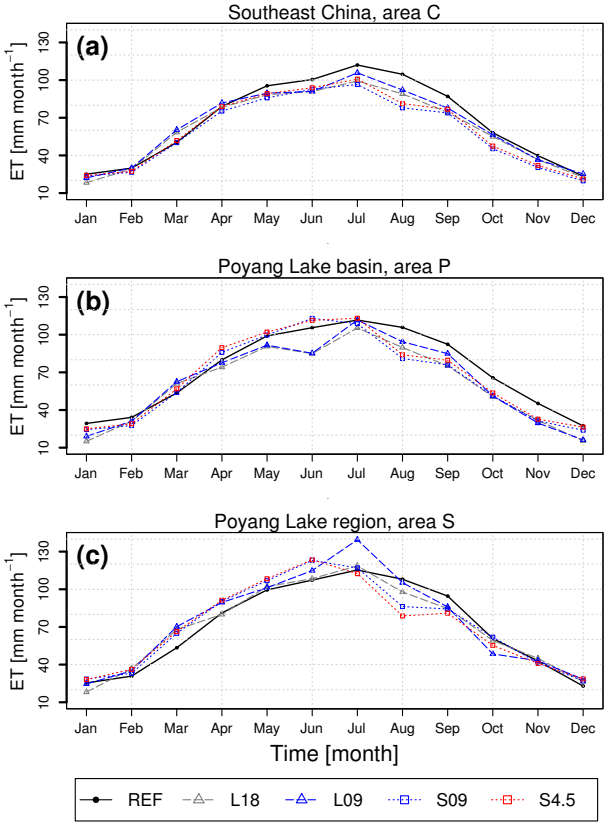

Figure 4.9: Comparison of simulation results of L18, L09, S09, and S4.5 (gray, blue, and red lines) and FLUXNET MTE reference data REF (black line): Shown are area-averaged, monthly time series of evapotranspiration (mm month^{-1}) for the three analysis areas C, P, and S (see Figure 4.2d).

The annual cycle of the simulated evapotranspiration aggregated over the three analysis areas is also in good agreement with the reference data (Figure 4.9). For area C, the values of the simulated evapotranspiration are smaller than the reference data during the whole year except March and April (Figure 4.9a). For the Poyang Lake basin (area P) (Figure 4.9b), the deviations of the large domain simulations are larger than that of the small domain simulations in the warm season (i.e., from April

to September). Over the source area S, significantly too small values are found only in summer, especially in August (Figure 4.9c). The reasons may be the slight underestimation of precipitation in this month and the neglection of irrigation schemes in this model. Pronounced large overestimation of evapotranspiration by L09 in July (see Figure 4.9c) are probably due to the interplay between overestimation of precipitation and higher air temperature in the previous month (June).

Temperature Figures 4.10 and 4.11 show the spatial distribution of simulated temperature (a, c, e, g) and the deviation pattern (b, d, f, h) with respect to the CRUT data.

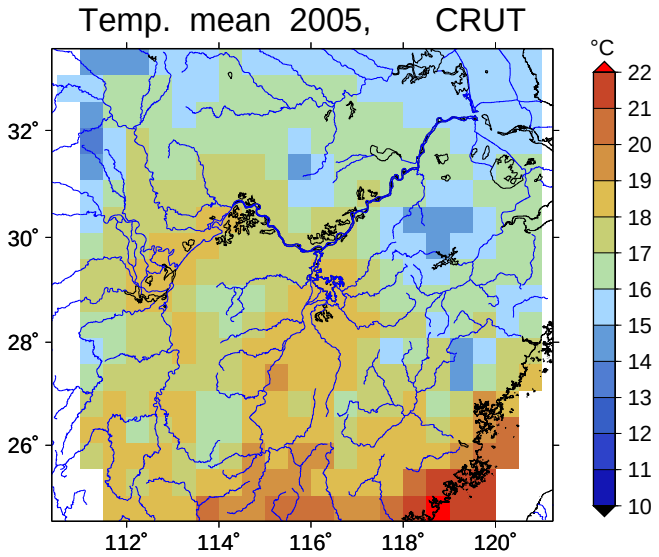

Figure 4.10: Annual mean temperature (℃) for Southeast China for 2005 from CRUT reference data.

The bias of the temperature in Figure 4.11 is closely connected to the bias of the precipitation in Figure 4.5. A significant cold bias occurs for the two large domain model runs (Figures 4.11b and4.11d), mainly in the North. On the contrary, a warm bias over the southern part of the area C is seen in Figures 4.11f and 4.11h for the two simulations with the small domain setups.

On a monthly scale, the deviations between simulations and observation are smaller (≤ 1℃) during the transient seasons and larger (≥ 2℃) in the hot July and the cold December (Figure 4.12). For L18 and L09, a significantly cold bias mainly occurs in July and in November and December, likely due to underestimated shortwave radiation (Zhang et al., 2011b). Whereas for S09 and S4.5, the simulated 2-meter temperatures agree well with reference data in October and November, but are approximately 2℃ lower in December when MM5 might overestimate cloud coverage. From May to

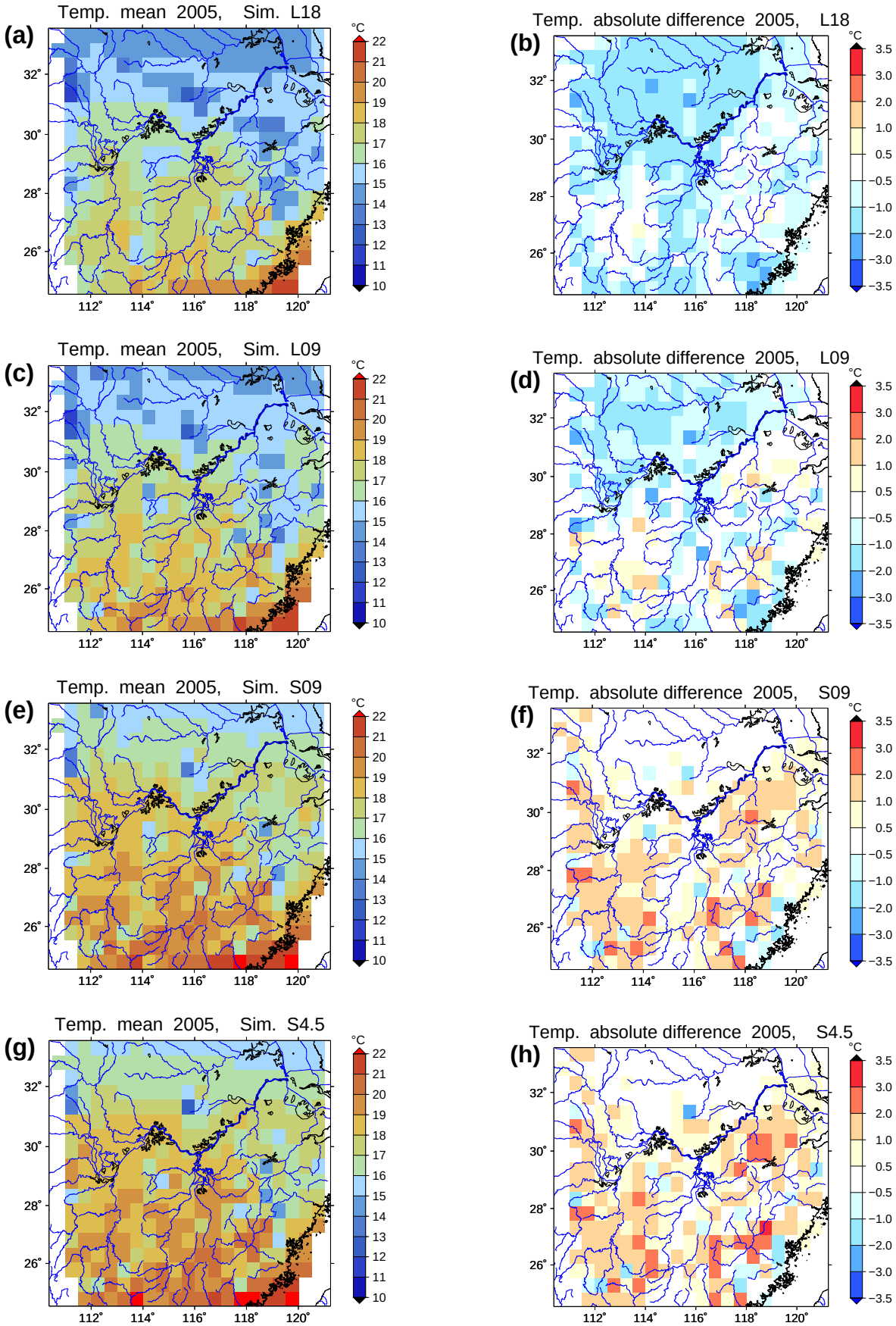

Figure 4.11: Annual mean temperature (℃) for Southeast China for 2005 from the four simulations L18, L09, S09, and S4.5 (the left column). The absolute differences (%) between simulation and reference data are shown in the right column.

September a pronouncedly warm bias persists.

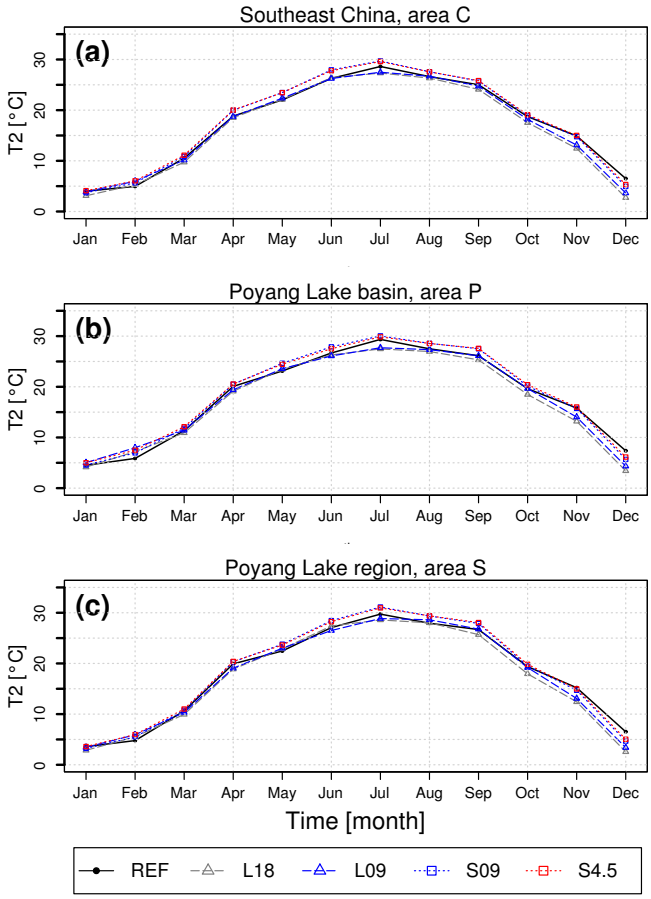

Figure 4.12: Comparison of simulation results of L18, L09, S09, and S4.5 (gray, blue, and red lines) and CRUT reference data REF (black line): Shown are area-averaged, monthly time series of temperature (°C) for the three analysis areas C, P, and S (see Figure 4.2d).

Identification of Suitable Model Setup As a summary, Table 4.3 shows the corresponding bias and RMSE values of the simulated variables with respect to the reference data. The mean bias of the precipitation for the simulation S4.5 holds the smallest value for the three analysis areas. Larger values of RMSE for S4.5 are found with the analysis area being smaller. For simulating evapotranspiration, S4.5 is also capable to conduct the simulation with little bias and RMSE. Only the RMSE value for area S is slightly larger probably due to the above-discussed restriction of the reference data. Regarding temperature, there is no significant improvement of simulation by changing the model domain size and the model horizontal grid spacing.

From the results (Table 4.3), it turns out that a model domain covering Southeast

China (see Figure 4.2d) with a horizontal resolution of 4.5 km and 240 × 240 grid cells (i.e., S4.5) is the best one. Many studies (Jones et al., 1995; Seth and Giorgi, 1998; Leduc and Laprise, 2009) suggest that the domain size should be large enough to allow the full development of small-scale features. However, Seth and Rojas (2003) and Gonzalo et al. (2004) noted that large deviations between simulations and observations are obtained when large scale nudging is not applied. Similarly, the simulation results on the large domain (L18 and L09) without applying large scale nudging show significantly deviations from the reference data as well. In contrast, in the simulations on the smaller domain (S09 and S4.5) the small-scale patterns are well represented. Therefore, the small domain size is appropriate for this study.

Regarding the horizontal resolution, Weisman et al. (1997) states that approximately 4 km is usually sufficient to reproduce mesoscale systems, which is also supported by the arguments given in Chapter 4.1. For this subtropical, mountainous study region (Southeast China), a model resolution of 4.5 km is chosen. This resolution is assumed to be fine enough to capture the convective systems sufficiently by grid-scale resolved dynamic model processes. Overall, the simulated evapotranspiration, precipitation, and temperature are reasonably reproduced in the simulation S4.5, and it is concluded that the model setup S4.5 allows to study evapotranspiration- and precipitation- related processes like precipitation contribution ratios. Here the results for the (total) moisture quantities were examined, but this indicates that this model setup also allows reasonable estimates of the tagged moisture quantities.

Table 4.3: Mean bias and RMSE for P (mm month^{-1}), ET (mm month^{-1}), and T2 (℃) of the four model runs (see Table 4.1) for three analysis areas (see Figure 4.2d) for the year of 2005.

	P			ET			T2		
area	C	P	S	C	P	S	C	P	S
Bias									
L18	24.8	16.0	-2.7	-5.4	-10.4	0.2	-0.9	-0.9	-0.9
L09	31.3	43.0	23.2	-3.0	-7.9	3.7	-0.5	-0.4	-0.5
S09	-24.0	-18.4	-21.1	-8.9	-6.1	1.9	0.5	0.6	0.5
S4.5	-15.1	-3.5	-1.0	-6.7	-3.8	0.7	0.7	0.7	0.6
RMSE									
L18	58.0	84.9	70.6	8.4	12.7	6.7	1.5	1.6	1.6
L09	65.4	129.6	144.6	6.7	10.9	10.3	1.1	1.3	1.2
S09	30.4	40.5	76.9	11.4	11.0	9.7	1.0	1.0	1.1
S4.5	27.5	52.7	99.6	9.3	9.7	12.1	1.0	1.0	1.0

4.3.2 Model versus Station Observations for the Final Model Setup

Wind For applying the age-weighted ET-Tagging approach to calculate the atmospheric water residence times, further performance evaluation of the MM5 model in simulating wind fields is presented. Following the result shown above, the focus here is on the simulation S4.5. Figure 4.13 shows the vertical profiles of wind components from MM5 and IGRA (see Section 4.2), averaged for 14 radiosonde stations (see Figure 4.3) by month for the year 2005. The variations of simulated wind speed and direction with height and season show comparatively good agreement with the data derived from the station observation. For the zonal wind component, a difference between simulated and observed winds is small from January to May, tends to larger (underestimation) in the following four warm months, and becomes small again for the remaining time (Figure 4.13a). Due to the onset and retreat of the East Asian summer monsoon, changes in the direction of the meridional wind component are observed in the lower part of the atmosphere (below 800 hPa) from IGRA (Figure 4.13b). These changes are also well captured by the model, with an overestimation of around 0.5 m s^{-1} in summer. Overall, the simulated winds are reasonably reproduced here and, it is concluded that the model setup S4.5 allows to study celerity-related processes like atmospheric water residence times for this study region.

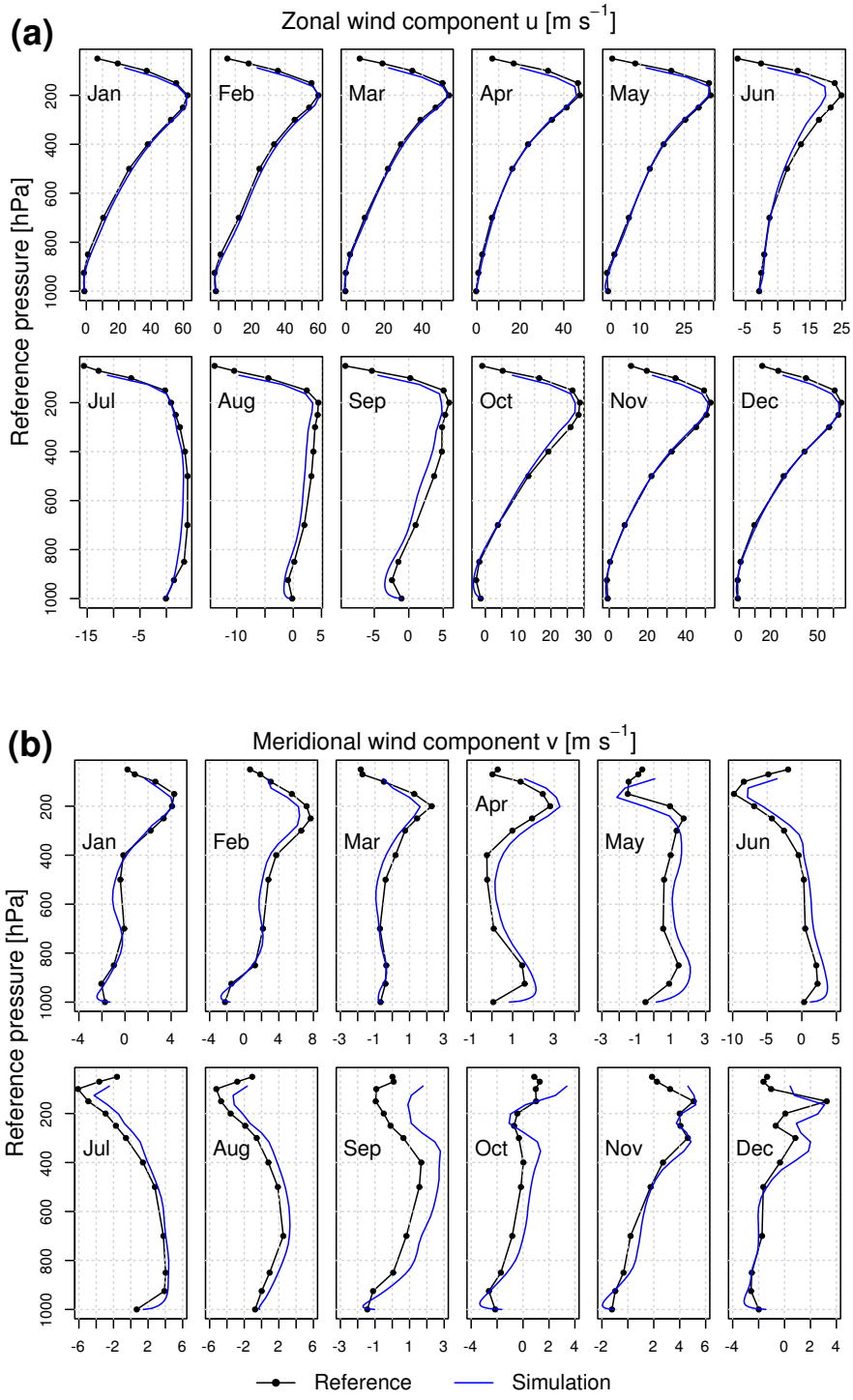

Figure 4.13: Comparison of simulation (blue line) and reference (black line) data for vertical profile of wind components: (a) zonal velocity u (m s^{-1}) and (b) meridional velocity v (m s^{-1}). The observational wind components from IGRA reference data are averaged for 14 radiosonde stations (shown in Figure 4.3b) for each month in 2005. Our simulated wind components are accordingly averaged over nine grid points surrounding each station for each model layer and for the same period under investigation.

Chapter 5

Fate of Evapotranspired Water

It is a challenge to quantitatively answer "where does the evapotranspired water from the Poyang Lake region go?". In the past, land-atmosphere interactions in the Poyang Lake region and their possible influence over Southeast China were inferred from previous research using analytical methods on global scales (Trenberth and Guillemot, 1995; Trenberth, 1998, 1999b) or for the whole of China (Simmonds et al., 1999; Zhou and Yu, 2005).

Previous studies have stated that more than 40% of precipitation in China is of continental origin (Bosilovich and Schubert, 2002; Yoshimura et al., 2004b; van der Ent et al., 2010; Goessling and Reick, 2011, 2013; van der Ent et al., 2014). Using the Water Accounting Model, van der Ent et al. (2010) found that 80% of China's water resources depends on terrestrial evaporation from the Eurasian continent. Oceanic evaporationsheds (sources) for precipitation in China covers the Atlantic Ocean westward of Europe, the Bay of Bengal, and the South China sea (van der Ent and Savenije, 2013). Additionally, Wei et al. (2012a) investigated the water vapor sources for the Yangtze River Valley rainfall with QIBT, using MERRA reanalysis data (Rienecker et al., 2011). It is shown that the major moisture source for the Yangtze River Valley is temporally varying between the Bay of Bengal, the South China Sea, and the western Pacific. In this region, however, consideration of dynamical and hydrological processes are still required for investigating the fate of evapotranspired water.

In this chapter, the ET-Tagging algorithm (Knoche and Kunstmann, 2013) is applied for the first time to the mountainous, subtropical monsoon region of Southeast China. The evapotranspiration study focuses on the Poyang Lake (29 °N, 116 °E) area, which is located in the center of Southeast China (see Figure 4.2d). 15-month simulations (RunTag$\boldsymbol{ET}$) from October 2004 to December 2005 are performed to investigate where and to what extent the tagged evapotranspired water returns to the land surface

as precipitation. Under the conditions of the complex mountainous terrain and the monsoon system in Southeast China, the detailed atmospheric online model for moisture tracking allows to spatially and temporally quantify the contribution of the water evapotranspired from the Poyang Lake region to local precipitation or to precipitation in the Poyang Lake basin or in Southeast China.

After a short description of the ET-Tagging application, a demonstration of this explicit moisture tagging approach is presented. Then, the distribution of tagged moisture and tagged precipitation is shown and an analysis of the atmospheric tagged water budget is presented.

5.1 Application of the ET-Tagging Algorithm

Specification of Source Area As the geographic source of tagged water in this study an area of about 25,000 km^2 covering the Poyang Lake and its surrounding wetlands was defined. This source area (referred to as area S) is identical with the red shaded smallest analysis area in Figure 4.2d. Figure 5.1 depicts the vegetation cover and land-use types for area S, based on the global 25-category data from the U.S. Geological Survey (USGS). The area of the Poyang Lake (land-use type 16) accounts for 13.5 % of the total source area (Figure 5.1b). Irrigated crop (i.e., paddy rice) around the lake is the prime vegetation type with a fraction of 47.6 % (land-use type 3). In comparison with the source areas defined in other tagging studies (Sodemann et al., 2009; Wei et al., 2012a; Winschall et al., 2014), the source area in this study, i.e. the Poyang Lake region, is relatively small.

Setup of the Extended Model Preparatory model runs with altered domain size and grid spacing were performed for the identification of a suitable model setup. The results of the comprehensive evaluation (shown in Chapter 4) are an indication that the extended model can also allow reasonable results for the tagged quantities. Consequently, the model configuration S4.5 (see Table 4.1) was chosen. The physical schemes applied for ET-Tagging simulations are the same as in Table 4.2. As already mentioned in Chapter 4.1, with cumulus parametrization schemes, it is difficult to achieve a process-based treatment for moisture modeling. Therefore, no cumulus parametrization is employed. Weisman et al. (1997) states that approximately 4 km is usually sufficient to reproduce mesoscale systems. The model resolution of 4.5 km chosen here is assumed to be fine enough to sufficiently capture the convective systems by grid-scale resolved dynamic model processes.

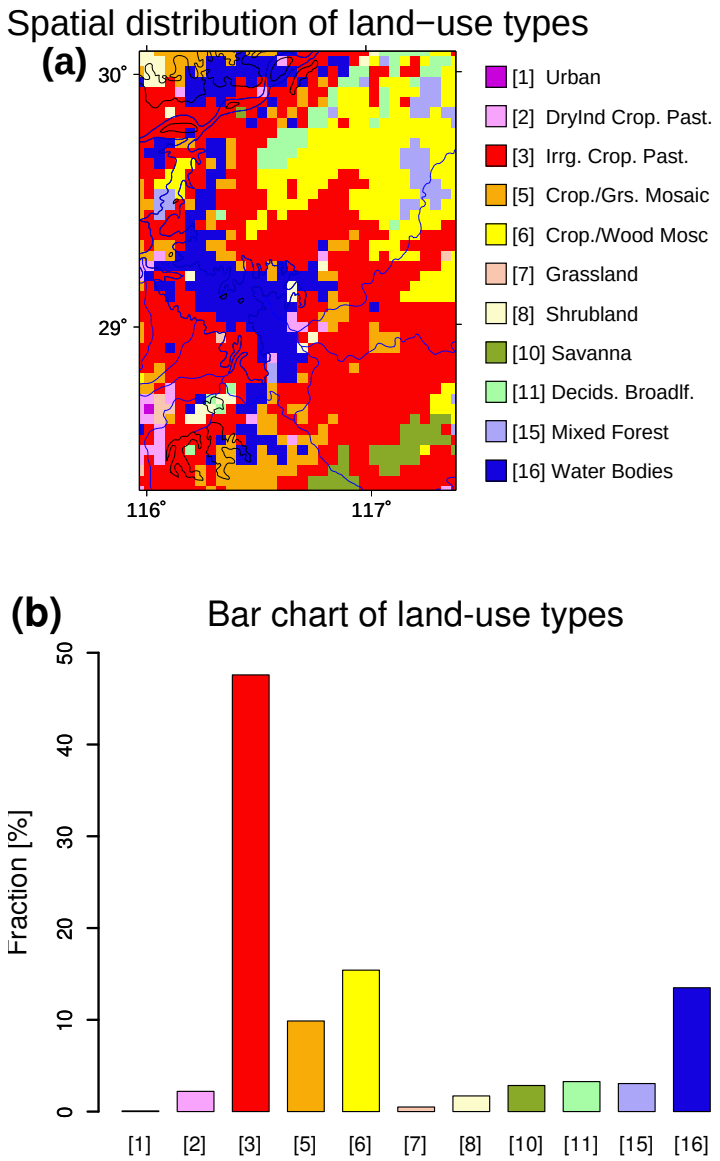

Figure 5.1: (a) Spatial distribution and (b) bar chart of the land-use types for area S (horizontal resolution 4.5 km). The results are based on the global 25-category data from the U.S. Geological Survey (USGS).

The driving data (ERA-Interim) and geographical data (USGS and FAO) are identical with those of the preparatory simulations (see Chapter 4.1). More details of the model configuration are given in Table 4.1. As the particular interest is in elaborating the impact of the advance and retreat of the East Asian monsoon on the land-atmosphere interaction for the Poyang Lake region, the analysis is performed for the period of one entire year (15-month simulations from October 2004 to December 2005, including 3-month spin-up period). The first three months (October-December 2004) are considered as model spin-up time in order to allow the tagged atmospheric moisture components to sufficiently develop. Regarding the spin-up time in this study, there are

two considerations: for atmospheric fields, the spin-up time is rather short (i.e., 1-2 days) (de Ela et al., 2002). Hence, 2 weeks of simulation are generally enough to develop the tagged atmospheric moisture components (Bosilovich and Schubert, 2002). In contrast, for some land-surface processes (e.g., deep soil hydrology), the spin-up time is considerably longer (Laprise, 2008): The long-term land-surface interaction studies require several months of simulation to develop a consistent state of the soil moisture, for example, (up to 1 year in Goessling and Reick (2013)). In a previous work (Knoche and Kunstmann, 2013), 1 month is taken as a spin-up period for a rainy month of investigation. Thus, this choice of a three-month spin-up time is a good compromise and assumed to be sufficient for this investigation.

Initially, there is no tagged water substance existing in the atmosphere. After the start of ET-Tagging simulation, a tagged water substance can leave the atmosphere through outflow at the lateral boundaries of the model domain. Returning tagged water from outside of the model domain is not taken into account.

Parallelism of the Extended Model Additionally, four further experimental ET-Tagging runs was conducted to evaluate the benefit from parallelism. The same model domain size and the same model physical scheme were taken as these of S4.5, but with a horizontal resolution of 9 km instand of 4.5 km in order to save CPU-hours. Significant performance gain is achieved by using the parallelized ET-Tagging model. More results of the parallelized ET-Tagging simulations are given in Appendix A. All the following simulations are conducted in the parallel computing mode.

5.2 Analysis Methods

To quantify the contribution of evapotranspiration to precipitation, a local precipitation contribution ratio ρ is defined as:

$$\rho = P_{tag}/P_{total} \tag{5.1}$$

P_{tag} denotes the tagged precipitation contribution of ET from a predefined source area, while P_{total} denotes the total precipitation originating from local ET or remote moisture sources.

To explore the relation between evapotranspiration from the source area and tagged precipitation in different geographic surrounding areas, an atmospheric tagged water budget analysis on monthly scales is performed. For this, the budget equation for the

tagged moisture can be formulated as

$$ET_{tag,S} = P_{tag,S} + P_{tag,PoS} + P_{tag,CoPS} + \Delta Q_{tag,C} + F_{tag,C} \tag{5.2}$$

where $ET_{tag,S}$ denotes the tagged evapotranspiration in the source area S. $P_{tag,S}$, $P_{tag,PoS}$, and $P_{tag,CoPS}$ denote the tagged precipitation in area S, in area P but outside of S, and in area C but outside of P and S, respectively. $\Delta Q_{tag,C}$ is the storage change of the tagged moisture over area C and $F_{tag,C}$ is the net lateral outflow flux of tagged moisture. $ET_{tag,S}$ and the tagged precipitation terms can be obtained directly from the ET-Tagging simulation. $\Delta Q_{tag,C}$ is calculated using the difference of the column-integrated total tagged moisture between the beginning and the end of the considered period, and $F_{tag,C}$ is determined as the residual in equation (5.2).

5.3 Results and Discussion

5.3.1 Illustration of Dynamical Evolution

To illustrate the dynamical evolution of the moisture evapotranspired from the tagging area S (here, the Poyang Lake region), transport and spreading of tagged moisture in the atmosphere is displayed during the first simulated 40 hours of RunTagET in October 2004. The day-night variations due to differences of evapotranspiration and the variations of the atmospheric conditions are depicted in Figures 5.2 and 5.3.

The 6-hourly time sequence in Figure 5.2 shows the horizontal distributions of the column-integrated total tagged moisture (consisting of water vapor, cloud water, cloud ice, rain water, and snow) over the area C. At the start of the simulation (08:00 China Stand Time CST 1 October 2004), tagged moisture is set to zero (Figure 5.2a). After that, evapotranspirating water from the source area S is tagged when entering the atmosphere. Then, the tagged moisture undergoes the same atmospheric processes (i.e., transport and phase transitions) as the (original) total moisture. The wind fields primarily dominate the dynamical evolution of the tagged moisture. The comparison between Figure 5.2b and Figure 5.2c demonstrates the transport and spreading of the total tagged moisture controlled by the wind fields after 6 hours. Finally, the tagged moisture can leave the model domain (see Figures 5.2c and 5.2d) or return to the land surface as precipitation (shown in section 5.3.3). The day-night differences of evapotranspiration, which is closely connected to the changes in temperature, also impact the variations of the tagged moisture pattern. Figure 5.2e shows that little tagged moisture is found in the atmosphere over the source area S due to the limited water evapotranspired in the cold early-morning. With the incoming radiation and tempera-

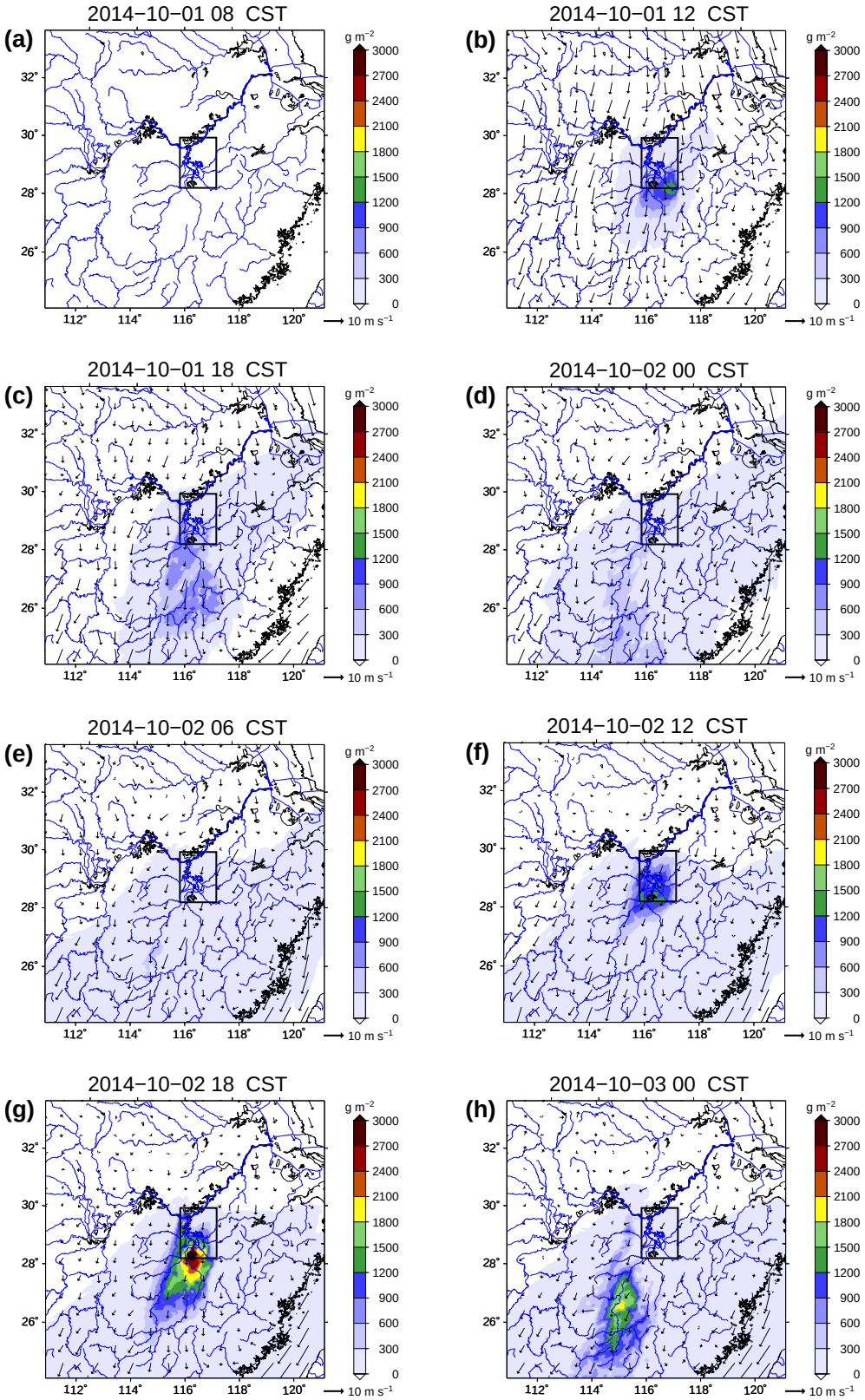

Figure 5.2: Horizontal distribution of column-integrated total tagged moisture (g m^{-2}) at different times during the first 40 hours (08:00 CST 01 October to 00:00 CST 03 October 2004). The arrows indicate the hourly mean of horizontal wind (m s^{-1}) at 10 meters.

ture increasing in the second day (i.e., 02 October), the tagged moisture increases and undergoes the transport and spreading processes again (Figures 5.2f-h).

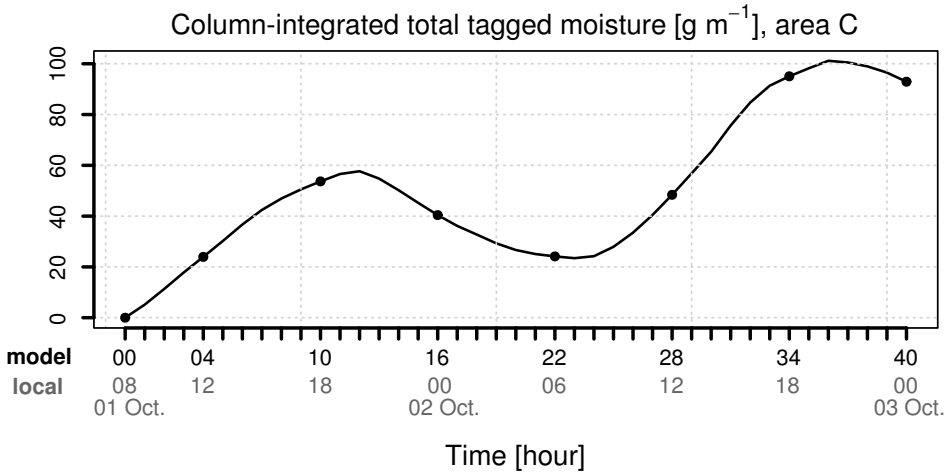

Figure 5.3: Time series of hourly area mean of column-integrated total tagged moisture (g m^{-2}) for area C during the first 40 hours (08:00 CST 01 October to 00:00 CST 03 October 2004). Dots indicate the corresponding time sequence chosen in Figure 5.2.

Figure 5.3 shows a time series of the column-integrated total tagged moisture averaged over area C during the first two days in October. The tagged moisture content increases almost monotonically in the model atmosphere before 20:00 CST 01 and decreases during the following night. The two-day fluctuations reflect the comprehensive interactions among the daily cycles of evapotranspiration, the formation of precipitation, and the loss due to outflow at lateral model boundaries. More details about these comprehensive interactions on monthly scales are described in the following sections.

5.3.2 Distribution of Tagged Moisture in the Atmosphere

The tagged moisture evapotranspired from the source area S is transported and spread in the atmosphere vertically and horizontally. Figure 5.4 shows the vertical distribution of (a) the total tagged moisture (consisting of water vapor, cloud water, cloud ice, rain water, and snow), and (b) the condensed tagged moisture (i.e., the sum of tagged liquid and solid cloud and precipitation water) over the source area S on monthly scales. Most of the tagged moisture remains in the boundary layer, with the maximum mixing ratio near the surface. The atmospheric storage of the tagged moisture increases from January to June and decreases from September to December and is associated with changes in the height of the boundary layer. In summer, high temperatures lead to enhanced evapotranspiration at the land surface, to an expansion of the boundary layer and to an increased water-storage capacity of the atmosphere.

The vertical distribution of the *condensed* tagged moisture is more diverse from month to month and is directly related to the formation of clouds and precipitation systems (see Figure 5.4b). As a result of more frequent convection and large-scale lifting, the condensed tagged moisture is found in higher atmospheric layers in the rainy season and in the summer season. For example, in May the main rain belt covers over Southeast China and the formation of convective clouds results in the tagged water vapor lifted up and condensed in the upper atmosphere above the planetary boundary layer. In contrast, in winter the condensed tagged moisture is predominantly formed in the lower atmospheric layers. However, compared to the total tagged moisture, the condensed tagged moisture only accounts for a very small fraction.

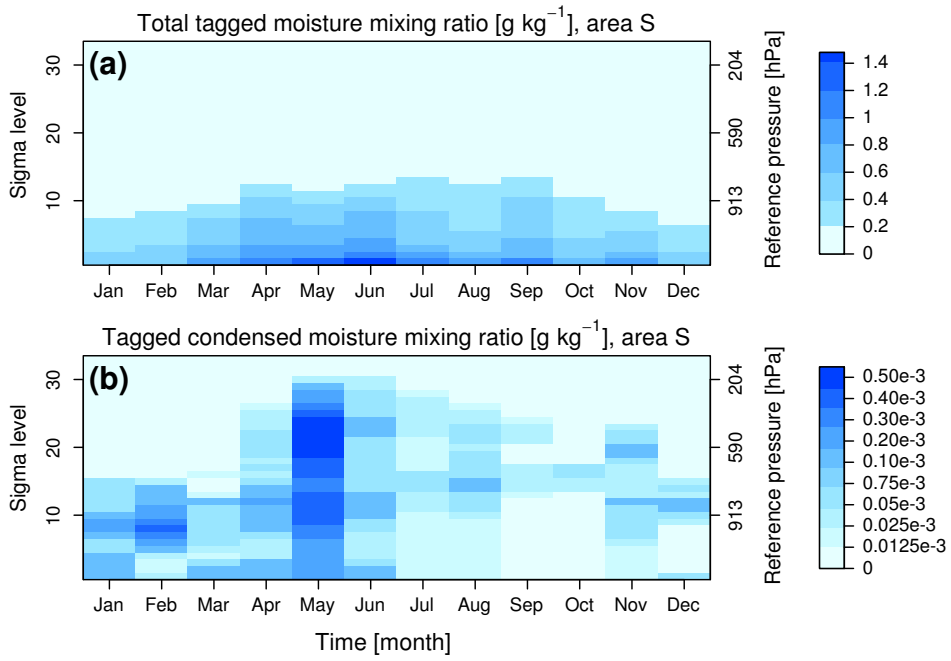

Figure 5.4: Monthly time series of vertical distribution of (a) total tagged moisture mixing ratio (g kg^{-1}) and (b) condensed tagged moisture mixing ratio (g kg^{-1}), averaged over area S for each model layer and for each month in 2005. The σ-values of the model levels are given in Table 4.1.

To study the transport and distribution processes of tagged moisture from the source area, monthly vertical profiles of the three wind components averaged over the source area S are shown in Figure 5.5. It illustrates the variability of wind speed and wind direction with height and season. The direction of the meridional wind component changes in April and September due to the onset and retreat of the East Asian summer monsoon, respectively. The vertical wind component near the land surface switches from slightly downward to upward, during the summer monsoon season, with the strongest updraft in May, especially in the higher levels.

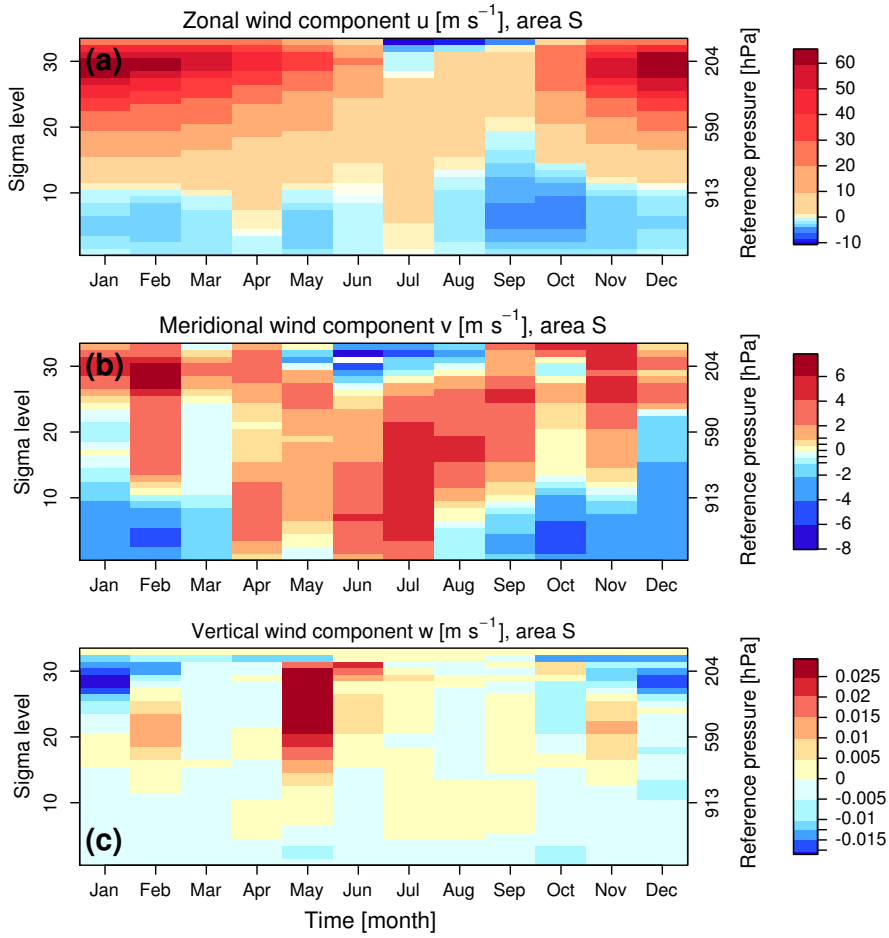

Figure 5.5: Monthly time series of vertical profile of wind components: (a) zonal velocity u (m s^{-1}), (b) meridional velocity v (m s^{-1}), and (c) vertical velocity w (m s^{-1}). The wind components are averaged over area S for each model layer and for each month in 2005.

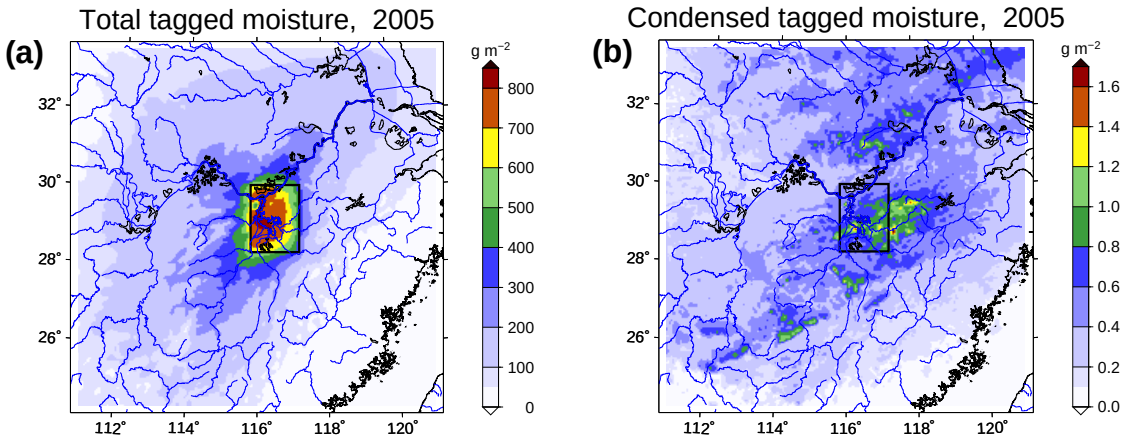

Figure 5.6: Horizontal distribution of (a) column-integrated total tagged moisture (g m^{-2}) and (b) column-integrated condensed tagged moisture (g m^{-2}), averaged for 2005. The color scale of (a) and (b) ends at 850 g m^{-2} and 1.7 g m^{-2}, respectively.

Figure 5.6a shows the horizontal distribution of the column-integrated total tagged moisture, average for 2005. Generally, the horizontal distribution of the total tagged moisture is governed by the wind direction changes due to the development and retreat of the East Asian monsoon (see Figure 5.5), and influenced by the topography of the Poyang Lake basin (see Figure 4.2d). Most of the total tagged moisture is found above the Poyang Lake area (around 850 g m^{-2}) and directly west of it, due to the easterly wind prevailing most of the year in the boundary layer (see Figure 5.5a). With increasing distance from the source area, the total tagged moisture content distinctly declines.

Figure 5.6b depicts the horizontal distribution of the column-integrated *condensed* tagged moisture. Most of the condensed tagged moisture is contained in the atmosphere above the Poyang Lake region and in the adjacent part to the East, and is, as suggested by Figure 5.4b, mainly formed during the rainy season. It indicates that the tagged moisture is involved in cloud formation and precipitating systems and is concentrated in the middle and high layers, where westerly winds dominate (see Figure 5.5b). The condensed tagged moisture found in the northern part of the domain results from the transportation processes by the prevailing southerly winds in summer. In contrast, the northerly winds in winter are responsible for the condensed tagged moisture appearing in the South.

5.3.3 Distribution of Tagged Precipitation over Land

Figure 5.7 shows the spatial distribution of the simulated total precipitation (left column) and tagged precipitation (middle column) for 2005. The patterns of the local precipitation contribution ratio ρ (equation 5.1) are also shown (right column). In addition to the annual sum, three months (February, May, and August) are selected for illustrating the monthly variations of the tagged precipitation and its contribution patterns due to the advance and retreat of the East Asian monsoon.

Overall, the tagged precipitation patterns in Figure 5.7b are similar to the condensed tagged moisture patterns (see Figure 5.6b). Most of the tagged precipitation in 2005 occurs around the source area S and in the adjacent part to the East with a maximum value of about 20 mm. In comparison to the total precipitation shown in Figure 5.7a, the tagged amount is nearly two orders of magnitude lower. Regions with a contribution ratio $\rho > 1.2\,\%$ are found in the source area and in the North along the Yangtze River Valley, about 200 km away from the Poyang Lake (Figure 5.7c). In contrast, the water evapotranspired from the Poyang Lake region does not significantly contribute to the precipitation in the southeast quadrant.

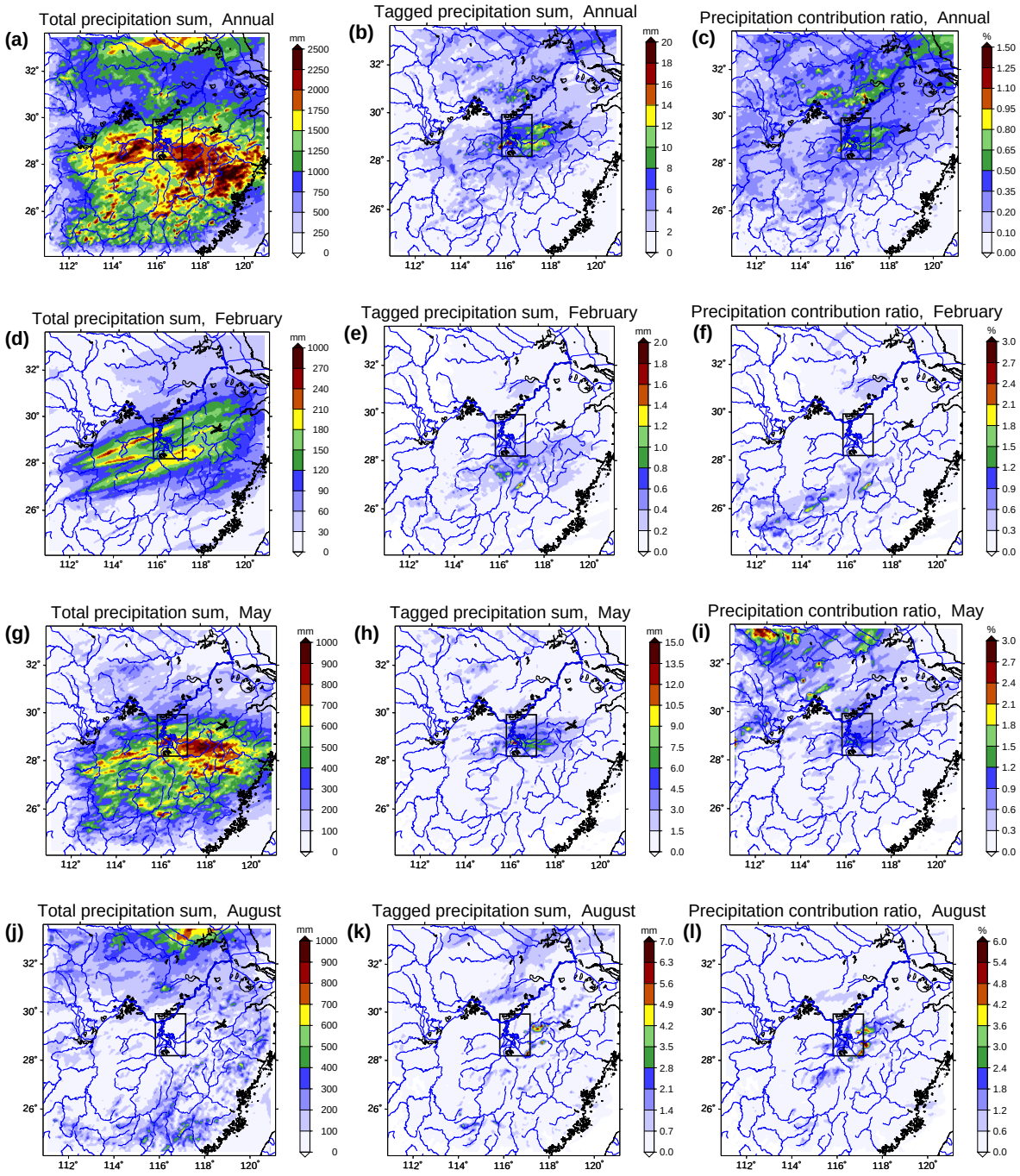

Figure 5.7: Annual sum and monthly sums of simulated total precipitation P_{total} in mm (left column) and of tagged precipitation P_{tag} in mm (middle column) for the whole year 2005 and three months (February, May, August) (from top to bottom). The right column shows annual/monthly local precipitation contribution ρ in % for the same periods.

In February, the maximum values of tagged precipitation (only 1.2 mm) are found south of the source area (Figure 5.7e), where the dominant northerly winds are close to the land surface (see Figure 5.5). A smaller amount of tagged precipitation is also formed in the North because of the repeated changes in wind direction. The pattern of the contribution ratio of the monthly mean precipitation ρ in Figure 5.7f exhibits a band-like structure, shifted towards the South in the downwind regions. In the North, despite very low tagged precipitation sums, the contribution ratio reaches around 0.6 % due to low values of total precipitation, too. After the onset of the East Asian summer monsoon in April, the prevailing low-level and upper-level winds rapidly reverse their directions. As discussed before, in May a large amount of condensed tagged moisture is locally involved in convective and large-scale precipitation processes. Therefore, the tagged precipitation amount reaches its maximum (15 mm) in the source area S and its surrounding regions (Figure 5.7h). The southerly winds also transport a small fraction of the tagged moisture towards the North, with some tagged precipitation occurring. Due to the low values of total precipitation (see Figure 5.7g), comparatively high contribution ratios are found in the North (Figure 5.7i). In August, due to the different wind directions near the land surface and in the upper-level atmosphere, the tagged precipitation falls not only in the North, but to a lesser extent also in the South (Figure 5.7k). Small fractions of condensed tagged moisture in higher model layers (see Figure 5.4b) lead to few local, convective rainfall events in and around the source area S, and to a contribution ratio of up to 6 % near the eastern boundary of the source area S (Figure 5.7l), which is also the maximum on monthly scales for the year 2005. The analysis of the selected three months reveals that the prevailing winds and the changing precipitation regime over Southeast China dominate the pattern of precipitation contribution. This finding is in general agreement with van der Ent et al. (2014).

5.3.4 Budget Analysis of Atmospheric Tagged Water

Table 5.1 summarizes the values of the tagged water budget terms on monthly scales for 2005. Overall, almost 90 % of the evapotranspired tagged water leaves the area C in 2005. Only 0.8 % of the tagged moisture precipitates locally in the source area S with monthly values between 0.1 % in October and 3.5 % in May. In contrast, the comparison of $P_{tag,C}$ and $P_{tag,S}$ shows that due to the annual movement of the East Asian monsoon, the tagged precipitation is more often formed outside of the source area S. Averaged over 12 months, the tagged precipitation falling in the Poyang Lake basin (area P) equates to 2.7 % of the tagged moisture with a maximum of 9.2 % in May. Considering area C (representing nearly the whole of Southeast China), 10.7 % of the tagged moisture returns as the tagged precipitation, with a maximum of 24.7 % in May. The tagged precipitation contribution ratios in areas S, P, and C reveal the

relevance of the evapotranspired water in the Poyang Lake region for tagged precipitation in Southeast China on different scales. Maximum values of tagged precipitation contribution ratios (i.e., significant recycling effects) are found in May when peak total (tagged and untagged) precipitation occurs.

In specific months like May and June but also in the months October to January, the wind regimes and the humidity of air masses over Southeast China change significantly. As a consequence, there are considerable differences in the atmospheric (tagged) moisture contents between the beginning and the end of the respective month. This explains the comparatively high values between -17 % and +16 % of the storage change term $\Delta Q_{tag,C}$.

Table 5.1: Atmospheric tagged water budget (equation 5.2) of the ET-Tagging simulation on monthly scales for 2005. Monthly sums and changes during a month ($\Delta Q_{tag,C}$) are shown as relative values compared to $ET_{tag,S}$ in % and as precipitable water in mm. Source and target areas (see Figure 4.2d) are indicated as subscript for each term (S: the Poyang Lake region; P: the Poyang Lake basin; C: Southeast China; PoS: the area outside of S but inside of P; CoPS: the area outside of P and S but inside of C).

	$ET_{tag,S}$		$P_{tag,S}$		$P_{tag,PoS}$		$P_{tag,CoPS}$		$\Delta Q_{tag,C}$		$F_{tag,C}$		$P_{tag,P}$		$P_{tag,C}$	
[Month]	[%]	[mm]	[%]	[mm]	[%]	[mm]	[%]	[mm]	[%]	[mm]	[%]	[mm]	[%]	[mm]	[%]	[mm]
1	100.0	28.6	0.6	0.2	2.7	0.2	5.0	0.1	12.5	0.1	79.2	-	3.3	0.2	8.3	0.1
2	100.0	34.9	0.6	0.2	3.0	0.2	7.4	0.1	-0.2	0.0	89.2	-	3.5	0.2	11.0	0.1
3	100.0	66.0	0.2	0.1	1.4	0.2	5.3	0.1	3.4	0.1	89.7	-	1.6	0.2	6.9	0.1
4	100.0	94.4	0.6	0.6	1.4	0.3	7.2	0.2	-9.5	-0.2	100.3	-	2.0	0.3	9.2	0.2
5	100.0	106.0	3.5	3.8	5.9	1.3	15.3	0.5	12.5	0.4	62.8	-	9.2	1.7	24.7	0.7
6	100.0	125.0	0.6	0.7	1.2	0.3	8.6	0.3	-11.8	-0.4	101.4	-	1.7	0.4	10.4	0.3
7	100.0	123.0	0.3	0.4	0.6	0.1	7.6	0.3	5.3	0.2	86.2	-	0.8	0.2	8.5	0.3
8	100.0	87.8	0.4	0.3	2.2	0.4	11.5	0.3	2.5	0.1	83.4	-	2.6	0.4	14.2	0.3
9	100.0	86.9	0.2	0.2	1.4	0.3	6.0	0.2	4.1	0.1	88.3	-	1.6	0.2	7.6	0.2
10	100.0	60.5	0.1	0.1	0.8	0.1	2.2	0.0	-16.1	-0.3	113.0	-	0.9	0.1	3.1	0.1
11	100.0	41.7	1.2	0.5	2.3	0.2	5.8	0.1	15.8	0.2	74.9	-	3.5	0.3	9.3	0.1
12	100.0	31.0	0.2	0.1	1.4	0.1	2.9	0.0	-16.9	-0.1	112.4	-	1.6	0.1	4.5	0.0
Total	100.0	888.8	0.8	7.2	2.0	3.7	7.9	2.2	-0.1	0.0	89.4	-	2.7	4.3	10.7	2.5

Chapter 6

Contribution of Transpiration and Evaporation to Precipitation

Changes of land-surface characteristics (e.g., soil, water bodies, and vegetation) can significantly alter the atmospheric branch of the hydrological cycle (Huntington, 2006) and can further modify climate variability (Karl and Trenberth, 2003; Seneviratne et al., 2006). With respect to the contribution of evapotranspiration to precipitation, however, what is the relative importance of transpiration and direct evaporation processes in the regional hydrological cycle? Partitioning evapotranspiration into biological transpiration and physical evaporation is extensively investigated (Lawrence et al., 2007; Hu et al., 2014; Coenders-Gerrits et al., 2014) and reviews on the approaches for partitioning are given, e.g., by Wang and Dickinson (2012) and Kool et al. (2014).

Globally, the land masses provides more transpiration (61 % ± 15 % s.d. of evapotranspiration) than direct evaporation. This means that transpiration dominates the terrestrial water cycle (Jasechko et al., 2013; Schlesinger and Jasechko, 2014). The local recycling over the Yangtze River Valley is controlled by rainfall and circulation changes (Wei et al., 2012a). Recently, Wang-Erlandsson et al. (2014) and van der Ent et al. (2014) depicted the contrasting roles of interception and transpiration in the hydrological cycle in the context of moisture recycling, and stressed the potential influence of the land surface on the hydrological cycle. By analyzing the "precipitationsheds", Keys et al. (2012) and Keys et al. (2014) found that North China and East China are highly vulnerable to land-use change. Bagley et al. (2012) indicated a negative affect of land-use change on potential crop yields due to a shortage of moisture sources for the breadbasket regions, e.g., North China. An enhancement of moisture recycling has also been attributed to irrigation (Tuinenburg et al., 2012; Wei et al., 2012b; Lo and Famiglietti, 2013).

In this chapter, in order to investigate the relative importance of evaporation and transpiration processes in the regional hydrological cycle and the corresponding impact on land-atmosphere interaction, the total evapotranspiration is split into direct evaporation (consisting of evaporation from inland water bodies, evaporation from the top soil layer, and evaporation of precipitation intercepted by the canopy, (see equation 3.9)) and transpiration (see equation 3.10). Individual evaporation and transpiration fluxes are calculated within a sophisticated land surface scheme (Oregon State University Land Surface Model OSU-LSM) in the regional climate model (MM5). They represent different dynamical effects of land-surface characteristics and of hydrological processes (Jacobs and De Bruin, 1992; Sewall et al., 2000; Wang and Dickinson, 2012; Wang-Erlandsson et al., 2014; van der Ent et al., 2014). A detailed description of the technical implementation was given in Chapter 3.3.

For the ET-Tagging partitioning study on the Poyang Lake region over Southeast China, this extended model is employed to conduct two model runs (RunTagE_d and RunTagE_t) to track direct evaporation and transpiration fluxes separately through the atmosphere. Including the results of the partitioning of tagged precipitation corresponding to partitioning of evapotranspiration, the relative contributions of the individual evapotranspiration components are presented. The source-target relations under consideration of the respective precipitation regime are explored.

6.1 Analysis Methods

In the context of ET-Tagging partitioning (see Chapter 3.3), the tagged evapotranspiration is split into tagged direct evaporation $E_{d,tag}$ and tagged transpiration $E_{t,tag}$

$$ET_{tag} = E_{d,tag} + E_{t,tag} \tag{6.1}$$

The tagged precipitation can be split accordingly as:

$$P_{tag} = P_{tag,E_d} + P_{tag,E_t} \tag{6.2}$$

To explore further the source-target relations under consideration of the respective precipitation regime (wet or dry weather conditions), the source-specific precipitation efficiency is introduced

$$\eta = P_{tag}/ET_{tag}, \tag{6.3}$$

describing the relation of water that enters the domain from a specific source area by evapotranspiration and that subsequently falls as precipitation. In contrast to the precipitation efficiency defined in other studies (Schär et al., 1999; Kunstmann and

Jung, 2007), the focus here is on the evapotranspired water from a specific source area rather than from the whole domain or from the outside. Similarly, in the context of ET-Tagging partitioning, the source-specific precipitation efficiency for direct evaporation is defined as

$$\eta_d = P_{tag,E_d}/E_{d,tag} \tag{6.4}$$

and the source-specific precipitation efficiency for transpiration as

$$\eta_t = P_{tag,E_t}/E_{t,tag}. \tag{6.5}$$

6.2 Results and Discussion

6.2.1 Distribution of Annual Partitioned Tagged Precipitation

According to equation (6.2), the tagged precipitation can be partitioned and separately analyzed. Figures 6.1a and 6.1b show the annual sum of P_{tag,E_d} and P_{tag,E_t} for 2005. Aggregated over area C, 69 % of the tagged precipitation is contributed by direct evaporation, and 31 % by transpiration. While higher values of P_{tag,E_d} are found in most parts of area C with a pronounced maximum over the source area S, higher values of P_{tag,E_t} are limited to the region around the source area S and to (remote) northern areas. In these remote areas, large amounts of tagged transpired moisture in summer are transported by dominating southerly winds and subsequently contribute to precipitation. As a result, the distribution of the fraction $P_{tag,E_t}/P_{tag}$ in Figure 6.1c shows that the transpired water accounts for about half of the precipitation in the North. However, transpiration is far less important around the source area S and in the South ($P_{tag,E_t}/P_{tag} \leq 15\,\%$) due to the small contribution of tagged transpiration to total tagged evapotranspiration in winter.

Recently, van der Ent et al. (2014) found that in Southeast China the continental precipitation recycling ratio for transpiration is larger than that for evaporation. This stands in contrast to the findings here and is mainly ascribed to the different representations of land-surface characteristics of the source areas in the two studies. The continent as a source area provides much more transpiration than direct evaporation. This means that transpiration dominates the terrestrial water cycle (Jasechko et al., 2013; Schlesinger and Jasechko, 2014; Wang-Erlandsson et al., 2014). By contrast, the source area in this study has a large fraction of moist land-use types (water bodies and wetlands) with direct evaporation. This process is more effective for water at or near the surface than transpiration for water from the root zone (Jasechko et al., 2013). Overall, the different finding reveals that the vegetation cover and land-use type have important impacts on the regional atmospheric hydrological cycle.

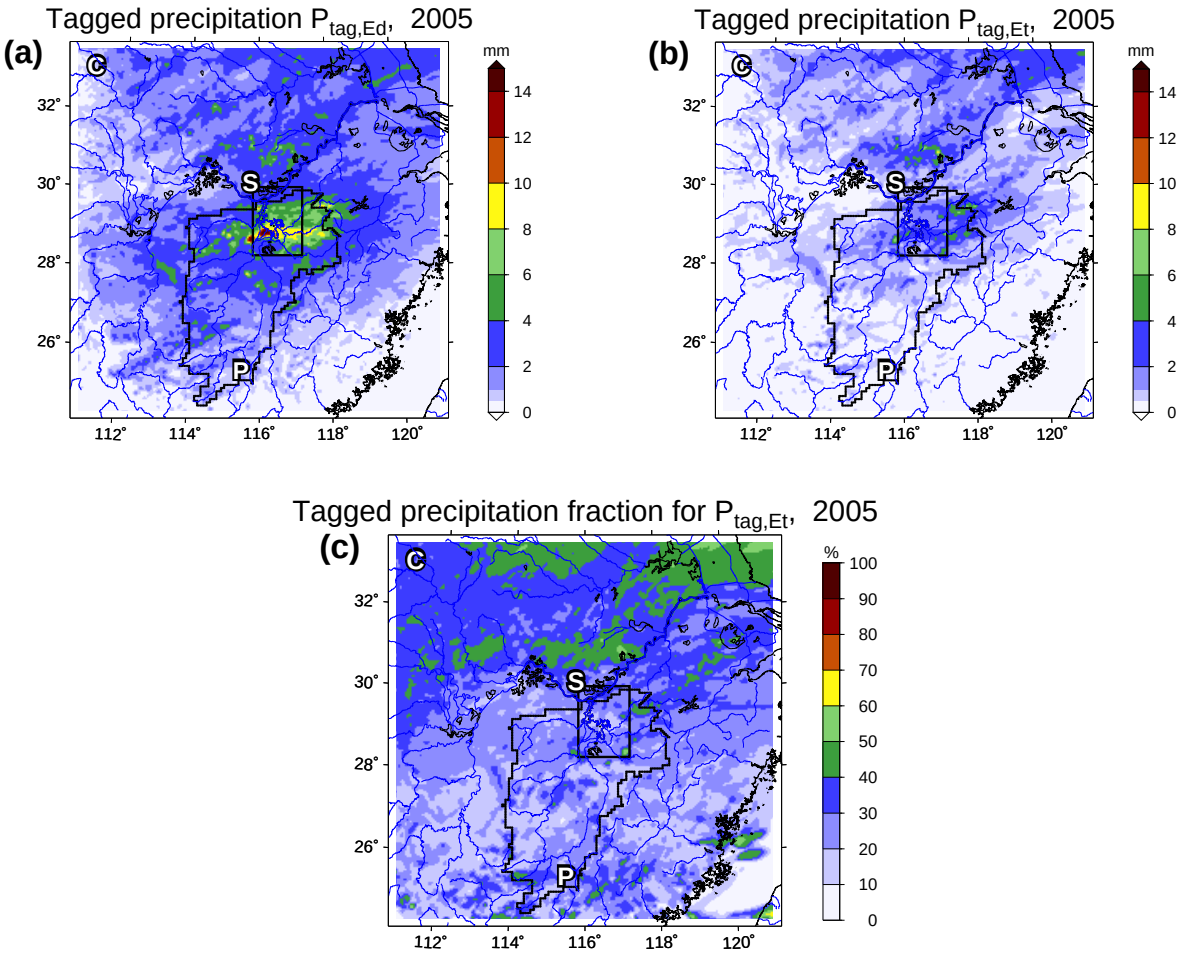

Figure 6.1: Annual sum of the simulated (a) tagged precipitation P_{tag,E_d} (mm) for direct evaporation, (b) tagged precipitation P_{tag,E_t} (mm) for transpiration, and (c) annual mean of tagged precipitation fraction $P_{tag,E_t}/P_{tag}$ (%) for transpiration for the year 2005. S denotes the source area, i.e., the Poyang Lake region. P denotes the Poyang Lake basin, and C denotes Southeast China.

6.2.2 Variation of Monthly Partitioned Tagged Precipitation

Next, the distribution of evapotranspiration and tagged precipitation is investigated on a monthly basis. Figure 6.2a shows time series of monthly area mean of ET_{tag} and the corresponding partitioning over area S for 2005. Except for July, August and September, the direct evaporation fluxes $E_{d,tag}$ show significantly higher values than the transpiration fluxes. They reach their maximum during the rainy season, since a large amount of water is available at the land surface and on the canopy of the fully developed vegetation. The monthly variation of the transpiration fraction $E_{t,tag}$ coincides with the seasonal changes in temperature. Since the land surface model in

this study uses a prescribed seasonal varying climatological green leaf area index and green vegetation fraction, increasing temperatures reflect promoting transpiration and allow for more water uptake from the root zone. Thus, the highest values of $E_{t,tag}$ are found from June to September.

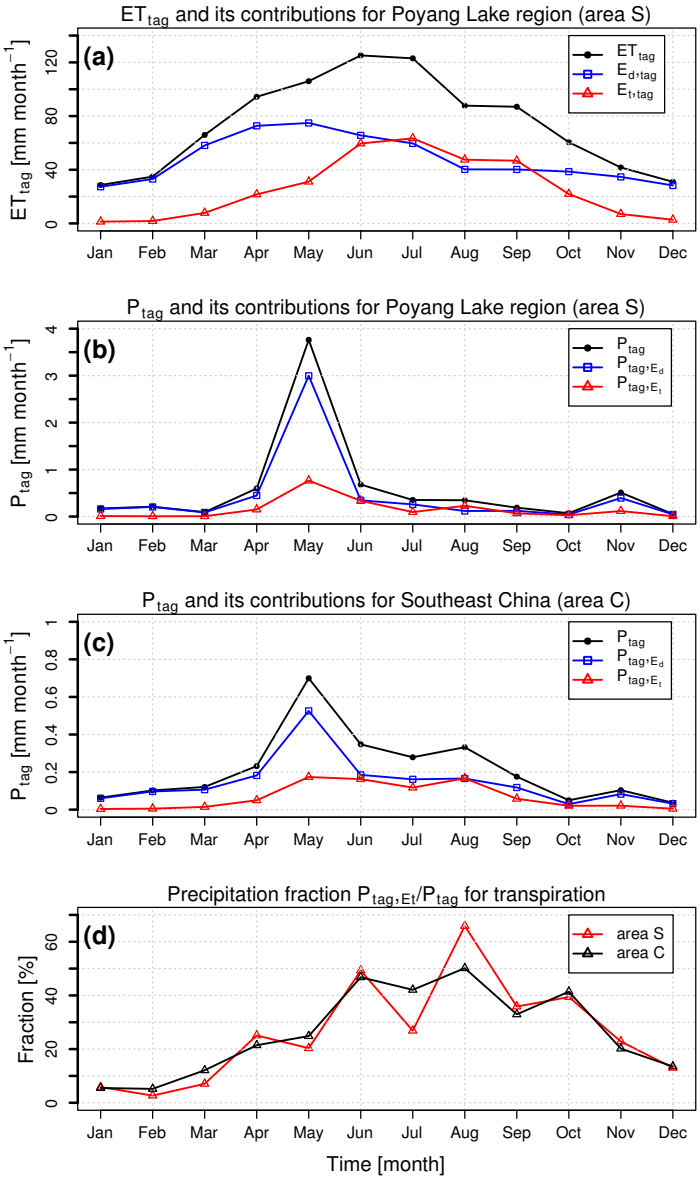

Figure 6.2: Time series of monthly area mean of (a) evapotranspiration ET_{tag} (black) and its contributions direct evaporation $E_{d,tag}$ (blue) and transpiration $E_{t,tag}$ (red) (mm month^{-1}) for area S, (b) tagged precipitation P_{tag} (black) and the contributions for direct evaporation P_{tag,E_d} (blue) and for transpiration P_{tag,E_t} (red) (mm month^{-1}) for area S, (c) as in (b), except for area C, and (d) precipitation fraction $P_{tag,E_t}/P_{tag}$ for transpiration for area S (red) and for area C (black) (%).

Correspondingly, time series of monthly area mean of the tagged precipitation P_{tag} and its fractions P_{tag,E_d} and P_{tag,E_t} over the source area S and over the target area C are shown in Figures 6.2b and 6.2c. In general, since little tagged precipitation for transpiration is found in winter and in the transit seasons, almost all of the tagged precipitation during these periods originates from direct evaporation. In the summer season, the transpiration becomes more important for the formation of tagged precipitation. For the small source area S, both P_{tag,E_d} and P_{tag,E_t} show the largest values in May (Figure 6.2b), in accordance with peak total (tagged and untagged) precipitation. For the large target area C, the time series of the tagged precipitation (Figure 6.2c) follows the trend of the source area S (see Figure 6.2b), but with less variation and markedly lower values in May, since P_{tag,E_t} is concentrated around the source area S due to frequent, local rainfall events. Relatively high values for P_{tag,E_t} persist from May to August.

Additionally, time series of the ratio $P_{tag,E_t}/P_{tag}$ for transpiration are given in Figure 6.2d. Larger fractions of $P_{tag,E_t}/P_{tag}$ for the source area S are found in June and August with maximum ratios of around 50 % and 66 %. For area S, in May, due to the large amount of P_{tag,E_d} formed, P_{tag,E_t} only accounts for 25 % of P_{tag}, while in the dry and warm season (from June to August), P_{tag,E_t} accounts for around 50 % of P_{tag}.

The comparison of the monthly precipitation ratios over the source area S and over area C (see Figure 6.2d) reveals that in specific months, large fractions of direct evaporated moisture and of transpired moisture are affected by different precipitation regimes. For example, in July, transpired water is transported over long distances and involved in remote rainfall events. In contrast, for example, local (area S) precipitation contribution by transpiration is more significant in August.

6.2.3 Analysis of Source-Target Relations

Figures 6.3a and 6.3b show the monthly values of the source-specific precipitation efficiencies η_d and η_t for the source area S and area C. The monthly variation of these parameters, which reflects different precipitation regimes, is closely connected to the monthly variation of the tagged precipitation and its fractions (see Figures 6.2b and 6.2c). Generally, higher source-specific precipitation efficiencies imply a larger amount of precipitation being formed. As a result, the highest values of tagged precipitation are found in the rainy season in May, when the source-specific precipitation efficiencies also reach the highest values both for area S and for area C. For the small source area S, the source-specific precipitation efficiencies show a wider range of seasonal variation (Figure 6.3a). With the target area being larger (area C), the averaged source-specific precipitation efficiencies are lower and more uniform (Figure 6.3b).

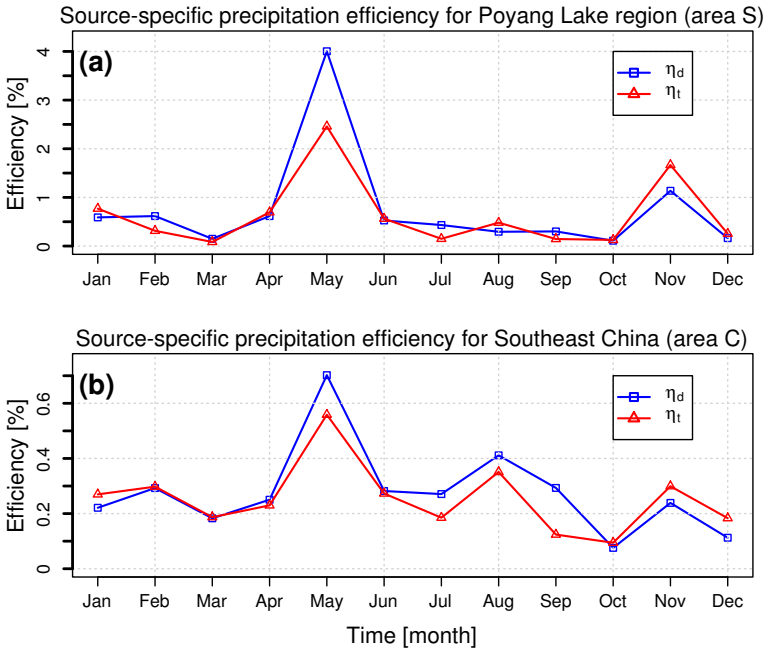

Figure 6.3: (a) Time series of monthly source-specific precipitation efficiencies for direct evaporation η_d (%) in blue and for transpiration η_t (%) in red for area S, (b) as in (a), except for area C.

Chapter 7

Atmospheric Residence Times from Transpiration and Evaporation to Precipitation

It is understood that human-induced global warming leads to an enhancement of the evapotranspiration process and thereby to an acceleration of the atmospheric branch of the hydrological cycle. This is supported by empirical evidence (Huntington, 2006), modeling studies (Allen and Ingram, 2002), and theoretical expectation (the Clausius-Clapyeron relation) (Held and Soden, 2006). Although the acceleration of the hydrological cycle is generally acknowledged, it is still challenging question of how the hydrological cycle changes as the climate changes (Trenberth, 1999a).

The response of the hydrological cycle to the climate regime can be studied by investigating, for example, the relationship between evapotranspiration and precipitation, particularly the celerity of the processes transferring from evapotranspired water to precipitating water. To quantify this celerity, the concept of atmospheric residence time, here defined as lifetime between the original evapotranspiration and the returning of its respective water masses to the land surface as precipitation, is used in various studies (Trenberth, 1998; Numaguti, 1999; James et al., 2003; Tuinenburg et al., 2012; Wang-Erlandsson et al., 2014; van der Ent, 2014). It is a fundamental descriptor that provides additional information on the timescales of evapotranspiration and precipitation and reflects the complexity of the atmospheric water pathways and the phase changes including the formation of precipitation. In addition, a probability density function (PDF) of residence times, hereafter referred to as residence times distribution (RTD), allows to characterize the natural atmospheric hydrological cycle for different regimes and seasons. Apart from atmospheric science, this concept has been also extensively applied in numerous fields of geophysics (McGuire and McDonnell, 2006; Harman

and Kim, 2014), e.g., in the hydrologic studies on rainfall-runoff response (Hrachowitz et al., 2013) and on groundwater age distributions (Gomez and Wilson, 2013). A detailed overview and interpretation of this concept are given by Bolin and Rodhe (1973), Zuber (1986), and McGuire and McDonnell (2006).

There are only a few studies calculating atmospheric water residence times. By using an atmospheric general circulation model in conjunction with moisture tracers, Numaguti (1999) investigated the mean age of the precipitating water from the oceanic and from the continental origins in Eurasia. A Lagrangian particle dispersion model in which particles act as tracers has been employed for assessing the exchange rate of air parcels between stratosphere and troposphere on a global scale (James et al., 2003). Trenberth (1998) used a function for depletion of precipitable water by precipitation and calculated the global mean residence time of atmospheric moisture as 8.1 days. Additionally, environmental tracers and passive modeled tracers are utilized often as a combined observational and modeling approach to calculate residence times and corresponding distributions (Gomez and Wilson, 2013).

The RTD for water evaporated from the Ganges basin has been estimated by Tuinenburg et al. (2012) using a quasi-isentropic moisture tracking scheme. The global atmospheric lifetime of recycled moisture was studied by van der Ent (2014). These and similar other modeling studies either have been conducted on large scales with a coarse resolution or have used relatively simple schemes for atmospheric dynamical and physical processes. This may limit the accuracy of estimates of atmospheric residence times, e.g., due to an inadequate representation of the complex atmospheric features, especially, when directional wind shear is present or strong moist convection happens (Goessling and Reick, 2013; van der Ent et al., 2013).

To overcome these difficulties, the RCM-based ET-Tagging partitioning algorithm is extended again by including a mechanism to calculate the atmospheric water residence times for moisture originated from a specific region (more details shown in Chapter 3.4). The newly extended model is applied in the research scope of land-atmosphere interactions to a case study over the same study area, i.e., the Poyang Lake region.

In this chapter, the age-weighted extended model is employed to address the research question of how long the lifetime is between the original evapotranspiration (transpiration and evaporation) in the Poyang Lake region and the subsequent precipitation. To our knowledge, an RCM-based algorithm for calculating atmospheric water residence times has not yet been used for the subtropical and mountainous Southeast China. Thus, the objectives of this chapter are (1) to introduce and demonstrate a process-based, three dimensional regional climate model-based algorithm for the calculation of atmospheric water residence times, (2) to apply this extended model for the first time in Southeast China, and (3) to investigate the spatial and temporal variations

of atmospheric residence times of the direct evaporated and transpired water from the Poyang Lake region.

For the application of the age-weighted ET-Tagging partitioning algorithm, the experimental design here closely follows that described in Chapter 5.1. To assess the atmospheric residence times of the evapotranspired (RunAgeET), direct evaporated (RunAgeE_d), and transpired (RunAgeE_t) water, three long-term model runs are performed for the period from October 2004 to December 2005. The analysis is limited to the entire year 2005 after 3 months spin-up time on a monthly scale. To demonstrate the age-weighted regiomal ET-tagging approach, the focus is on the formation of tagged and age-weighted tagged moisture in the first 48 hours during the spin-up period of the simulation for the evapotranspired water.

7.1 Analysis Methods

The atmospheric residence times of moisture is calculated by

$$\tau_k = q_{k,age}/q_{k,tag} \tag{7.1}$$

and the atmospheric residence times of precipitated water by

$$T_P = P_{age}/P_{tag}. \tag{7.2}$$

In the context of ET-Tagging partitioning, the atmospheric residence times τ_{k,E_d} of tagged moisture components $q_{k,tagE_d}$ formed by direct evaporation E_d and the atmospheric residence times τ_{k,E_t} of tagged moisture components $q_{k,tagE_t}$ formed by transpiration E_t are defined as

$$\tau_{k,E_d} = q_{k,ageE_d}/q_{k,tagE_d} \tag{7.3}$$

$$\tau_{k,E_t} = q_{k,ageE_t}/q_{k,tagE_t}. \tag{7.4}$$

Similarly, the atmospheric residence times T_{P,E_d} of tagged precipitation P_{tag,E_d} contributed by direct evaporation and the atmospheric residence times T_{P,E_t} of tagged precipitation P_{tag,E_t} contributed by transpiration are defined as

$$T_{P,E_d} = P_{age,E_d}/P_{tag,E_d} \tag{7.5}$$

$$T_{P,E_t} = P_{age,E_t}/P_{tag,E_t}. \tag{7.6}$$

7.2 Results and Discussion

7.2.1 Illustration of Dynamical Evolution

To demonstrate the age-weighted ET-Tagging algorithm, the first 48 hours of the model run RunAgeET is considered as simulating the formation of tagged and age-weighted tagged moisture originating from the evapotranspired water. The results are shown in Figures 7.1 and 7.2. The evolutions of the tagged moisture, of the age-weighted tagged moisture, and of the corresponding atmospheric residence times are displayed for five selected times between 00:00 UTC 1 and 24:00 UTC 2 in October 2004. The figures reveal the variations due to differences of the evapotranspiration and of the atmospheric transport conditions.

Figure 7.1 shows the spatial distribution of the column-integrated total tagged moisture Qt_{tag} (consisting of water vapor, cloud water, cloud ice, rain water, and snow) (left column), the age-weighted total tagged moisture Qt_{age} (middle column), and the age τ_{Qt} of the total tagged moisture (right column) over Southeast China at the selected five times. In addition, the hourly mean of the simulated horizontal wind field at 10-meter is shown as well. At the start of the simulation at 08:00 in the Chinese Standard Time (CST) zone (00:00 UTC) on 1 October in 2004, tagged moisture and age-weighted tagged moisture are set to zero. After that, evapotranspired water from the source area S is tagged when entering the atmosphere, and the age-weighting processes of tagged moisture components are triggered. Then, both the tagged moisture Qt_{tag} and the age-weighted tagged moisture Qt_{age} undergo the same atmospheric processes (i.e., transport by the wind fields and phase transitions) as the (original) total moisture. Figures 7.1a and 7.1b demonstrate the transport and spreading controlled by the wind fields after one hour of simulation. Finally, the tagged moisture and the age-weighted tagged moisture can leave the model domain (see Figures 7.1d, 7.1g, and Figures 7.1e, 7.1h) or can return to the land surface as tagged precipitation and age-weighted tagged precipitation. Moreover, during these 48 hours, the role of the precipitation is not yet significant. The day-night change in temperature leads to the fluctuation of the amount of evapotranspired water and thereby impacts the variations of the Qt_{tag} and the Qt_{age} patterns. Figures 7.1g and 7.1h show that little tagged moisture and little age-weighted tagged moisture are found over the source area S due to the limited water evapotranspired in the cold hours after midnight (i.e., 02:00 CST 2 October). With incoming radiation and rising temperature in the second day (i.e., 2 October), Qt_{tag} and Qt_{age} increase and undergo the transport and spreading processes again (see Figures 7.1j, 7.1m and Figures 7.1k, 7.1n).

The mean age τ_{Qt} patterns of the total tagged moisture in Figure 7.1 (right column) are generally controlled by two factors: the magnitudes of the newly tagged evapotran-

spired water compared to the magnitudes of the already existing tagged moisture and the atmospheric transport conditions. Within the first hour of the simulation, the τ_{Qt} pattern spreads towards the South due to the northerly winds (see area S in Figure 7.1c). In addition, the north-south lifetime gradient is pronounced. Comparatively fresh total tagged moisture with a low age (< 0.3 hours) is found over the northern part of the source area S since the atmosphere here contains a large proportion of the newly tagged evapotranspired water. Over the southern part of the source area S, τ_{Qt} is around 0.5 hours (approximately the averaged age of the tagged moisture in the domain), attributed to the mixing between the newly and the already existing evapotranspired water. In contrast, the total tagged moisture out of the source area S has a mean age up to 0.96 hour since there is no direct supply of fresh moisture.

Figure 7.1f depicts the τ_{Qt} pattern at the model time 11 hours just before a large amount of the older total tagged moisture starts to leave the area C (see Figure 7.1d). An age with values larger than 8 hours is also found over the adjacent part in the East and Southeast of the source area S despite the small absolute values of the total tagged moisture, which may be mainly caused by repeatedly wind direction changes. Figures 7.1i, 7.1l, and 7.1o show the age patterns on the second day at the selected three local times, consisting of early morning (Figure 7.1i), afternoon (Figure 7.1l), and night (Figure 7.1o). Due to gradually decreasing wind speed, the contoured age pattern with a large gradient tends now to be centered on the source area S.

Figure 7.2 shows time series of hourly means of (a) total tagged moisture, (c) age-weighted total tagged moisture, and (e) age of total tagged moisture, averaged over the analysis area C, and (b), (d), (f) the corresponding hourly net changes, during the first 48 hours in October 2004. The tagged moisture content increases almost monotonically in the model atmosphere till 20:00 CST 1 October, decreases during the following evening and night, and increases again after sunrise on the next day (Figure 7.2a). The fluctuations reflect the comprehensive interactions among the daily cycles of evapotranspiration, the formation of precipitation (to a lesser degree), the spatial redistribution due to various transport processes, and the loss due to outflow at lateral model boundaries. The trend of reduction of the total tagged moisture content (negative net change) during the nighttime follows the trend of enrichment (positive net change) during the daytime (Figure 7.2b). Within the first 12 hours, the total tagged moisture nearly linearly increases, whereas the age-weighted tagged moisture shows a non-linear increasing trend due to the age-weighting process, with a nearly linear increment of the hourly net changes as time elapses (Figure 7.2d). Later in the evening, the age-weighted total tagged moisture switches from gain (positive change) to loss (negative change) (at 22:00 CST 1 in Figure 7.2d) with an one hour lag compared to the total tagged moisture (at 21:00 CST 1 in Figure 7.2d). The mean age (Figure 7.2e) of the total tagged moisture averaged over the analysis area C increases from 08:00 CST 1 until 19:00 CST 1 before large amounts of the total tagged moisture leaves the

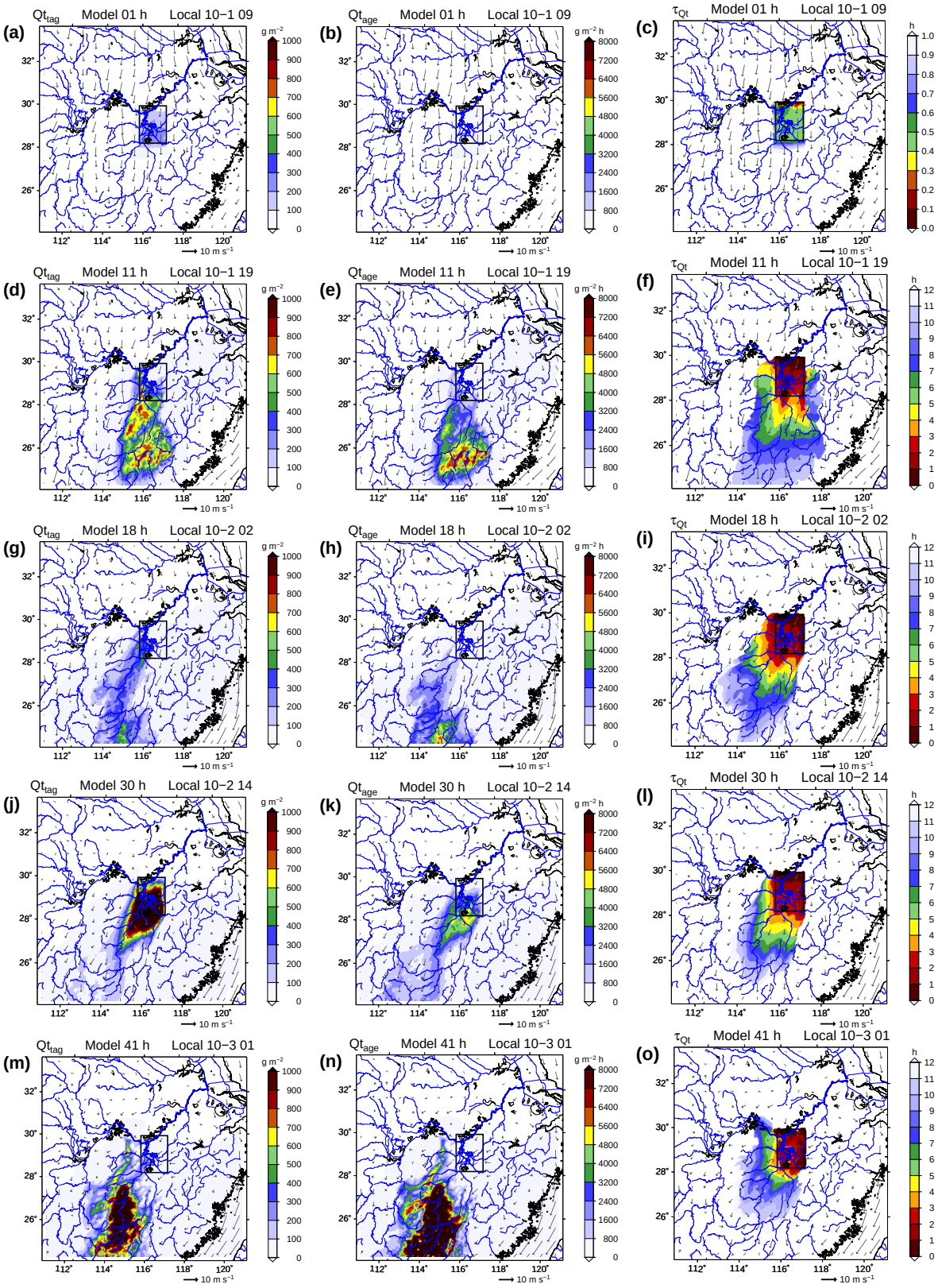

Figure 7.1: Horizontal distribution of column-integrated total tagged moisture Qt_{tag} in g m^{-2} (left column), column-integrated age-weighted total tagged moisture Qt_{age} in g m^{-2} h (middle column), and age τ_{Qt} of column-integrated total tagged moisture in h (right column) at different times during the first simulated 48 hours (00:00 UTC 1 to 24:00 UTC 2) in October 2004. The source area S lies within the black rectangle.

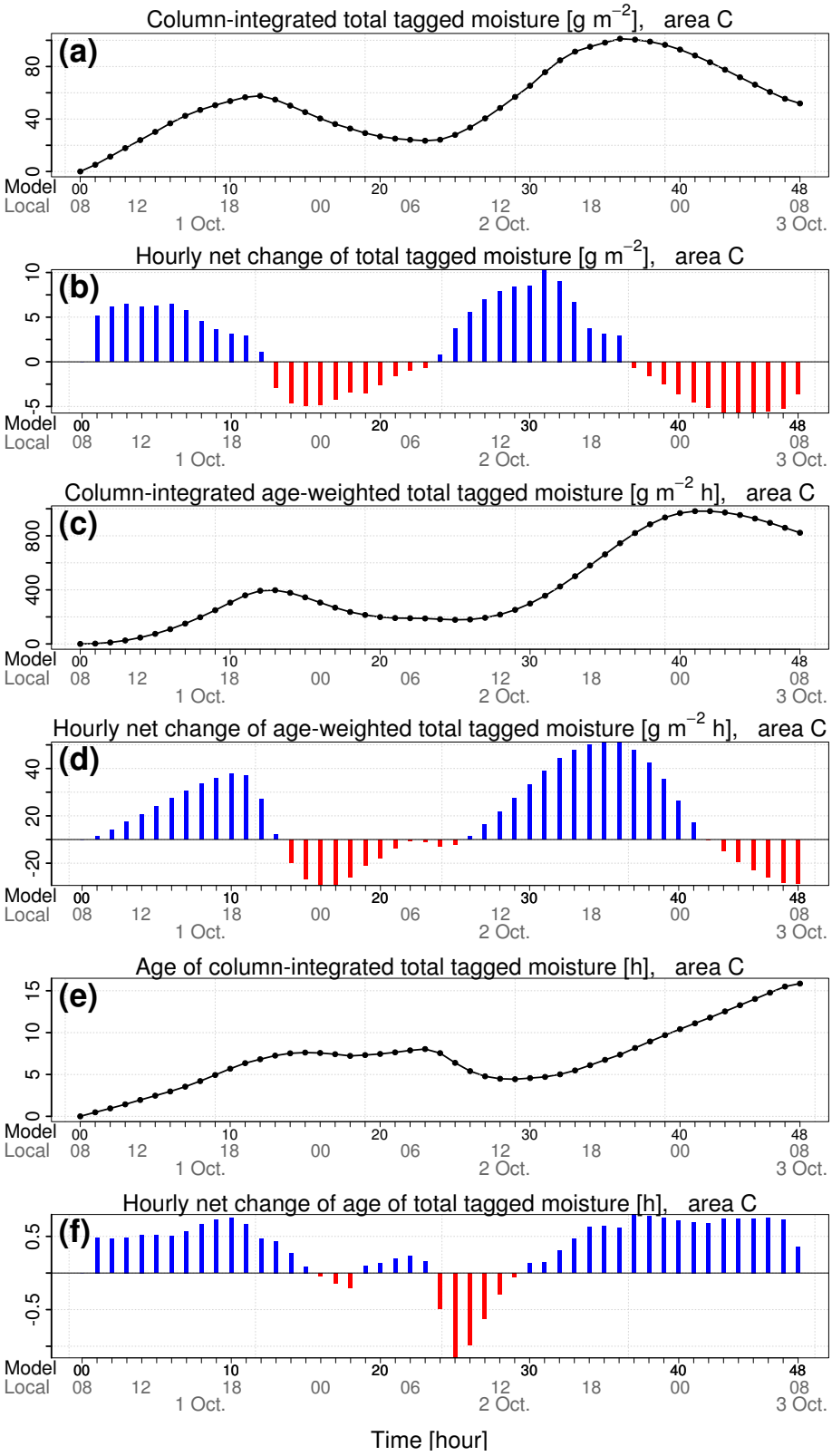

Figure 7.2: Time series from 08:00 CST 1 to 08:00 CST 3 in October 2004 of (a) column-integrated total tagged moisture Qt_{tag} in g m^{-2}, (c) column-integrated age-weighted total tagged moisture Qt_{age} in g m^{-2} h, (e) age τ_{Qt} of column-integrated total tagged moisture in h, and (b, d, f) correspondingly hourly net changes, averaged over the analysis area C.

analysis area (see Figure 7.1d). In the first hour, the increase is nearly linear, after that it tends to be even stronger, since the weakening evapotranspiration process (see Figure 7.2b) can only slightly refresh the large amount of the already existing (old) total tagged moisture within area C (see Figures 7.1e and 7.2d). In the following, the total tagged moisture becomes younger when the loss-induced decrease of the old total tagged moisture predominates, e.g., during the two periods (00:00-02:00, 08:00-13:00, CST 2).

7.2.2 Residence Times of Tagged Moisture in the Atmosphere

The atmospheric water residence times are now derived from the long-term run, i.e., the full year 2005. Figure 7.3 (upper panel) shows the vertical distribution of (a) the total tagged moisture qt_{tag}, (b) the age-weighted total tagged moisture qt_{age}, and (c) the mean age of the total tagged moisture τ_{qt} averaged over the analysis area C on monthly scales. Generally, the vertical profile of qt_{age} shows the same patterns as that of qt_{tag}: the values are dominated by the water vapor portion and are therefore high in the lower part of the atmosphere, especially during the rainy, warm season (April-June) (Figures 7.3a and 7.3b). The mean age of the total tagged moisture shown in Figure 7.3c varies from only 13 hours near the surface, to around 60 hours close to the planetary boundary layer top, to larger than 110 hours in the upper atmosphere. In the boundary layer, the total tagged moisture in summer is younger (lower values of the mean age) than in winter, which reveals that generally the atmospheric branch of the hydrological cycle in summer proceeds faster than in winter.

To examine the intensity of the cloud and precipitation formation, monthly vertical profiles (d) of the *condensed* tagged moisture qd_{tag} (i.e., the sum of tagged liquid and solid cloud and precipitation water), (e) of the age-weighted condensed tagged moisture qd_{age}, and (f) of the corresponding mean age τ_{qd} are shown in Figure 7.3 (lower panel). The vertical distribution of patterns of qd_{tag} and qd_{age} exhibits significant differences from month to month. In winter, most of the condensed tagged water is formed in lower layers with a mean age of around 4 hours, only a very small amount is found far above the boundary layer with a higher mean age, e.g., around 10 hours in February and March. In contrast, in the rainy season and in the summer months, large-scale lifting and frequent convection result in a low age (around 3 hours) above the planetary boundary layer and in a higher age (around 6 hours) within the boundary layer. The different age profile in winter and summer indicates the diverse precipitation regimes. Moreover, the lower absolute values of the mean age of the condensed tagged moisture in summer than in winter suggest that the response of cloud and precipitating formation in summer is faster than in winter.

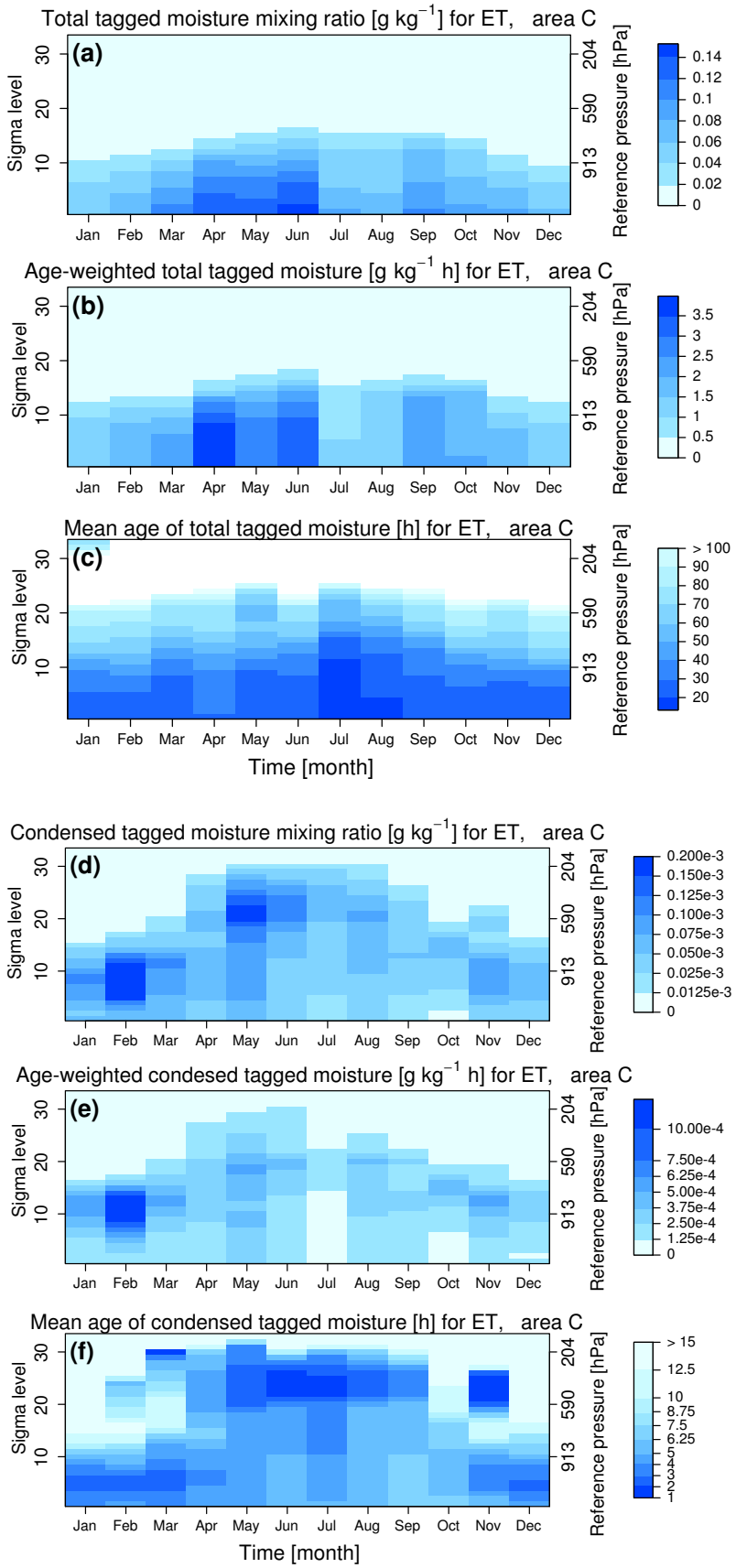

Figure 7.3: Time series of vertical distribution of (a) total tagged moisture mixing ratio qt_{tag} in g kg^{-1}, (b) age-weighted total tagged moisture qt_{age} in g kg^{-1} h, and (c) mean age τ_{qt} of total tagged moisture in h, averaged over area C for each model layer and for each month in 2005. Lower panel shows same as upper panel but for condensed tagged moisture.

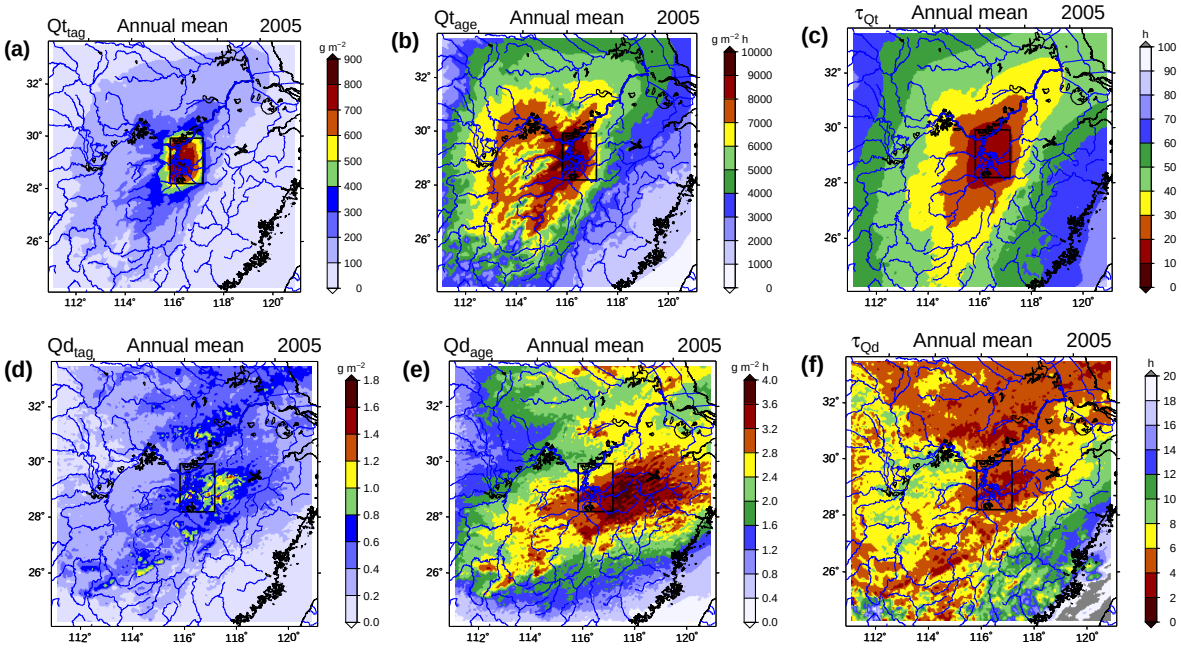

Figure 7.4: Annual mean of simulated column-integrated (a) total tagged moisture Qt_{tag} in g m^{-2}, (b) age-weighted total tagged moisture Qt_{age} in g m^{-2} h, (c) age τ_{Qt} of total tagged moisture in h, for the year 2005. Lower row (d-f) shows the same as the upper row but for annual mean of simulated column-integrated condensed tagged moisture.

Figure 7.4 (upper row) shows the horizontal distribution of (a) the column-integrated total tagged moisture Qt_{tag}, (b) the column-integrated age-weighted total tagged moisture Qt_{age}, and (c) the corresponding mean age τ_{qt} averaged for 2005. Generally, the values of Qt_{tag} and Qt_{age} decrease with distance from the source area with similar patterns. On the other hand, the age of the tagged moisture principally increases with increasing distance from the source area (Figure 7.4c). The values range from around 11 hours over the source area S up to 90 hours over the southeastern and northwestern corners of area C. Averaged over area C, the mean age of the total tagged moisture is around 36 hours. Spatially, the northeast-southwest expanding pattern reflects the differently prevailing wind directions in the winter monsoon and summer monsoon controlled seasons. Additionally, the gradient of the mean age towards the Northeast is lower than that towards the Southwest. It indicates that large amounts of fresh total tagged moisture are transported with strong southeasterly winds in summer, while small amounts of the old total tagged moisture are transported with weak northwesterly winds in winter.

Figure 7.4 (lower row) shows the horizontal distributions for the *condensed* parts. The horizontal distribution of the column-integrated age-weighted condensed tagged moisture Qd_{age} (Figure 7.4e) generally follows the distribution of Qd_{tag} (Figure 7.4d). In comparison to the patterns for the total tagged moisture (see Figure 7.4c), the

mean age patterns of the condensed part (Figure 7.4f) are distinctly different and the values are much lower (around 8 hours). Moreover, the comparison between Figure 7.4d and Figure 7.4f shows that, generally, larger values of the condensed tagged moisture correspond with lower age in the atmosphere.

7.2.3 Residence Times of Tagged Precipitation over Land

Figure 7.5 shows the spatial distribution of the simulated tagged precipitation P_{tag} (left column), and the age-weighted tagged precipitation P_{age} (middle column) for the total year 2005 and three selected months (February, May, and August). The patterns of the age T_P are depicted as well (right column). Accumulated over the year 2005, the horizontal distribution of the tagged precipitation patterns P_{tag} (Figure 7.5a) are closely related to the condensed tagged moisture patterns Qd_{tag} (Figure 7.4d). Similarly, the age-weighted tagged precipitation distribution P_{age} in Figure 7.5b appears like the distribution of Qd_{age} (see Figure 7.4e). Figure 7.5c shows the age patterns synthesizing the variations of evapotranspiration, atmospheric transport conditions, and precipitating events for the whole year 2005. Overall, the age has a negative correlation with the tagged precipitation: Most of the low age ($\leq$ 3 hours) are found in regions where relatively large amounts of the tagged precipitation ($\geq$ 8 mm) occur, for example, in the source area S and in the North along the Yangtze River Valley. The reason is, that a large proportion of the annual tagged precipitation in these regions is accounted for by the precipitation occuring in the rainy season and in the summer months (e.g., May in Figure 7.5g and August in Figure 7.5j), with a comparatively faster response of the atmospheric branch of the hydrological cycle. In contrast, significantly decreasing wind speed and rapidly changing wind direction lead to longer atmospheric water pathways of the tagged moisture before precipitating, for example in the southeast quadrant. It is worth to note that the age patterns of the tagged precipitation over the land surface (Figure 7.5c) is very similar to the age patterns of the condensed tagged moisture in the atmosphere, but being around one hour shorter (Figure 7.4f). This time lag is probably ascribed to a longer life of the non-precipitating and later re-evaporating condensed tagged moisture.

Furthermore, the three selected months clearly reveal the impact of the different monsoon-controlled precipitation regimes on the monthly variations of the age-weighted tagged precipitation patterns and of the corresponding age patterns. In February, the prevailing northwesterly winds generate a band-like structure of the age-weighted tagged precipitation P_{age} (Figure 7.5e). The maximum values of P_{age} are located in the adjacent parts to the East and to the Southeast of the source area. The tagged precipitation P_{tag} with large values generally has a lower age T_P, while comparatively high (around 8 hours) age is found for relatively low values of P_{tag} (around 0.4 mm)

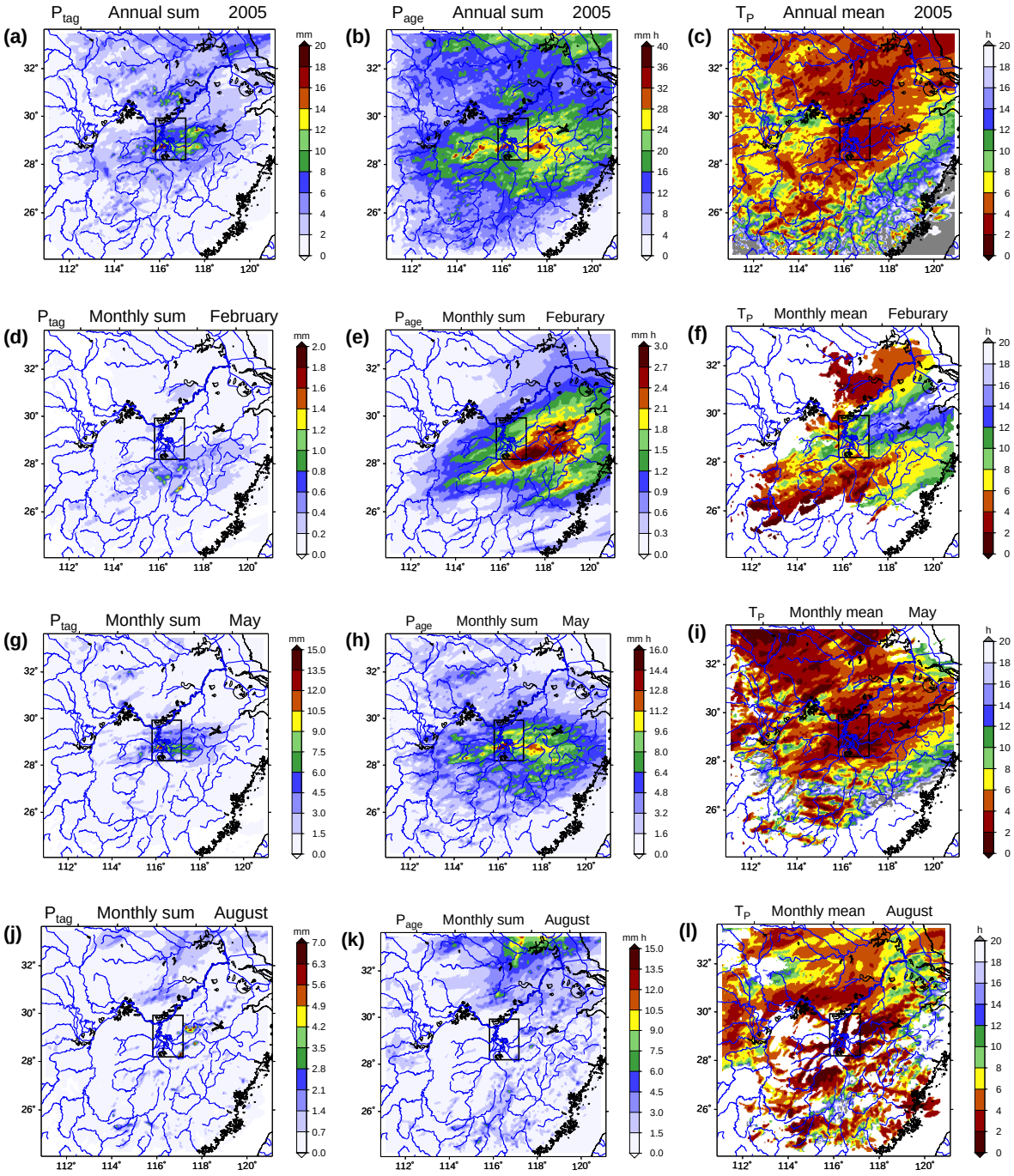

Figure 7.5: Sum of simulated tagged precipitation P_{tag} in mm (left column), age-weighted tagged precipitation P_{age} in mm h (middle column), and age T_P in h (right column) for the total year 2005 and for three selected months (February, May, August).

(see Figures 7.5d and 7.5f). Regions with both significantly high age (> 12 hours) and very small amount of the tagged precipitation (< 0.2 mm) are found in the East of the source area S, probably due to the repeated changes in wind direction. In the rainy season, like in May, the age-weighted tagged precipitation (Figure 7.5h) has higher values than in February (see Figure 7.5e) and the patterns are generally similar to the patterns of the tagged precipitation (Figure 7.5g), with maximum values in the source area S and its surrounding regions. Correspondingly, the age in these regions shown in Figure 7.5i is low (< 5 hours), since large amounts of the tagged moisture is involved in fast, large-scale precipitation processes (see Figure 7.3). A low age of the tagged precipitation are also found in the Northeast and in the South, where the tagged moisture originating from the source area S is transported by strong winds, and then precipitates in accordance with locally convective events. In August, some large values of the tagged precipitation P_{tag} (Figure 7.5g) and of the age-weighted tagged precipitation P_{age} (Figure 7.5h) are found in various regions in and around the source area S. However, regions with maximum age-weighted tagged precipitation (> 10 mm h) are in the remote North (Figure 7.5h) with a long time residing in the atmosphere (Figure 7.5l) due to the decreasing strength of the summer monsoon and the changing wind directions associated with the retreat of the monsoon. Overall, Figure 7.5 depicts the different patterns of the tagged precipitation and the accompanying age, which reveals the varying conditions and dynamical complexity of the atmospheric branch of the hydrological cycle.

7.2.4 Residence Times Corresponding to Partitioned Transpiration and Evaporation

In the context of ET-Tagging partitioning (see Chapter 3.3), the atmospheric residence times of the transpired water and the direct evaporated water can be separately calculated in two long-term simulations (RunAgeE_t and RunAgeE_d) and are presented here. Figures 7.6a and 7.6b shows the vertical profiles of the annual mean of the total tagged moisture mixing ratio and its mean age for evapotranspiration ET and for its partitions E_d and E_t for 2005. Overall, the values of the total tagged moisture decreases with increasing height and reaching values near zero above the planetary boundary layer (Figure 7.6a). In all layers, the contribution by direct evaporation dominates. Regarding the mean age (Figure 7.6b), both, the total tagged moisture for transpiration and direct evaporation resides short in the lower part and longer in the upper part of the atmosphere. Below around 950 hPa (7^{th} sigma level), the age for direct evaporation is lower than that for transpiration. The reason is probably that a large amount of direct evaporated moisture originates during the daytime frequently coinciding with convection. Instead, the transpired moisture originates more continuously and shows higher mean age, especially contributed by the long residence times of water transpired

during the nighttime. In contrast, an inversed difference in the profiles of the mean age for transpiration (younger) and direct evaporation (older) is found in the upper part of the atmosphere (above the 7^{th} sigma level). This inversion is presumably ascribed to the transpired water uptake from the wet root zone contrasting to less direct evaporated water from the dry top soil, especially during the dry season. This explanation is generally supported by van der Ent (2014). Overall, these differences reflect the different features of the respective processes: intermittent direct evaporation, more continuous transpiration, and rising and mixing of the two partitions.

Figures 7.6c and 7.6d show the same as Figures 7.6a and 7.6b but for the condensed tagged moisture. Two peaks of the condensed tagged moisture mixing ratio for the two ET partitions are found (Figure 7.6c), which indicates the overall meteorological conditions relating to the atmospheric circulations over Southeast China. One peak is found around 913 hPa (10^{th} sigma level), presumably due to the mean stratification, mainly in winter. Another peak around 590 hPa (20^{th} sigma level) may be caused by the lifting convection dominating in summer. In all layers, the condensed tagged moisture qd_{tag} is mainly contributed by the younger direct evaporation. The mean age of qd_{tag} for direct evaporation in the lower part of the atmosphere is lower than in the upper part, which is inversed for transpiration (Figure 7.6d). This reveals that the direct evaporated water favors the formation of clouds and precipitation more in the lower part of the atmosphere, while the transpired moisture condenses relatively more and later in the upper part. By comparison the mean age of qd_{tag} for the two ET partitions, the atmosphere has a quick response to the direct evaporation process and a slower response to the transpiration process.

Horizontally, the pattern of the tagged moisture originating from direct evaporation Qt_{tag,E_d} (Figure 7.7a) follows the pattern of the total tagged moisture from evapotranspiration Qt_{tag} (see Figure 7.4a). Averaged over area C, Qt_{tag,E_d} accounts for 64 % of Qt_{tag}. The age pattern of Qt_{tag,E_d} (Figure 7.7b) is similar to the age pattern of Qt_{tag} (Figure 7.4c). Compared with the Qt_{tag,E_d} pattern, the pattern for the transpiration contribution is shifted slightly bit towards the North (Figure 7.7c). Especially, over the southwestern part of area C the atmosphere contains younger (around 40 hours) tagged moisture contributed by direct evaporation and slightly older (around 50 hours) moisture by transpiration. Such a difference is also found in the southeast quadrant, while over the northern and western parts, the mean age for direct evaporation and for transpiration shows similar values. Averaged over area C, the mean age of Qt_{tag,E_d} and Qt_{tag,E_t} are nearly equal to the value for evapotranspiration τ_{Qt}, i.e., around 36 hours.

Regarding the condensed tagged moisture Qd_{tag}, 69.2 % is contributed by direct evaporation and the rest by transpiration. The area-averaged age of Qt_{tag,E_d} (around 7 hours) is lower than that of Qt_{tag,E_t} (around 11 hours). A large amount of the condensed tagged moisture Qd_{tag,E_d} originating from direct evaporated water is found in

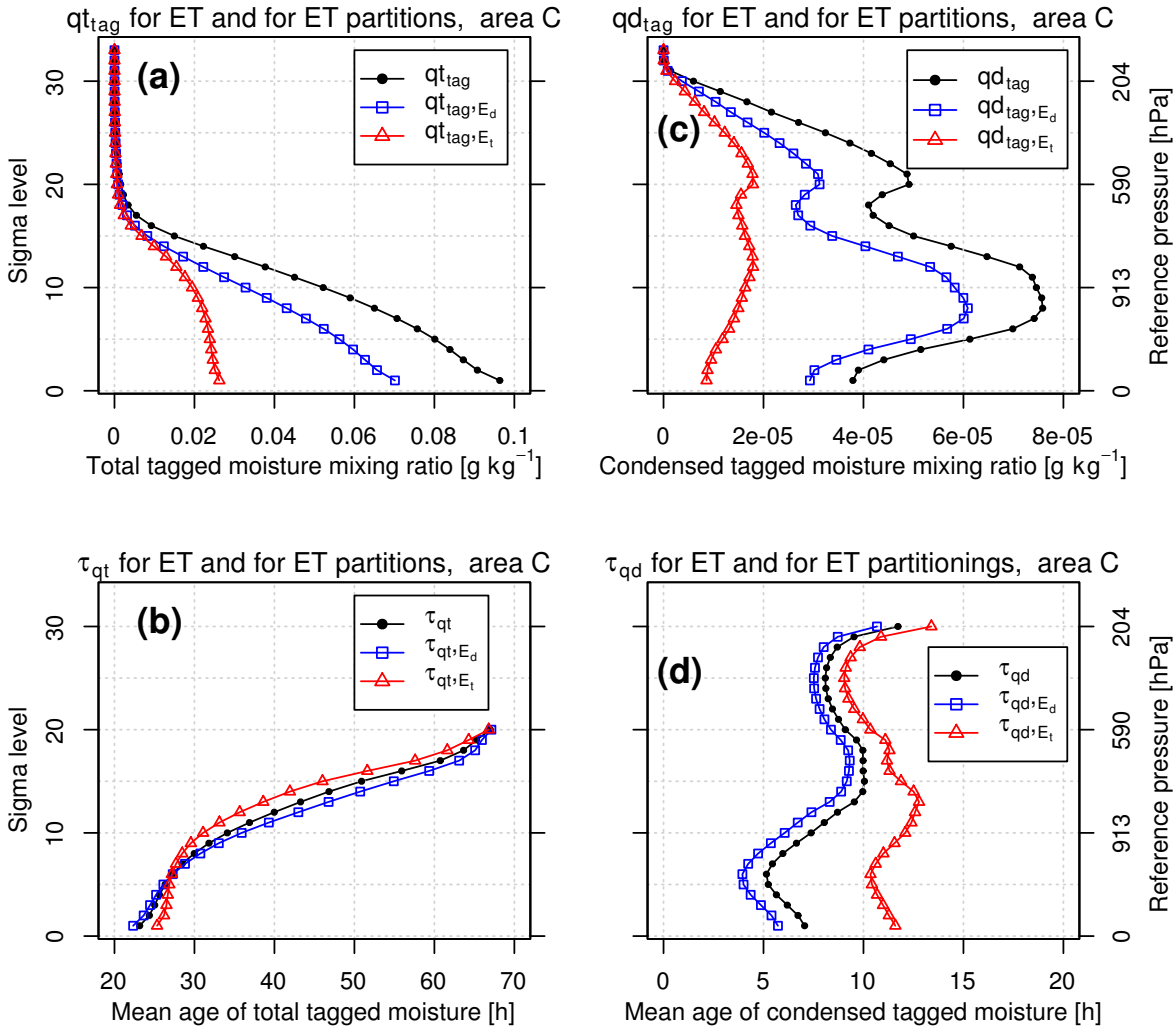

Figure 7.6: Vertical distribution of annual mean of (a) total tagged moisture mixing ratio qt_{tag} in g kg^{-1}, (b) mean age of total tagged moisture mixing ratio τ_{qt} in h, originating from evapotranspired water (in black), from direct evaporated water (in blue), and from transpired water (in red), averaged over area C for the year 2005. Right column shows the same as the left column but for condensed tagged moisture.

the atmosphere over the source area S and in the adjacent part to the East and in the South (Figure 7.7e), with an age of more than 6 hours (Figure 7.7f). In contrast, transpired water is more important over the region close to the source area S and in the North (Figure 7.7g), with an age of less than 6 hours (Figure 7.7h). In comparison, in the South, the direct evaporated water contributes nearly to all the condensed tagged moisture with low age (< 8 hours), whereas the transpired water contributes little with higher age (> 12 hours). In the North, the two ET partitions contribute nearly equally with similar age (only ≤ 2 hours lag between the direct evaporated precipitation and the transpired precipitation).

In order to investigate the monthly variation of the atmospheric water residence times over area C, time series of monthly mean of moisture content (upper row) and of age (lower row) for the year 2005 are displayed in Figure 7.8. The tagged moisture Qt_{tag,E_d} due to direct evaporation (Figure 7.8a) significantly increases from January to March, reaches its maximum during the months from April to June, and becomes relatively low (around 60 g m^{-2}) in the following months. In contrast, the tagged moisture Qt_{tag,E_t} due to transpiration has low values in winter and reaches its maximum values in June and September. This reveals that, in the summer season, the transpiration turns more important for the formation of tagged moisture and also for the formation of tagged precipitation. Considering the mean age (Figure 7.8b), generally, there is a systematic difference between in the ages of Qt_{tag,E_d} and of Qt_{tag,E_t}. In particular, the age of Qt_{tag,E_t} reaches nearly the same value as that of Qt_{tag,E_d} during the period from July to September, which is likely due to the stronger effect of the transpired water uptake by vegetation.

In comparison with the absolute of the total tagged moisture, the condensed amount for the two partitions (Qd_{tag,E_d} and Qd_{tag,E_t}) is nearly two orders of magnitude lower (Figure 7.8c). Generally, the monthly variation of Qd_{tag,E_d} is similar to the variation of Qd_{tag,E_t}. But, the respective maximum values are found in different months: in May for Qd_{tag,E_d}, and in June and August for Qd_{tag,E_t}. Correspondingly, the monthly variation of the age of Qd_{tag,E_d} is larger (from 7 hours in July to 25 hours in November) compared with that of Qd_{tag,E_d} (from 5 to 10 hours) (Figure 7.8d). The mean age of Qd_{tag,E_d} is lower than that of Qt_{tag,E_t}, especially in the cold season, with the difference of around 15 hours, since the direct evaporation dominates the formation of the condensed moisture during this period. This difference becomes small in the transient season and even nearly no difference during the warm months from June to August. It indicates that the transpired and direct evaporated water nearly have the same probability to be involved in forming clouds and tagged precipitation.

Figure 7.9 (left column) shows the horizontal distribution of the tagged precipitation contributed by the two ET partitions, accumulated for the year 2005. The annual mean of the corresponding age is shown in Figure 7.9 (right column). Generally, the

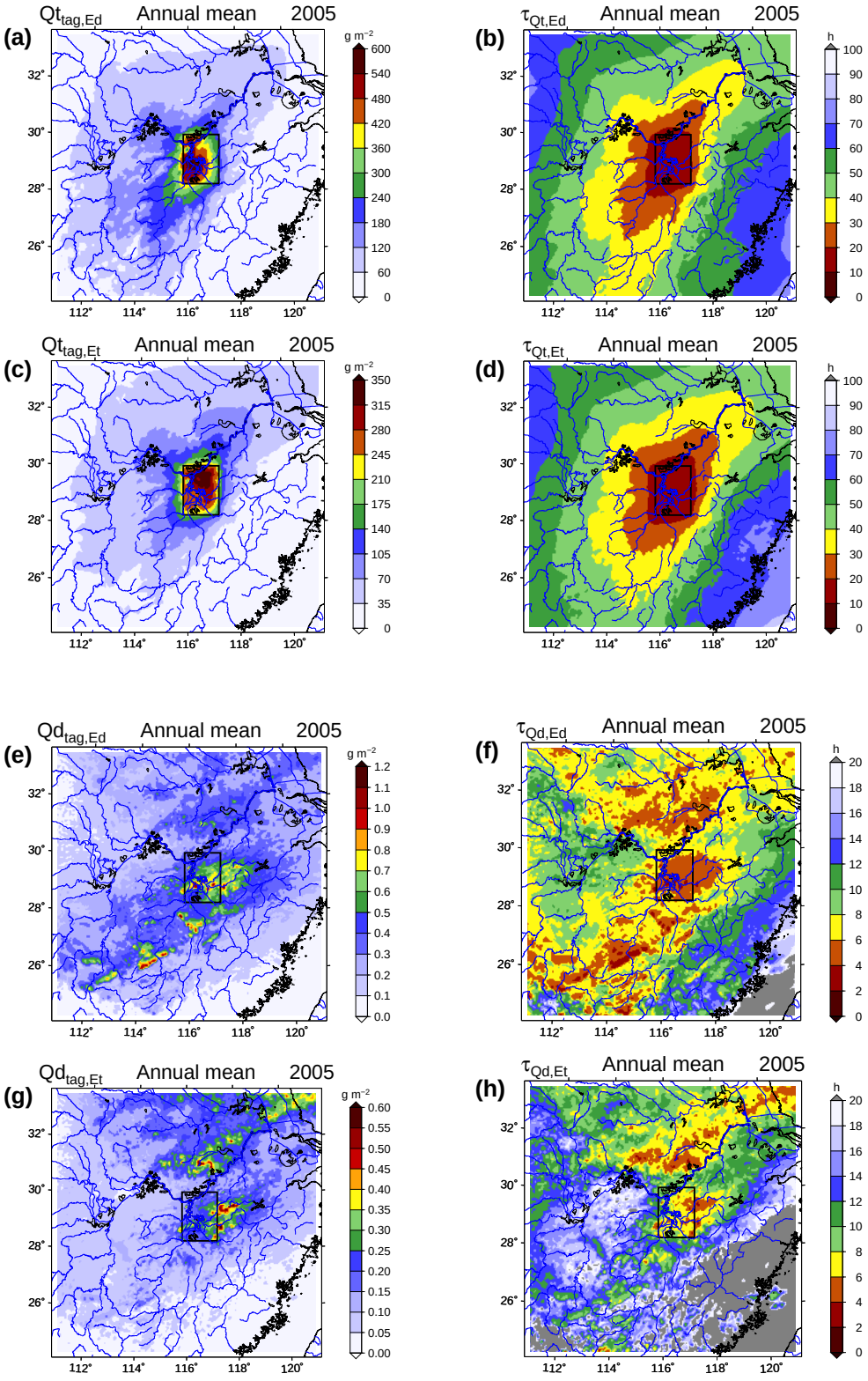

Figure 7.7: Annual mean of simulated column-integrated (a) total tagged moisture originating from direct evaporated water Qt_{tag,E_d} in g m^{-2} and (b) age τ_{Q_t,E_d} of total tagged moisture for direct evaporation in h, averaged for the year 2005. The second row (c,d) shows the same as the first row but for tagged moisture from transpiration. (e) Annual mean of condensed tagged moisture from direct evaporation Qd_{tag,E_d} in g m^{-2} and (f) corresponding age τ_{Q_d,E_d} in h. The fourth row (g, h) shows the same as the third row but for transpiration.

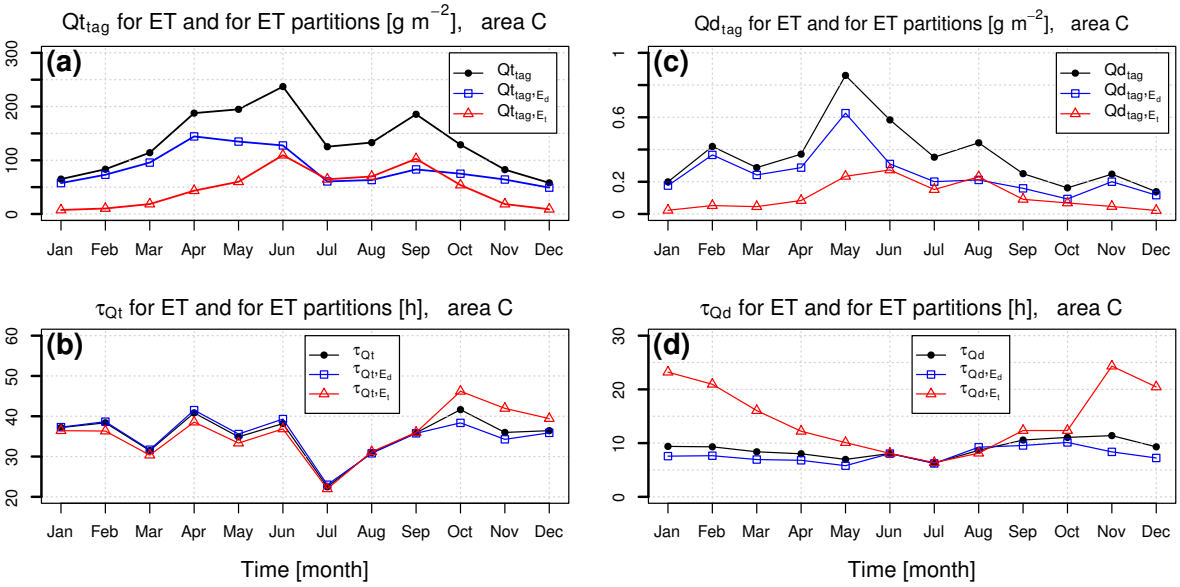

Figure 7.8: Time series of monthly mean of column integrated (a) total tagged moisture Qt_{tag} in g m^{-2} and (b) age τ_{Qt} of total tagged moisture in h, originating from evapotranspired water (in black), from direct evaporated water (in blue), and from transpired water (in red), each averaged over area C. Right panel shows the same as the left panel but for condensed tagged moisture.

patterns of the partitioned tagged precipitation (their age) are similar to the patterns of the partitioned condensed tagged moisture (their age) (see Figure 7.7e-h). The direct evaporation contributes more to the total tagged precipitation with a lower age (area mean: 6.6 hours) than the transpiration (area mean: 10.7 hours). Over the regions around the source area and in the North, the ages of the two partitioned tagged precipitation are similarly short ($<$ 6 hours). However, in the West and in the South, the tagged precipitation by transpiration has much higher age than that by direct evaporation.

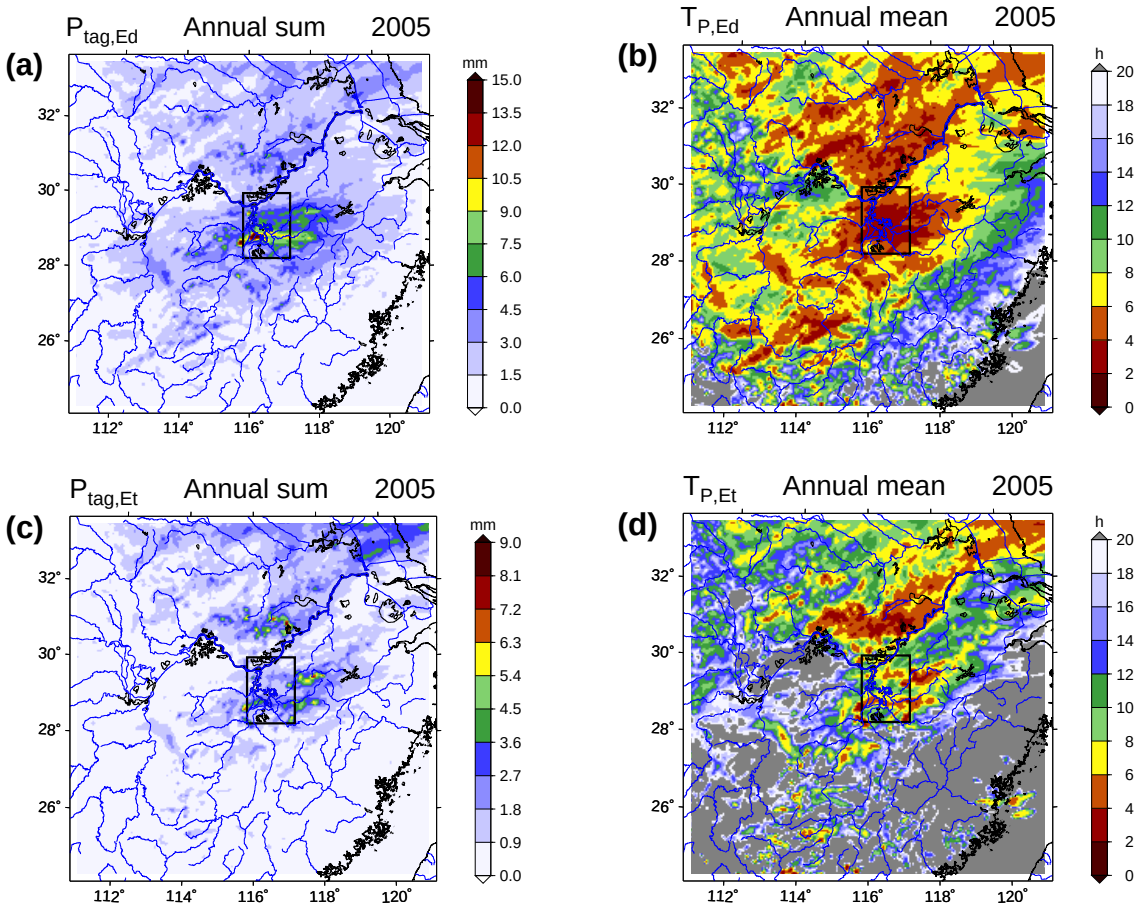

Figure 7.9: (a) Annual sum of simulated tagged precipitation originating from direct evaporation P_{tag,E_d} in mm and (b) corresponding mean age T_{P,E_d} in h, for the year 2005. Lower panel (c,d) shows the same as the upper panel but for transpiration.

Chapter 8

Summary, Conclusions, and Perspectives

A regional climate model with an ET-Tagging algorithm was applied to the Poyang Lake region (Southeast China) for 2005. This method, accounting for all water transport and phase transitions, allows to tag the evapotranspired water from a given source area and to follow the pathways across the atmosphere until the tagged moisture returns to the land surface as precipitation or leaves the model domain. This model has been extended to track transpiration and direct evaporation separately and has been extended again by including an age-weighting mechanism to calculate the atmospheric water residence time, correspondingly. It was used to explicitly quantify the contribution of regional evapotranspiration to precipitation, and to further evaluate the effect of land-surface characteristics on hydrological processes by partitioning total evapotranspiration into direct evaporation and transpiration. Additionally, the age-weighting mechanism, calculating the atmospheric residence times of the direct evaporated and transpired water, allows to assess the response, here the celerity, of the atmospheric branch of the hydrological cycle.

The study reveals that the location and magnitude of the tagged precipitation show large spatial and temporal variability controlled by synoptic weather conditions, especially by the wind shear due to the advance and retreat of the East Asian monsoon. Most tagged precipitation falls around the Poyang Lake region. In 2005, the tagged precipitation contribution accounts for up to 1.2 % of the total rainfall. On a monthly scale, the maximum value of the contribution ratio is found in August ($\leq 6\,\%$). This relative low contribution of evapotranspiration from the Poyang Lake region to the precipitation in Southeast China means that the precipitation mainly originates from non-local moisture. This result is generally in line with previous studies by Numaguti (1999); Yoshimura et al. (2004a); van der Ent and Savenije (2011). In summer, non-

local moisture contributions are mainly from the ocean, transported by the East Asian monsoon (Wu et al., 2006), whereas in winter, it mainly comes from the North (Chow et al., 2008). Maximum values of tagged precipitation contribution ratios are consistently found in May, which reveals that the contribution of the Poyang Lake region becomes significant in accordance with peak total precipitation occuring.

Regarding the impact of vegetation cover and land-use, in 2005 69 % of the tagged precipitation in Southeast China is contributed by direct evaporation from the Poyang Lake region, and 31 % by vegetation transpiration. The annual cycle of these fractions reflects the changes of meteorological conditions and vegetation growth. In winter, the fraction of precipitation from transpiration accounts for only around 10 % of the total tagged precipitation, while it reaches values of up to 50 % for the remainder of the year.

Seasonal varying values of the source-specific precipitation efficiencies reveal a different response of the atmospheric hydrological cycle: warmer air temperature, increased convection, and large-scale lifting enhance the response of the atmospheric hydrological cycle to the direct evaporation from the Poyang Lake region, resulting in maximum values of the source-specific precipitation efficiencies in the rainy season. In May, the precipitation formation is more efficient for moisture originating from direct evaporation. While in the comparatively dry month August, the efficiency for transpiration dominates in the source area since a large amount of water from the lower moist soil is transferred by vegetation, with little evaporative flux from the upper dry soil.

With regard to the atmospheric water residence times, the study shows the formation and evolution of the tagged and age-weighted tagged moisture fields and depicts the evolution of the corresponding lifetimes. The spatial and temporal variations of the mean age of the tagged moisture are controlled by the magnitudes of the newly tagged evapotranspired water compared to the magnitudes of the already existing age-weighted tagged moisture and by changes in the atmospheric transport conditions.

Our results reveal that the celerity of the atmospheric branch of the hydrological cycle changes over the months. The atmospheric total tagged moisture originating from the Poyang Lake region has a comparatively long residence time in winter and a shorter time in summer. Spatially, the age of the total tagged moisture increases with the length of the moisture pathways, resulting in most cases in an increasing distance to the Poyang Lake region, too. The horizontal and vertical patterns reflect differently prevailing wind directions and speeds in the winter and summer monsoon controlled seasons.

Regarding the cloud and precipitation formation, the age of the condensed tagged moisture, i.e., around 8 hours averaged over area C (nearly Southeast China), is much shorter in comparison with that of the total tagged moisture (around 36 hours). Most

of the condensed tagged moisture with short residence times is found in winter in the lower part of the atmosphere and in summer in the higher layers of the atmosphere, which reflects the different precipitation regimes in Southeast China. In comparison, the mean age patterns of the tagged precipitation over the land surface is very similar to the mean age patterns of the condensed tagged moisture in the atmosphere, but being around one hour shorter. A longer life of the non-precipitating and later re-evaporating condensed moisture presumably accounts for this time lag. As well, the tagged precipitation has different age patterns from month to month, which reveals the varying conditions impacted by the East Asian monsoon and the dynamical complexity of the atmospheric branch of the hydrological cycle.

In the context of the ET-Tagging partitioning, in 2005 the age of the tagged moisture for direct evaporation is lower than that for transpiration in the lower part of the atmosphere and the inversed case is found in higher layers. This phenomenon reflects different features of respective process over the land surface: intermittent direct evaporation, more continuous transpiration, and mixing of the two ET partitions. Horizontally, over the southwestern part of area C and in the southeast quadrant, the atmosphere contains the "fresh" (around 40 hours) tagged moisture contributed by direct evaporation and "older" (around 50 hours) by transpiration. Over the northern and western parts, the age for the two ET partitions reaches the similar values. On the monthly scale, there is no significant difference between the age of the tagged moisture for the two ET partitions. However, the condensed tagged moisture for transpiration has always higher age than that for direct evaporation in all vertical layers of the atmosphere. A large amount of the condensed tagged moisture by direct evaporation with lower age is found in the South, while two ET partitions play nearly the same role in forming the cloud and precipitation in the North. Monthly, the age of the condensed tagged moisture due to direct evaporation is lower than the age due to transpiration, especially in the cold season. This age difference becomes smaller in the transient season and even no difference during the warm months from June to August.

Overall, in 2005 the direct evaporated water accounts for 64% of the total tagged moisture and the transpired water for 36% with a mean age of 36 hours for both. Regarding the condensed tagged moisture, 69.2% originates from the direct evaporated water and 30.8% from the transpired water, with a mean age of 7 hours and 11 hours, respectively. Similarly, the tagged precipitation consists of a large proportion (69%) of direct evaporated water with comparatively short atmospheric residence times (area mean: 6.6 hours) and of a small amount of transpired water with longer atmospheric residence times (area mean: 10.7 hours).

However, it is important to note that there are several limitations to the method used here: The results depend on how well physical processes like evapotranspiration, evapotranspiration partitioning, and precipitation are represented in the respective

model system (here: MM5). Moreover, this study did not account for the impact of human activities, like irrigation of paddy rice in the Poyang Lake region.

This study is based on a one year simulation, because the focus is on the introduction and evaluation of methods to distinguish between direct evaporation and transpiration and to calculate the corresponding atmospheric water residence times within the evapotranspiration tagging approach. It has been shown that the partitioning has a clear intra-annual/seasonal variability in accordance with the general monsoon dynamics of the region and the vegetation response. Magnitudes of recycling, partitioning, and residence times may defer from year to year with respect to different atmospheric circulation types (Philipp et al., 2014), but are expected to follow the monsoon controlled partitioning behavior. It is noted that for small tagging areas and accordingly small precipitation recycling ratios (like 1 % mean in this study), uncertainties due to numerical approximations might have more influence on derived values than in cases of larger domains and larger precipitation recycling ratios.

In the future, this proposed high-resolution RCM-based age-weighted evapotranspiration tagging partitioning algorithm should be applied in sensitivity simulations and in further case studies to narrow down uncertainties. Although this study addresses only selected aspects of the complex relationships between land and atmosphere, it emphasizes the important impacts of vegetation cover and land-use on the regional atmospheric hydrological cycle. The results depict the comprehensive interactions between land-surface characteristics as simulated by a mesoscale model (e.g., water bodies, soil, and vegetation) and atmospheric variability such as the seasonal variation of the prevailing meteorological conditions. It is shown that there is a pronounced difference in the spatial and temporal ranges to which and how long transpiration and evaporation are able to contribute to precipitation. Moreover, the information on the timescales for the atmospheric branch of the hydrological cycle, particularly for transpired and evaporated water, has been explicitly quantified by using the age-weighted regional ET-Tagging approach. Following this approach, future research will address how atmospheric water residence times may change as climate changes.

Bibliography

Alexandre, R.-E. and Gonzalo, M.-M. (2013). Moisture recycling and the maximum of precipitation in spring in the Iberian Peninsula. *Climate Dynamics*, pages 1–25.

Allen, M. R. and Ingram, W. J. (2002). Constraints on future changes in climate and the hydrologic cycle. *Nature*, 419(6903):224–232.

Arakawa, A. (2004). The Cumulus Parameterization Problem: Past, Present, and Future. *J. Climate*, 17(13):2493–2525.

Bagley, J. E., Desai, A. R., Dirmeyer, P. A., and Foley, J. A. (2012). Effects of land cover change on moisture availability and potential crop yield in the world's breadbaskets. *Environmental Research Letters*, 7.

Baldocchi, D., Falge, E., Gu, L., Olson, R., Hollinger, D., Running, S., Anthoni, P., Bernhofer, C., Davis, K., Evans, R., Fuentes, J., Goldstein, A., Katul, G., Law, B., Lee, X., Malhi, Y., Meyers, T., Munger, W., Oechel, W., Paw, K. T., Pilegaard, K., Schmid, H. P., Valentini, R., Verma, S., Vesala, T., Wilson, K., and Wofsy, S. (2001). FLUXNET: A New Tool to Study the Temporal and Spatial Variability of Ecosystem-Scale Carbon Dioxide, Water Vapor, and Energy Flux Densities. *Bull. Amer. Meteor. Soc.*, 82(11):2415–2434.

Bolin, B. and Rodhe, H. (1973). A note on the concepts of age distribution and transit time in natural reservoirs. *Tellus*, 25(1):58–62.

Bosilovich, M. G. and Chern, J.-D. (2006). Simulation of Water Sources and Precipitation Recycling for the MacKenzie, Mississippi, and Amazon River Basins. *J. Hydrometeor*, 7(3):312–329.

Bosilovich, M. G. and Schubert, S. D. (2001). Precipitation Recycling over the Central United States Diagnosed from the GEOS-1 Data Assimilation System. *J. Hydrometeor*, 2(1):26–35.

Bosilovich, M. G. and Schubert, S. D. (2002). Water Vapor Tracers as Diagnostics of the Regional Hydrologic Cycle. *J. Hydrometeor*, 3(2):149–165.

Bosilovich, M. G., Schubert, S. D., and Walker, G. K. (2005). Global Changes of the Water Cycle Intensity. *J. Climate*, 18(10):1591–1608.

Bosilovich, M. G., Sud, Y. C., Schubert, S. D., and Walker, G. K. (2003). Numerical simulation of the large-scale North American monsoon water sources. *Journal of Geophysical Research: Atmospheres*, 108(D16):n/a–n/a.

Brohan, P., Kennedy, J. J., Harris, I., Tett, S. F. B., and Jones, P. D. (2006). Uncertainty estimates in regional and global observed temperature changes: A new data set from 1850. *Journal of Geophysical Research: Atmospheres*, 111(D12):n/a–n/a.

Brubaker, K. L., Entekhabi, D., and Eagleson, P. S. (1993). Estimation of Continental Precipitation Recycling. *J. Climate*, 6(6):1077–1089.

Brutsaert, W. and Parlange, M. B. (1998). Hydrologic cycle explains the evaporation paradox. *Nature*, 396(6706):30–30.

Budyko, M. (1974). *Climate and Life*, volume 18. Academic Press, INC, New York.

Burde, G. I. and Zangvil, A. (2001). The Estimation of Regional Precipitation Recycling. Part I: Review of Recycling Models. *J. Climate*, 14(12):2497–2508.

Burde, G. I., Zangvil, A., and Lamb, P. J. (1996). Estimating the Role of Local Evaporation in Precipitation for a Two-Dimensional Region. *J. Climate*, 9(6):1328–1338.

Chen, F. and Dudhia, J. (2001). Coupling an Advanced Land Surface-Hydrology Model with the Penn State-NCAR MM5 Modeling System. Part I: Model Implementation and Sensitivity. *Mon. Wea. Rev.*, 129(4):569–585.

Chen, F., Mitchell, K., Schaake, J., Xue, Y., Pan, H.-L., Koren, V., Duan, Q. Y., Ek, M., and Betts, A. (1996). Modeling of land surface evaporation by four schemes and comparison with FIFE observations. *J. Geophys. Res.*, 101(D3):7251–7268.

Chow, K., Tong, H.-W., and Chan, J. (2008). Water vapor sources associated with the early summer precipitation over China. *Climate Dynamics*, 30(5):497–517.

Coenders-Gerrits, A. M. J., van der Ent, R. J., Bogaard, T. A., Wang-Erlandsson, L., Hrachowitz, M., and Savenije, H. H. G. (2014). Uncertainties in transpiration estimates. *Nature*, 506(7487):E1–E2.

Dai, A., Genio, A. D. D., and Fung, I. Y. (1997). Clouds, precipitation and temperature range. *Nature*, 386(6626):665–666.

de Ela, R., Laprise, R., and Denis, B. (2002). Forecasting Skill Limits of Nested, Limited-Area Models: A Perfect-Model Approach. *Mon. Wea. Rev.*, 130(8):2006–2023.

Dee, D. P., Uppala, S. M., Simmons, A. J., Berrisford, P., Poli, P., Kobayashi, S., Andrae, U., Balmaseda, M. A., Balsamo, G., Bauer, P., Bechtold, P., Beljaars, A. C. M., van de Berg, L., Bidlot, J., Bormann, N., Delsol, C., Dragani, R., Fuentes, M., Geer, A. J., Haimberger, L., Healy, S. B., Hersbach, H., Hólm, E. V., Isaksen, L., Kållberg, P., Köhler, M., Matricardi, M., McNally, A. P., Monge-Sanz, B. M., Morcrette, J.-J., Park, B.-K., Peubey, C., de Rosnay, P., Tavolato, C., Thépaut, J.-N., and Vitart, F. (2011). The ERA-Interim reanalysis: configuration and performance of the data assimilation system. *Quarterly Journal of the Royal Meteorological Society*, 137(656):553–597.

Deng, X., Zhao, Y., Wu, F., Lin, Y., Lu, Q., and Dai, J. (2011). Analysis of the trade-off between economic growth and the reduction of nitrogen and phosphorus emissions in the Poyang Lake Watershed, China. *Ecological Modelling*, 222(2):330 – 336. Wetlands in China.

Denis, B., Laprise, R., and Caya, D. (2003). Sensitivity of a regional climate model to the resolution of the lateral boundary conditions. *Climate Dynamics*, 20(2-3):107–126.

Ding, Y. and Chan, J. C. L. (2005). The East Asian summer monsoon: an overview. *Meteorology and Atmospheric Physics*, 89(1-4):117–142.

Dirmeyer, P. A. and Brubaker, K. L. (1999). Contrasting evaporative moisture sources during the drought of 1988 and the flood of 1993. *Journal of Geophysical Research: Atmospheres*, 104(D16):19383–19397.

Dirmeyer, P. A. and Brubaker, K. L. (2007). Characterization of the Global Hydrologic Cycle from a Back-Trajectory Analysis of Atmospheric Water Vapor. *J. Hydrometeor*, 8(1):20–37.

Dominguez, F., Kumar, P., Liang, X.-Z., and Ting, M. (2006). Impact of Atmospheric Moisture Storage on Precipitation Recycling. *J. Climate*, 19(8):1513–1530.

Done, J., Davis, C. A., and Weisman, M. (2004). The next generation of NWP: explicit forecasts of convection using the weather research and forecasting (WRF) model. *Atmospheric Science Letters*, 5(6):110–117.

Draxler, R. R. (2003). Evaluation of an Ensemble Dispersion Calculation. *J. Appl. Meteor.*, 42(2):308–317.

Druyan, L. M. and Koster, R. D. (1989). Sources of Sahel Precipitation for Simulated Drought and Rainy Seasons. *J. Climate*, 2(12):1438–1446.

Dudhia, J. (1989). Numerical Study of Convection Observed during the Winter Monsoon Experiment Using a Mesoscale Two-Dimensional Model. *J. Atmos. Sci.*, 46(20):3077–3107.

Dudhia, J. (1993). A Nonhydrostatic Version of the Penn State-NCAR Mesoscale Model: Validation Tests and Simulation of an Atlantic Cyclone and Cold Front. *Mon. Wea. Rev.*, 121(5):1493–1513.

Dudhia, J. (2014). A history of mesoscale model development. *Asia-Pacific Journal of Atmospheric Sciences*, 50(1):121–131.

Durre, I., Vose, R. S., and Wuertz, D. B. (2006). Overview of the Integrated Global Radiosonde Archive. *J. Climate*, 19(1):53–68.

Durre, I., Vose, R. S., and Wuertz, D. B. (2008). Robust Automated Quality Assurance of Radiosonde Temperatures. *J. Appl. Meteor. Climatol.*, 47(8):2081–2095.

Easterling, D. R., Horton, B., Jones, P. D., Peterson, T. C., Karl, T. R., Parker, D. E., Salinger, M. J., Razuvayev, V., Plummer, N., Jamason, P., and Folland, C. K. (1997). Maximum and Minimum Temperature Trends for the Globe. *Science*, 277(5324):364–367.

Ek, M. B., Mitchell, K. E., Lin, Y., Rogers, E., Grunmann, P., Koren, V., Gayno, G., and Tarpley, J. D. (2003). Implementation of Noah land surface model advances in the National Centers for Environmental Prediction operational mesoscale Eta model. *Journal of Geophysical Research: Atmospheres*, 108(D22):n/a–n/a.

Eltahir, E. A. B. and Bras, R. L. (1994). Precipitation recycling in the Amazon basin. *Quarterly Journal of the Royal Meteorological Society*, 120(518):861–880.

Eltahir, E. A. B. and Bras, R. L. (1996). Precipitation recycling. *Reviews of Geophysics*, 34(3):367–378.

Entekhabi, D., Rodriguez-Iturbe, I., and Bras, R. L. (1992). Variability in Large-Scale Water Balance with Land Surface-Atmosphere Interaction. *J. Climate*, 5(8):798–813.

Feng, L., Hu, C., Chen, X., Cai, X., Tian, L., and Gan, W. (2012). Assessment of inundation changes of Poyang Lake using MODIS observations between 2000 and 2010. *Remote Sensing of Environment*, 121(0):80 – 92.

Fersch, B. and Kunstmann, H. (2013). Atmospheric and terrestrial water budgets: sensitivity and performance of configurations and global driving data for long term continental scale WRF simulations. *Climate Dynamics*, pages 1–30.

Gao, B., Yang, D., and Yang, H. (2013). Impact of the Three Gorges Dam on flow regime in the middle and lower Yangtze River. *Quaternary International*, 304(0):43 – 50. Larger Asian Rivers: Changes in hydro-climate and water environments.

Gao, G., Chen, D., Xu, C.-y., and Simelton, E. (2007). Trend of estimated actual evapotranspiration over China during 1960-2002. *Journal of Geophysical Research: Atmospheres*, 112(D11):n/a–n/a.

Gemmer, M., Becker, S., and Jiang, T. (2004). Observed monthly precipitation trends in China 1951-2002. *Theoretical and Applied Climatology*, 77(1-2):39–45.

Gimeno, L., Stohl, A., Trigo, R. M., Dominguez, F., Yoshimura, K., Yu, L., Drumond, A., DurÃ¡n-Quesada, A. M., and Nieto, R. (2012). Oceanic and terrestrial sources of continental precipitation. *Reviews of Geophysics*, 50(4):n/a–n/a.

Goessling, H. F. and Reick, C. H. (2011). What do moisture recycling estimates tell us? Exploring the extreme case of non-evaporating continents. *Hydrology and Earth System Sciences*, 15(10):3217–3235.

Goessling, H. F. and Reick, C. H. (2013). On the "well-mixed" assumption and numerical 2-D tracing of atmospheric moisture. *Atmospheric Chemistry and Physics*, 13(11):5567–5585.

Gomez, J. D. and Wilson, J. L. (2013). Age distributions and dynamically changing hydrologic systems: Exploring topography-driven flow. *Water Resources Research*, 49(3):1503–1522.

Gonzalo, M., L., S. G., and Alan, R. (2004). Spectral nudging to eliminate the effects of domain position and geometry in regional climate model simulations. *Journal of Geophysical Research: Atmospheres*, 109(D13):n/a–n/a.

Grell, G., Dudhia, J., and Stauffer, D. (1994). A description of the fifth-generation Penn State/NCAR Mesoscale Model (MM5). Technical report, NCAR Technical Note NCAR/TN-398+STR.

Gustafsson, M., Rayner, D., and Chen, D. (2010). Extreme rainfall events in southern Sweden: where does the moisture come from? *Tellus A*, 62(5):–.

Han, Z., Ueda, H., and An, J. (2008). Evaluation and intercomparison of meteorological predictions by five MM5-PBL parameterizations in combination with three land-surface models. *Atmospheric Environment*, 42(2):233 – 249.

Harman, C. J. and Kim, M. (2014). An efficient tracer test for time-variable transit time distributions in periodic hydrodynamic systems. *Geophysical Research Letters*, 41(5):1567–1575.

Held, I. M. and Soden, B. J. (2006). Robust Responses of the Hydrological Cycle to Global Warming. *J. Climate*, 19(21):5686–5699.

Hirabayashi, Y., Mahendran, R., Koirala, S., Konoshima, L., Yamazaki, D., Watanabe, S., Kim, H., and Kanae, S. (2013). Global flood risk under climate change. *Nature Clim. Change*, 3(9):816–821.

Hong, J., Kim, J., Lee, D., and Lim, J.-H. (2008). Estimation of the storage and advection effects on H2O and CO2 exchanges in a hilly KoFlux forest catchment. *Water Resources Research*, 44(1):n/a–n/a.

Hong, S.-Y. and Pan, H.-L. (1996). Nonlocal Boundary Layer Vertical Diffusion in a Medium-Range Forecast Model. *Mon. Wea. Rev.*, 124(10):2322–2339.

Hrachowitz, M., Savenije, H., Blöschl, G., McDonnell, J., Sivapalan, M., Pomeroy, J., Arheimer, B., Blume, T., Clark, M., Ehret, U., Fenicia, F., Freer, J., Gelfan, A., Gupta, H., Hughes, D., Hut, R., Montanari, A., Pande, S., Tetzlaff, D., Troch, P., Uhlenbrook, S., Wagener, T., Winsemius, H., Woods, R., Zehe, E., and Cudennec, C. (2013). A decade of Predictions in Ungauged Basins (PUB)—a review. *Hydrological Sciences Journal*, 58(6):1198–1255.

Hu, Z., Wen, X., Sun, X., Li, L., Yu, G., Lee, X., and Li, S. (2014). Partitioning of evapotranspiration through oxygen isotopic measurements of water pools and fluxes in a temperate grassland. *Journal of Geophysical Research: Biogeosciences*, pages n/a–n/a.

Huntington, T. G. (2006). Evidence for intensification of the global water cycle: Review and synthesis. *Journal of Hydrology*, 319(1-4):83–95.

Jacobs, C. M. J. and De Bruin, H. A. R. (1992). The Sensitivity of Regional Transpiration to Land-Surface Characteristics: Significance of Feedback. *J. Climate*, 5(7):683–698.

James, P., Stohl, A., Forster, C., Eckhardt, S., Seibert, P., and Frank, A. (2003). A 15-year climatology of stratosphere-troposphere exchange with a Lagrangian particle dispersion model: 1. Methodology and validation. *Journal of Geophysical Research: Atmospheres*, 108(D12):n/a–n/a.

Jasechko, S., Sharp, Z. D., Gibson, J. J., Birks, S. J., Yi, Y., and Fawcett, P. J. (2013). Terrestrial water fluxes dominated by transpiration. *Nature*, 496(7445):347–350.

Jiao, L. (2009). Scientists Line Up Against Dam That Would Alter Protected Wetlands. *Science*, 326(5952):508–509.

Jones, R. G., Murphy, J. M., and Noguer, M. (1995). Simulation of climate change over europe using a nested regional-climate model. I: Assessment of control climate, including sensitivity to location of lateral boundaries. *Quarterly Journal of the Royal Meteorological Society*, 121(526):1413–1449.

Joussaume, S., Sadourny, R., and Jouzel, J. (1984). A general circulation model of water isotope cycles in the atmosphere. *Nature*, 311(5981):24–29.

Joussaume, S., Sadourny, R., and Vignal, C. (1986). Origin of precipitating water in a numerical simulation of the July climate. *Ocean-Air Inter.*, 1:43–56.

Jouzel, J., Froehlich, K., and Schotterer, U. (1997). Deuterium and oxygen-18 in present-day precipitation: data and modelling. *Hydrological Sciences Journal*, 42(5):747–763.

Jouzel, J., Russell, G. L., Suozzo, R. J., Koster, R. D., White, J. W. C., and Broecker, W. S. (1987). Simulations of the HDO and H218O atmospheric cycles using the NASA GISS general circulation model: The seasonal cycle for present-day conditions. *Journal of Geophysical Research: Atmospheres*, 92(D12):14739–14760.

Jung, M., Reichstein, M., and Bondeau, A. (2009). Towards global empirical upscaling of FLUXNET eddy covariance observations: validation of a model tree ensemble approach using a biosphere model. *Biogeosciences*, 6(10):2001–2013.

Jung, M., Reichstein, M., Ciais, P., Seneviratne, S. I., Sheffield, J., Goulden, M. L., Bonan, G., Cescatti, A., Chen, J., de Jeu, R., Dolman, A. J., Eugster, W., Gerten, D., Gianelle, D., Gobron, N., Heinke, J., Kimball, J., Law, B. E., Montagnani, L., Mu, Q., Mueller, B., Oleson, K., Papale, D., Richardson, A. D., Roupsard, O., Running, S., Tomelleri, E., Viovy, N., Weber, U., Williams, C., Wood, E., Zaehle, S., and Zhang, K. (2010). Recent decline in the global land evapotranspiration trend due to limited moisture supply. *Nature*, 467(7318):951–954.

Jung, M., Reichstein, M., Margolis, H. A., Cescatti, A., Richardson, A. D., Arain, M. A., Arneth, A., Bernhofer, C., Bonal, D., Chen, J., Gianelle, D., Gobron, N., Kiely, G., Kutsch, W., Lasslop, G., Law, B. E., Lindroth, A., Merbold, L., Montagnani, L., Moors, E. J., Papale, D., Sottocornola, M., Vaccari, F., and Williams, C. (2011). Global patterns of land-atmosphere fluxes of carbon dioxide, latent heat, and sensible heat derived from eddy covariance, satellite, and meteorological observations. *Journal of Geophysical Research: Biogeosciences*, 116(G3):n/a–n/a.

Karl, T. R. and Trenberth, K. E. (2003). Modern Global Climate Change. *Science*, 302(5651):1719–1723.

Keys, P. W., Barnes, E. A., van der Ent, R. J., and Gordon, L. J. (2014). Variability of moisture recycling using a precipitationshed framework. *Hydrology and Earth System Sciences*, 18(10):3937–3950.

Keys, P. W., van der Ent, R. J., Gordon, L. J., Hoff, H., Nikoli, R., and Savenije, H. H. G. (2012). Analyzing precipitationsheds to understand the vulnerability of rainfall dependent regions. *Biogeosciences*, 9(2):733–746.

Knoche, H. R. and Kunstmann, H. (2013). Tracking atmospheric water pathways by direct evaporation tagging: A case study for West Africa. *Journal of Geophysical Research: Atmospheres*.

Kool, D., Agam, N., Lazarovitch, N., Heitman, J., Sauer, T., and Ben-Gal, A. (2014). A review of approaches for evapotranspiration partitioning. *Agricultural and Forest Meteorology*, 184(0):56 – 70.

Koster, R., Jouzel, J., Suozzo, R., Russell, G., Broecker, W., Rind, D., and Eagleson, P. (1986). Global sources of local precipitation as determined by the Nasa/Giss GCM. *Geophysical Research Letters*, 13(2):121–124.

Kunstmann, H. and Jung, G. (2007). Influence of soil-moisture and land use change on precipitation in the Volta Basin of West Africa. *International Journal of River Basin Management*, 5(1):9–16.

Kurita, N., Numaguti, A., Sugimoto, A., Ichiyanagi, K., and Yoshida, N. (2003). Relationship between the variation of isotopic ratios and the source of summer precipitation in eastern Siberia. *Journal of Geophysical Research: Atmospheres*, 108(D11):n/a–n/a.

Lai, X., Jiang, J., Yang, G., and Lu, X. X. (2014). Should the Three Gorges Dam be blamed for the extremely low water levels in the middle–lower Yangtze River? *Hydrological Processes*, 28(1):150–160.

Laprise, R. (2008). Regional climate modelling. *Journal of Computational Physics*, 227(7):3641–3666.

Lawrence, D. M., Thornton, P. E., Oleson, K. W., and Bonan, G. B. (2007). The Partitioning of Evapotranspiration into Transpiration, Soil Evaporation, and Canopy Evaporation in a GCM: Impacts on Land-Atmosphere Interaction. *J. Hydrometeor*, 8(4):862–880.

Leduc, M. and Laprise, R. (2009). Regional climate model sensitivity to domain size. *Climate Dynamics*, 32(6):833–854.

Lee, W.-J. and Hong, J. (2015). A hybrid dynamic and fuzzy time series model for mid-term power load forecasting. *International Journal of Electrical Power & Energy Systems*, 64(0):1057–1062.

Lin, E., Xu, Y., Wu, S., Ju, H., and Ma, S. (2007). China's National Assessment Report on Climate Change (II): Climate change impacts and adaptation. *Advances in Climate Change Research*, 03(00):6.

Liu, B., Xu, M., Henderson, M., and Gong, W. (2004a). A spatial analysis of pan evaporation trends in China, 1955-2000. *Journal of Geophysical Research: Atmospheres*, 109(D15):n/a–n/a.

Liu, B., Xu, M., Henderson, M., and Qi, Y. (2005). Observed trends of precipitation amount, frequency, and intensity in China, 1960-2000. *Journal of Geophysical Research: Atmospheres*, 110(D8):n/a–n/a.

Liu, B., Xu, M., Henderson, M., Qi, Y., and Li, Y. (2004b). Taking China's Temperature: Daily Range, Warming Trends, and Regional Variations, 1955–2000. *Journal of Climate*, 17(22):4453–4462.

Liu, M. and Tian, H. (2010). China's land cover and land use change from 1700 to 2005: Estimations from high-resolution satellite data and historical archives. *Global Biogeochemical Cycles*, 24(3):n/a–n/a.

Liu, Y., Wu, G., and Zhao, X. (2013). Recent declines in China's largest freshwater lake: trend or regime shift? *Environmental Research Letters*, 8(1):014010.

Lo, M.-H. and Famiglietti, J. S. (2013). Irrigation in California's Central Valley strengthens the southwestern U.S. water cycle. *Geophysical Research Letters*, 40(2):301–306.

McGuire, K. J. and McDonnell, J. J. (2006). A review and evaluation of catchment transit time modeling. *Journal of Hydrology*, 330(3–4):543 – 563.

Menon, S., Hansen, J., Nazarenko, L., and Luo, Y. (2002). Climate Effects of Black Carbon Aerosols in China and India. *Science*, 297(5590):2250–2253.

Milly, P. C. D., Wetherald, R. T., Dunne, K. A., and Delworth, T. L. (2002). Increasing risk of great floods in a changing climate. *Nature*, 415(6871):514–517.

Mlawer, E. J., Taubman, S. J., Brown, P. D., Iacono, M. J., and Clough, S. A. (1997). Radiative transfer for inhomogeneous atmospheres: RRTM, a validated correlated-k model for the longwave. *Journal of Geophysical Research: Atmospheres*, 102(D14):16663–16682.

Mohamed, Y. A., van den Hurk, B. J. J. M., Savenije, H. H. G., and Bastiaanssen, W. G. M. (2005). Hydroclimatology of the Nile: results from a regional climate model. *Hydrology and Earth System Sciences*, 9(3):263–278.

Molinari, J. and Dudek, M. (1992). Parameterization of Convective Precipitation in Mesoscale Numerical Models: A Critical Review. *Mon. Wea. Rev.*, 120(2):326–344.

Niu, G.-Y., Yang, Z.-L., Mitchell, K. E., Chen, F., Ek, M. B., Barlage, M., Kumar, A., Manning, K., Niyogi, D., Rosero, E., Tewari, M., and Xia, Y. (2011). The community Noah land surface model with multiparameterization options (Noah-MP): 1. Model description and evaluation with local-scale measurements. *Journal of Geophysical Research: Atmospheres*, 116(D12):n/a–n/a.

Numaguti, A. (1999). Origin and recycling processes of precipitating water over the Eurasian continent: Experiments using an atmospheric general circulation model. *Journal of Geophysical Research: Atmospheres*, 104(D2):1957–1972.

Ohmura, A. and Wild, M. (2002). Is the Hydrological Cycle Accelerating? *Science*, 298(5597):1345–1346.

Oki, T. and Kanae, S. (2006). Global Hydrological Cycles and World Water Resources. *Science*, 313(5790):1068–1072.

Pan, H.-L. and Mahrt, L. (1987). Interaction between soil hydrology and boundary-layer development. *Boundary-Layer Meteorology*, 38(1-2):185–202.

Peterson, T. C., Golubev, V., and Groisman, P. (1995). Evaporation losing its strength. *Nature*, 377(6551):687–688.

Pfahl, S., Wernli, H., and Yoshimura, K. (2012). The isotopic composition of precipitation from a winter storm – a case study with the limited-area model COSMO$_{iso}$. *Atmospheric Chemistry and Physics*, 12(3):1629–1648.

Philipp, A., Beck, C., Huth, R., and Jacobeit, J. (2014). Development and comparison of circulation type classifications using the COST 733 dataset and software. *International Journal of Climatology*, pages n/a–n/a.

Prein, A., Gobiet, A., Suklitsch, M., Truhetz, H., Awan, N., Keuler, K., and Georgievski, G. (2013). Added value of convection permitting seasonal simulations. *Climate Dynamics*, 41(9-10):2655–2677.

Qian, C., Fu, C., and Wu, Z. (2011). Changes in the Amplitude of the Temperature Annual Cycle in China and Their Implication for Climate Change Research. *J. Climate*, 24(20):5292–5302.

Reisner, J., Rasmussen, R. M., and Bruintjes, R. T. (1998). Explicit forecasting of supercooled liquid water in winter storms using the MM5 mesoscale model. *Quarterly Journal of the Royal Meteorological Society*, 124(548):1071–1107.

Rienecker, M. M., Suarez, M. J., Gelaro, R., Todling, R., Bacmeister, J., Liu, E., Bosilovich, M. G., Schubert, S. D., Takacs, L., Kim, G.-K., Bloom, S., Chen, J., Collins, D., Conaty, A., da Silva, A., Gu, W., Joiner, J., Koster, R. D., Lucchesi, R., Molod, A., Owens, T., Pawson, S., Pegion, P., Redder, C. R., Reichle, R., Robertson, F. R., Ruddick, A. G., Sienkiewicz, M., and Woollen, J. (2011). MERRA: NASA's Modern-Era Retrospective Analysis for Research and Applications. *J. Climate*, 24(14):3624–3648.

Roderick, M. L. and Farquhar, G. D. (2002). The Cause of Decreased Pan Evaporation over the Past 50 Years. *Science*, 298(5597):1410–1411.

Savenije, H. H. (1995). New definitions for moisture recycling and the relationship with land-use changes in the Sahel. *Journal of Hydrology*, 167(1–4):57 – 78.

Schlesinger, W. H. and Jasechko, S. (2014). Transpiration in the global water cycle. *Agricultural and Forest Meteorology*, 189–190(0):115 – 117.

Schär, C., Lüthi, D., Beyerle, U., and Heise, E. (1999). The Soil-Precipitation Feedback: A Process Study with a Regional Climate Model. *J. Climate*, 12(3):722–741.

Seneviratne, S. I., Corti, T., Davin, E. L., Hirschi, M., Jaeger, E. B., Lehner, I., Orlowsky, B., and Teuling, A. J. (2010). Investigating soil moisture–climate interactions in a changing climate: A review. *Earth-Science Reviews*, 99(3–4):125 – 161.

Seneviratne, S. I., Luthi, D., Litschi, M., and Schar, C. (2006). Land-atmosphere coupling and climate change in Europe. *Nature*, 443(7108):205–209.

Seth, A. and Giorgi, F. (1998). The Effects of Domain Choice on Summer Precipitation Simulation and Sensitivity in a Regional Climate Model. *J. Climate*, 11(10):2698–2712.

Seth, A. and Rojas, M. (2003). Simulation and Sensitivity in a Nested Modeling System for South America. Part I: Reanalyses Boundary Forcing. *J. Climate*, 16(15):2437–2453.

Sewall, J. O., Sloan, L. C., Huber, M., and Wing, S. (2000). Climate sensitivity to changes in land surface characteristics. *Global and Planetary Change*, 26(4):445–465.

Shankman, D., Keim, B. D., Nakayama, T., Li, R., Wu, D., and Remington, W. C. (2012). Hydroclimate Analysis of Severe Floods in China's Poyang Lake Region. *Earth Interact.*, 16(14):1–16.

Shankman, D., Keim, B. D., and Song, J. (2006). Flood frequency in China's Poyang Lake region: trends and teleconnections. *International Journal of Climatology*, 26(9):1255–1266.

Sheffield, J., Wood, E. F., and Roderick, M. L. (2012). Little change in global drought over the past 60 years. *Nature*, 491(7424):435–438.

Shen, D. and Varis, O. (2001). Climate Change in China. *AMBIO: A Journal of the Human Environment*, 30(6):381–383.

Simmonds, I., Bi, D., and Hope, P. (1999). Atmospheric Water Vapor Flux and Its Association with Rainfall over China in Summer. *J. Climate*, 12(5):1353–1367.

Sodemann, H. and Stohl, A. (2013). Moisture Origin and Meridional Transport in Atmospheric Rivers and Their Association with Multiple Cyclones*. *Mon. Wea. Rev.*, 141(8):2850–2868.

Sodemann, H., Wernli, H., and Schwierz, C. (2009). Sources of water vapour contributing to the Elbe flood in August 2002 - A tagging study in a mesoscale model. *Quarterly Journal of the Royal Meteorological Society*, 135(638):205–223.

Stidd, C. K. (1967). *Local moisture and precipitation.* Desert Research Institute, University of Nevada. Preprint series. Desert Research Institute, University of Nevada.

Stohl, A., Forster, C., Frank, A., Seibert, P., and Wotawa, G. (2005). Technical note: The Lagrangian particle dispersion model FLEXPART version 6.2. *Atmospheric Chemistry and Physics*, 5(9):2461–2474.

Stohl, A. and James, P. (2004). A Lagrangian Analysis of the Atmospheric Branch of the Global Water Cycle. Part I: Method Description, Validation, and Demonstration for the August 2002 Flooding in Central Europe. *J. Hydrometeor*, 5(4):656–678.

Stohl, A. and James, P. (2005). A Lagrangian Analysis of the Atmospheric Branch of the Global Water Cycle. Part II: Moisture Transports between Earth's Ocean Basins and River Catchments. *J. Hydrometeor*, 6(6):961–984.

Sun, S. L., Chen, H. S., Ju, W. M., Song, J., Li, J. J., Ren, Y. J., and Sun, J. (2012). Past and future changes of streamflow in Poyang Lake Basin, Southeastern China. *Hydrology and Earth System Sciences*, 16(7):2005–2020.

Tie, X. and Cao, J. (2009). Aerosol pollution in China: Present and future impact on environment. *Particuology*, 7(6):426 – 431.

Trenberth, K. (1998). Atmospheric Moisture Residence Times and Cycling: Implications for Rainfall Rates and Climate Change. *Climatic Change*, 39(4):667–694.

Trenberth, K. (1999a). Conceptual Framework for Changes of Extremes of the Hydrological Cycle with Climate Change. *Climatic Change*, 42(1):327–339.

Trenberth, K. E. (1999b). Atmospheric Moisture Recycling: Role of Advection and Local Evaporation. *J. Climate*, 12(5):1368–1381.

Trenberth, K. E. and Guillemot, C. J. (1995). Evaluation of the Global Atmospheric Moisture Budget as Seen from Analyses. *J. Climate*, 8(9):2255–2272.

Trenberth, K. E., Smith, L., Qian, T., Dai, A., and Fasullo, J. (2007). Estimates of the Global Water Budget and Its Annual Cycle Using Observational and Model Data. *J. Hydrometeor*, 8(4):758–769.

Trenberth, K. E. and Stepaniak, D. P. (2004). The flow of energy through the earth's climate system. *Quarterly Journal of the Royal Meteorological Society*, 130(603):2677–2701.

Trenberth, K. E., Stepaniak, D. P., and Caron, J. M. (2000). The Global Monsoon as Seen through the Divergent Atmospheric Circulation. *J. Climate*, 13(22):3969–3993.

Tuinenburg, O. A., Hutjes, R. W. A., and Kabat, P. (2012). The fate of evaporated water from the Ganges basin. *Journal of Geophysical Research: Atmospheres*, 117(D1):n/a–n/a.

van der Ent, R. (2014). *A new view on the hydrological cycle over continents*. PhD thesis.

van der Ent, R. J. and Savenije, H. H. G. (2011). Length and time scales of atmospheric moisture recycling. *Atmospheric Chemistry and Physics*, 11(5):1853–1863.

van der Ent, R. J. and Savenije, H. H. G. (2013). Oceanic sources of continental precipitation and the correlation with sea surface temperature. *Water Resources Research*, 49(7):3993–4004.

van der Ent, R. J., Savenije, H. H. G., Schaefli, B., and Steele-Dunne, S. C. (2010). Origin and fate of atmospheric moisture over continents. *Water Resources Research*, 46(9):n/a–n/a.

van der Ent, R. J., Tuinenburg, O. A., Knoche, H.-R., Kunstmann, H., and Savenije, H. H. G. (2013). Should we use a simple or complex model for moisture recycling and atmospheric moisture tracking? *Hydrology and Earth System Sciences*, 17(12):4869–4884.

van der Ent, R. J., Wang-Erlandsson, L., Keys, P. W., and Savenije, H. H. G. (2014). Contrasting roles of interception and transpiration in the hydrological cycle – Part 2: Moisture recycling. *Earth System Dynamics*, 5(2):471–489.

Wang, K. and Dickinson, R. E. (2012). A review of global terrestrial evapotranspiration: Observation, modeling, climatology, and climatic variability. *Reviews of Geophysics*, 50(2):n/a–n/a.

Wang, Y. and Zhou, L. (2005). Observed trends in extreme precipitation events in China during 1961-2001 and the associated changes in large-scale circulation. *Geophysical Research Letters*, 32(9):n/a–n/a.

Wang-Erlandsson, L., van der Ent, R. J., Gordon, L. J., and Savenije, H. H. G. (2014). Contrasting roles of interception and transpiration in the hydrological cycle – Part 1: Temporal characteristics over land. *Earth System Dynamics*, 5(2):441–469.

Wei, J., Dirmeyer, P. A., Bosilovich, M. G., and Wu, R. (2012a). Water vapor sources for Yangtze River Valley rainfall: Climatology, variability, and implications for rainfall forecasting. *Journal of Geophysical Research: Atmospheres*, 117(D5):n/a–n/a.

Wei, J., Dirmeyer, P. A., Wisser, D., Bosilovich, M. G., and Mocko, D. M. (2012b). Where Does the Irrigation Water Go? An Estimate of the Contribution of Irrigation to Precipitation Using MERRA. *J. Hydrometeor*, 14(1):275–289.

Weisman, M. L., Skamarock, W. C., and Klemp, J. B. (1997). The Resolution Dependence of Explicitly Modeled Convective Systems. *Mon. Wea. Rev.*, 125(4):527–548.

Wilby, R. and Wigley, T. (1997). Downscaling general circulation model output: a review of methods and limitations. *Progress in Physical Geography*, 21(4):530–548.

Winschall, A., Pfahl, S., Sodemann, H., and Wernli, H. (2012). Impact of North Atlantic evaporation hot spots on southern Alpine heavy precipitation events. *Quarterly Journal of the Royal Meteorological Society*, 138(666):1245–1258.

Winschall, A., Pfahl, S., Sodemann, H., and Wernli, H. (2014). Comparison of Eulerian and Lagrangian moisture source diagnostics – the flood event in eastern Europe in May 2010. *Atmospheric Chemistry and Physics*, 14(13):6605–6619.

Wu, P., Wood, R., Ridley, J., and Lowe, J. (2010). Temporary acceleration of the hydrological cycle in response to a CO2 rampdown. *Geophysical Research Letters*, 37(12):n/a–n/a.

Wu, S., Yin, Y., Zheng, D., and Yang, Q. (2006). Moisture conditions and climate trends in China during the period 1971-2000. *International Journal of Climatology*, 26(2):193–206.

Xie, H., Wang, P., and Huang, H. (2013). Ecological Risk Assessment of Land Use Change in the Poyang Lake Eco-economic Zone, China. *International Journal of Environmental Research and Public Health*, 10(1):328–346.

Xu, C.-y., Gong, L., Jiang, T., and Chen, D. (2006a). Decreasing reference evapotranspiration in a warming climate–A case of Changjiang (Yangtze) River catchment during 1970-2000. *Advances in Atmospheric Sciences*, 23(4):513–520.

Xu, M., Chang, C.-P., Fu, C., Qi, Y., Robock, A., Robinson, D., and Zhang, H.-m. (2006b). Steady decline of east Asian monsoon winds, 1969-2000: Evidence from direct ground measurements of wind speed. *Journal of Geophysical Research: Atmospheres*, 111(D24):n/a–n/a.

Yang, Z.-L., Niu, G.-Y., Mitchell, K. E., Chen, F., Ek, M. B., Barlage, M., Longuevergne, L., Manning, K., Niyogi, D., Tewari, M., and Xia, Y. (2011). The community Noah land surface model with multiparameterization options (Noah-MP): 2. Evaluation over global river basins. *Journal of Geophysical Research: Atmospheres*, 116(D12):n/a–n/a.

Yatagai, A., Arakawa, O., Kamiguchi, K., Kawamoto, H., Nodzu, M. I., and Hamada, A. (2009). A 44-Year Daily Gridded Precipitation Dataset for Asia Based on a Dense Network of Rain Gauges. *SOLA*, 5:137–140.

Yatagai, A., Kamiguchi, K., Arakawa, O., Hamada, A., Yasutomi, N., and Kitoh, A. (2012). APHRODITE: Constructing a Long-Term Daily Gridded Precipitation Dataset for Asia Based on a Dense Network of Rain Gauges. *Bull. Amer. Meteor. Soc.*, 93(9):1401–1415.

Ye, J.-S. (2013). Trend and variability of China's summer precipitation during 1955-2008. *International Journal of Climatology*, pages n/a–n/a.

Ye, X., Zhang, Q., Bai, L., and Hu, Q. (2011). A modeling study of catchment discharge to Poyang Lake under future climate in China. *Quaternary International*, 244(2):221 – 229.

Ye, X., Zhang, Q., Liu, J., Li, X., and yu Xu, C. (2013). Distinguishing the relative impacts of climate change and human activities on variation of streamflow in the Poyang Lake catchment, China. *Journal of Hydrology*, 494(0):83 – 95.

Yoshimura, K., Oki, T., and Ichiyanagi, K. (2004a). Evaluation of two-dimensional atmospheric water circulation fields in reanalyses by using precipitation isotopes databases. *Journal of Geophysical Research: Atmospheres*, 109(D20):n/a–n/a.

Yoshimura, K., Oki, T., Ohte, N., and Kanae, S. (2004b). Colored Moisture Analysis Estimates of Variations in 1998 Asian Monsoon Water Sources. *Journal of the Meteorological Society of Japan. Ser. II*, 82(5):1315–1329.

You, Q., Kang, S., Aguilar, E., Pepin, N., Flügel, W.-A., Yan, Y., Xu, Y., Zhang, Y., and Huang, J. (2011). Changes in daily climate extremes in China and their connection to the large scale atmospheric circulation during 1961-2003. *Climate Dynamics*, 36(11-12):2399–2417.

Zhai, J. Q., Liu, B., Hartmann, H., Su, B. D., Jiang, T., and Fraedrich, K. (2010). Dryness/wetness variations in ten large river basins of China during the first 50 years of the 21st century. *Quaternary International*, 226(1–2):101 – 111. <ce:title>Larger Asian Rivers: Climate Change, River Flow, and Watershed Management</ce:title>.

Zhang, Q., chun Ye, X., Werner, A. D., liang Li, Y., Yao, J., hu Li, X., and yu Xu, C. (2014a). An investigation of enhanced recessions in Poyang Lake: Comparison of Yangtze River and local catchment impacts. *Journal of Hydrology*, 517:425–434.

Zhang, Q., Li, L., Wang, Y.-G., Werner, A. D., Xin, P., Jiang, T., and Barry, D. A. (2012). Has the Three-Gorges Dam made the Poyang Lake wetlands wetter and drier? *Geophysical Research Letters*, 39(20):n/a–n/a.

Zhang, Q., Liu, Y., Yang, G., and Zhang, Z. (2011a). Precipitation and hydrological variations and related associations with large-scale circulation in the Poyang Lake basin, China. *Hydrological Processes*, 25(5):740–751.

Zhang, Q., Xiao, M., Li, J., Singh, V. P., and Wang, Z. (2014b). Topography-based spatial patterns of precipitation extremes in the Poyang Lake basin, China: Changing properties and causes. *Journal of Hydrology*, 512(0):229 – 239.

Zhang, Q., Xu, C.-Y., Zhang, Z., Chen, Y. D., ling Liu, C., and Lin, H. (2008). Spatial and temporal variability of precipitation maxima during 1960-2005 in the Yangtze River basin and possible association with large-scale circulation. *Journal of Hydrology*, 353(3-4):215 – 227.

Zhang, Q., Xu, C.-Y., Zhang, Z., Chen, Y. D., and Liu, C.-L. (2009). Spatial and temporal variability of precipitation over China, 1951-2005. *Theoretical and Applied Climatology*, 95(1-2):53–68.

Zhang, Y., Cheng, S.-H., Chen, Y.-S., and Wang, W.-X. (2011b). Application of MM5 in China: Model evaluation, seasonal variations, and sensitivity to horizontal grid resolutions. *Atmospheric Environment*, 45(20):3454 – 3465.

Zhou, T.-J. and Yu, R.-C. (2005). Atmospheric water vapor transport associated with typical anomalous summer rainfall patterns in China. *Journal of Geophysical Research: Atmospheres*, 110(D8):n/a–n/a.

Zhu, X., Li, Y., Li, M., Pan, Y., and Shi, P. (2013). Agricultural irrigation in China. *Journal of Soil and Water Conservation*, 68(6):147A–154A.

Zhu, Y. and Chen, L. (2002). The relationship between the asian/ australian monsoon and ENSO on a Quasi-Four-Year Scale. *Advances in Atmospheric Sciences*, 19(4):727–739.

Zou, X., Zhai, P., and Zhang, Q. (2005). Variations in droughts over China: 1951–2003. *Geophysical Research Letters*, 32(4):n/a–n/a.

Zuber, A. (1986). On the interpretation of tracer data in variable flow systems. *Journal of Hydrology*, 86(1-2):45–57.

Appendix A

Parallelization of ET-Tagging Code

In this appendix the numerical parallelization strategy to speed up the MM5-based ET-Tagging simulations is introduced. With the availability of large-memory multiprocessor machines, it is becoming more efficient to execute computational tasks in parallel instead of in series. In the mode of serial computing (Figure A.1a), all programs including the parallelizable parts are processed in a queue. As a consequence much time is consumed. High-efficiency computing can be achieved by distributing parallelizable parts to different processors, which utilizes the available computational resources more efficiently (Figure A.1b).

According to parallel computer memory architectures, there are roughly three parallel programming models utilized in numerical models (see Figure A.2). Each of them has distinct characteristics. The shared-memory model (Figure A.2a) with OpenMP in principle allows all CPUs to access the same memory and there is no need for the communication between different memories through network, compared to the message passing interface (MPI) based distributed-memory model (Figure A.2b) or the hybrid MPI/OpenMP-based model (Figure A.2c). Therefore, implementing, debugging, and performance tuning a parallel application on the basis of OpenMP compared to those on the basis of MIP/OpenMP are much easier and quicker to realize if variables are independent and no race condition can occur. Moreover, this parallel programming model also involves a compromise of effort put into parallelization, memory requirement, and availability of CPUs. Consequently, in order to achieve high performance on the CPU clusters here OpenMP is chosen for parallelization of the ET-Tagging extensions.

Since the existing source codes of the original MM5 model are parallelized by default, only the source codes of the ET-Tagging extensions need an analogous implementation. Technically, vectorization and parallelization of the original and the extended

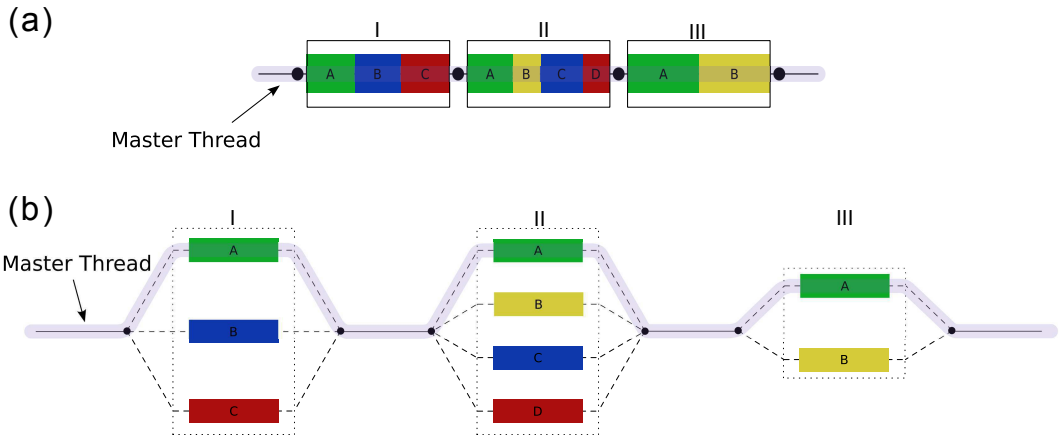

Figure A.1: Illustration of executing tasks in the mode of (a) serial computing and (b) parallel computing (http://en.wikipedia.org/wiki/Openmp).

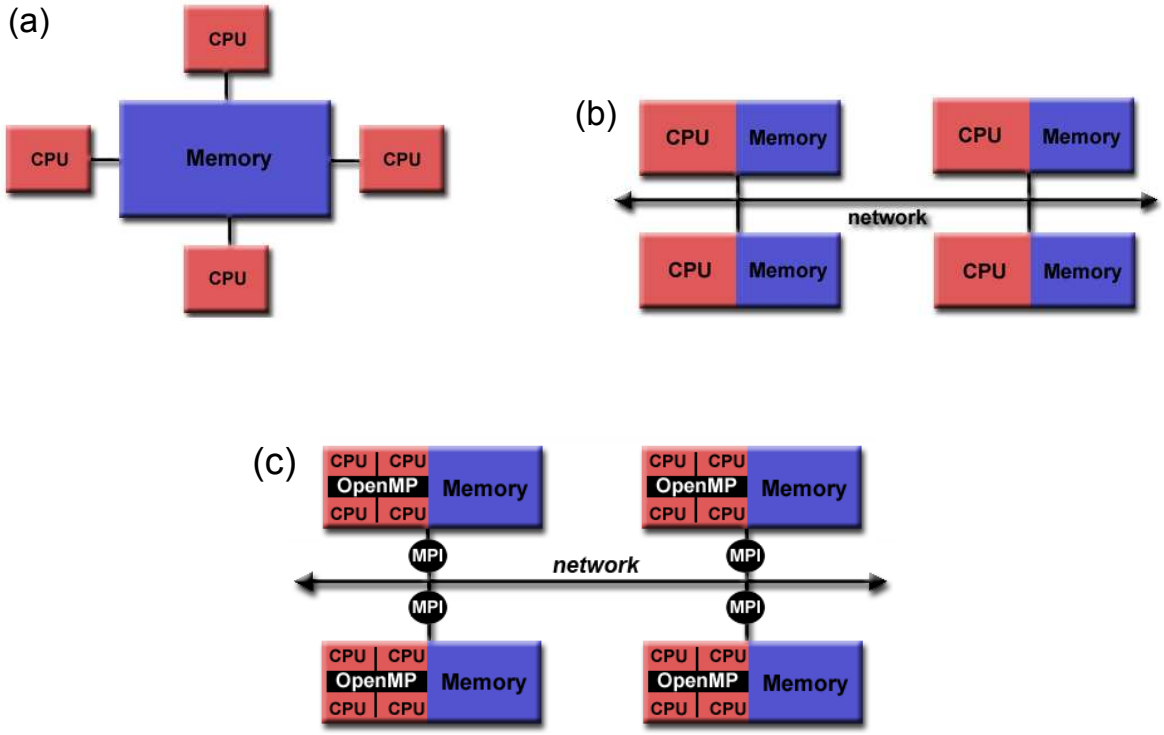

Figure A.2: Three parallel programming models utilized in numerical climate and weather prediction models. (a) Shared memory system with OpenMP, (b) Distributed memory system with MPI, and (c) Hybrid OpenMP/MPI system (https://computing.llnl.gov/tutorials/parallel_comp/).

Table A.1: Example of parallelizing a do-loop with OpenMP for a FORTRAN compiler. Blue codes are the parallel-programming directives of OpenMP.

Source code	Description
c$omp parallel do default(shared)	1. declare by default the variables in this do-loop as sharing common memory and being overwritable
c$omp private(i,j)	2. declare variables that keep their values in their own (private) memory during parallel execution
DO J=1,JL DO I=1,IL QDOT(I,J,KLP1)=0. WTENS(I,J,KLP1)=0. ENDDO ENDDO	3. main do-loop

parts should be done in the same manner to achieve compatibility.

Table A.1 illustrates an example of parallelizing a do-loop in a shared-memory mode using OpenMP. This do-loop is in charge of initializing one meteorological field for a following iteration. Parallelization is implemented by placing special directives ahead of the parallel loop (blue codes in Table A.1) for a FORTRAN compiler. Shared memory is seen by all processors in contrast to private memory.

In this thesis, parallelizing the ET-Tagging extensions consists of the following steps:

1. check the feasibility of the parallelization for all the do-loops of the extended ET-Tagging codes
2. identify the added variables that should be declared in private memory
3. place the parallel-programming directives of OpenMP ahead of each do-loop.

To examine the benefits from parallelism, the original and the extended MM5 models were applied to Southeast China with a horizontal resolution of 9 km (see Figure A.3). We conducted four experimental simulations using these two models in series and in parallel modes of computing. All the simulations were performed on the basis of the same physical schemes and the same configuration (same as the model setup of *S09* in Table 4.1) for the one month period of October in 2004. Generally, the nearly same results (not shown here) were obtained from the four experimental model runs. For a diagnostic variable, only a slightly non-systematic, numerical difference is found between serial and parallel modes of computing. It is caused by the different schemes of compilation used, and can be neglected for the following study.

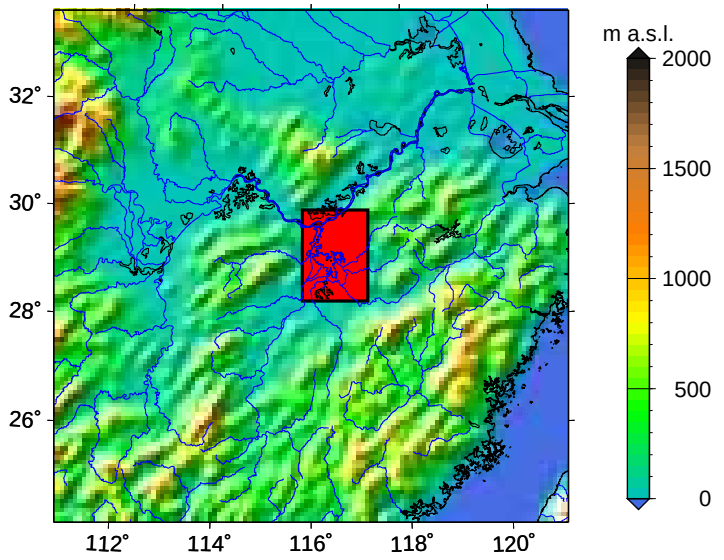

Figure A.3: Model domain with terrain height (m a.s.l) at 9 km × 9 km horizontal resolution as used for evaluation of the benefits from parallelism. Rivers, lakes, and the ocean are shown in blue. The red shaded area marks the source region where evapotranspirated water is tagged.

To measure the performance gain achieved by parallelizing a given application, speedup S is used as a performance metric. It is defined as ratio of time T_s taken to solve a problem on a single processing element to time T_p required to solve the same problem on a parallel computer with p processing elements:

$$S = T_s/T_p \tag{A.1}$$

Table A.2: Comparison of execution time and speedup in serial and parallel mode of computing, using the original and the extended MM5 models for the simulation of one month (October in 2004).

Model	Computing mode	CPU-numbers	CPU-hours	Speedup S
MM5.original	serial	1	57	14.3
	parallel	24	4	
MM5.tagging	serial	1	82.5	13.6
	parallel	24	6	

Table A.2 summarizes the values of the execution time on the 1-CPU computer and on the 24-CPUs computer and the values of speedup for one month simulation using the original and the extended MM5 models. Overall, significant performance gain is achieved in the parallel model of computing. The speedup ratio due to parallelization is 14.3 for the original MM5 model, and 13.6 for the extended MM5 model. The comparison of the CPU-hours consumed by the original and the extended MM5 model

shows that the computation of the ET-Tagging extensions takes additionally around 50 % CPU-hours. It is worthy to note that the value of a speedup ratio is also impacted by the speed of network for I/O between processors and a hard-disk storage.

Appendix B

Implementation of ET Partitioning within the Tagging Extension

The aim of this appendix is to introduce the implementation of the evapotranspiration partitioning within the framework of the ET-Tagging algorithm. The schematic for retrieving each individual ET component of the OSU-LSM model code is depicted in Figure B.1. The names of routines relating to the extensions and the corresponding descriptions are summarized in Table B.1.

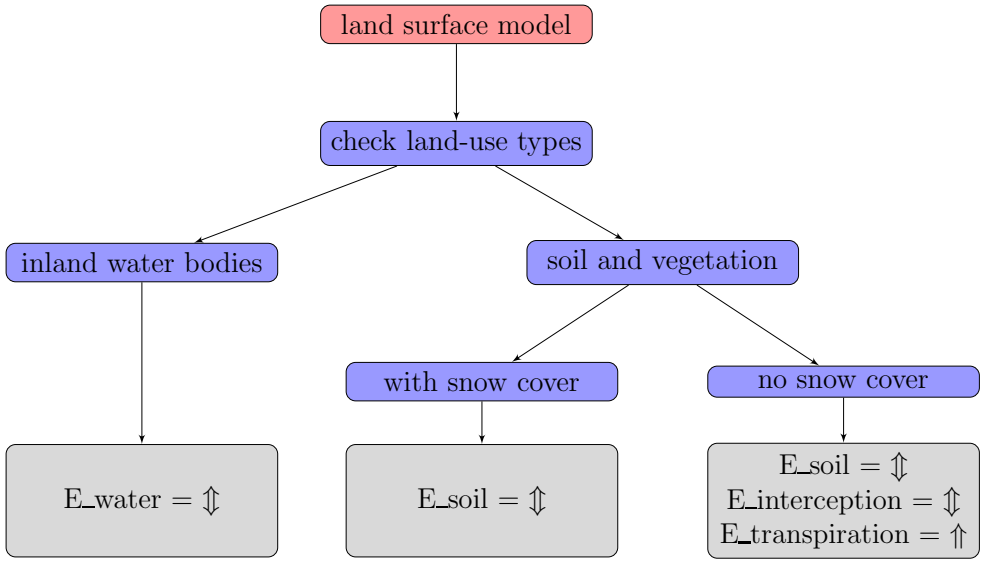

Figure B.1: Schematic of the ET partitioning in the OSU-LSM. The symbols in the gray box indicate the direction of the flux for each ET component. Upward and downward fluxes are denoted by ⇑ and ⇓, respectively. The two-direction flux (up- and downward) is symbolized by ⇳.

Table B.1: Organization of the extended MM5 code for the partitioning of the ET-flux.

routine	location	description
tagging.incl	include/	define and add new variables
diag2d.incl	include/	define the dimensions of the non-scalar new variables
init.F	domain/inital/	initialize new variables
nopac.F	physics/pbl_sfc/osusfc/	calculate the soil moisture and heat flux values and update soil moisture content and soil heat content for the case when no snow pack is present
snopac.F	physics/pbl_sfc/osusfc/	same as nopac.F, but for the case when a snow pack is present
sflx.F	physics/pbl_sfc/osusfc/	calculate and accumulate ET values
surface.F	physics/pbl_sfc/osusfc/	calculate surface conditions
mrfpbl_tag.F	physics/pbl_sfc/mrfpbl/	handle subgrid-scale vertical transports for tagged and total variables
solve.F	dynamics/nonhydro/	compute the tendencies of the prognostic variables
climoutstuff.F	domain/io	calculate new variables statistics
outtap.F	domain/io	write output data to a standard output file

New variables are defined and declared in the source code by including two files, `tagging.incl` and `diag2d.incl`. Initialization is done in the routine `init.F`. The fluxes of the four ET components (see equation 3.8) are calculated in the subroutines `nopac.F` and `snopac.F` for the cases when no snow pack or when snow pack is present (see Figure B.1). The rates of these four fluxes are transferred and accumulated in the routines `sflx.F` and `surface.F` for the calculation of processes in the planetary boundary layer (routine `mrfpbl_tag.F`). After computing the tendencies of the prognostic variables in the routine `solve.F`, statistics of the new variables are calculated in the routine `climoutstuff.F` and are written to a standard output file by using `outtap.F`.

Over inland water bodies only E_{water} can proceed. Transpiration by vegetation can only transfer water upward from the top three soil layers via roots and canopy. Snow can be stored only on the ground. The one-layer snow model accounts for snow evaporation/sublimation and melting process, mainly by considering snow heat flux, potential evaporation, and skin temperature. Here, E_{water}, E_{soil} (in case of with or

without snow cover), and $E_{interception}$ are combined as E_d (see equation 3.9) since they represent the same fast changing evaporation process at the surface. In contrast, the transpiration E_t is the slow process by which moisture is carried not only from the surface soil layer but also from the deep soil layers.